MODELLING AND EXPERIMENTATION

OF PANTOGRAPH DYNAMICS

by

GEORGE C. VESELY

B.S. University of California at Los Angeles
(1981)

SUBMITTED IN PARTIAL FULFILLMENT
OF THE REQUIREMENTS FOR THE
DEGREE OF

MASTER OF SCIENCE IN

MECHANICAL ENGINEERING

at the

Massachusetts Institute of Technology

January 1983

Signature of Author.....
Department of Mechanical Engineering
January 17, 1983

Certified By.....
David N. Wormley
Thesis Supervisor

.....
Warren P. Seering
Thesis Supervisor

Accepted By.....
Warren M. Rohsenow
Chairman, Department Committee

MODELLING AND EXPERIMENTATION

OF PANTOGRAPH DYNAMICS

by

GEORGE C. VESELY

Submitted to the Department of Mechanical Engineering on January 17, 1983, in partial fulfillment of the requirements for the degree of Master of Science in Mechanical Engineering

ABSTRACT

Rail line electrification offers important features for urban and intercity passenger service as well as high density freight service in terms of energy utilization efficiency. Improved dynamic performance of pantograph behavior can result in overhead catenary simplification, and therefore reduced cost catenary construction. A detailed analytical and experimental study of a test pantograph has been completed which has led to the formulation of an experimentally verified nonlinear, lumped parameter pantograph model that can evaluate dynamic performance. Linearization of the nonlinear model to the classical 2-mass pantograph model has provided a basis for evaluating the operating regions for which the 2-mass representation is adequate. In addition, static theoretical analysis characterizing the test pantograph force-deflection curve has been achieved.

Thesis Supervisors: David N. Wormley
Professor of Mechanical Engineering

Warren P. Seering
Assistant Professor of Mechanical Engineering

ACKNOWLEDGMENTS

The author would like to thank the U. S. Department of Transportation for sponsoring this work, and Professor D. N. Wormley for making available this study. Professor Wormley has directed the principle research with forbearance, understanding, and a large amount of professionalism. Professor Seering, as the other principle investigator, has provided crucial supervision and check on both theory and experimentation - his extra efforts are much appreciated.

The author wishes to thank Curt Spenny and John Stickler, at the Transportation Systems Center, for providing access to the experimental set up and for their kind cooperation with the procurring of experimental data. Also, thanks to Kurt Armbruster, my colleague in the project, for his assistance and helpful collaboration.

Much gratitude goes to Leslie Regan and Joan Gillis for their swift and very adept help with the final compilation of the research efforts.

Appreciation goes to the members of the Vehicles Dynamics Laboratory (Ademola, Mark, Jerry, Mary Ann, Forrest, Jim, Johny, Long Chain, Dave, Dan, Gus, Mike and John) for their comments, suggestions, and friendship. The light hearted friendship and vital help from the members of the Acoustic and Vibration Laboratory (Mark, Chuck, George, Bob and Shawn) is appreciated. Also, the members of the Machine Dynamics Laboratory, especially Randy and Ken, have been valuable with computer techniques.

Finally, good luck to Dave O'Conner in continuing the project. Hope the end result is a substantial contribution to design improvements.

TABLE OF CONTENTS

LIST OF FIGURES

LIST OF TABLES

CHAPTER 1

INTRODUCTION

1.1 Background

The use of electric power for rail transportation propulsion systems provides increased efficiency of power conversion in comparsion to non-electric drives and allows utilization of nonpetroleum based fuels. Electrical propulsion is appropriate for urban and intercity passenger service and can provide operating advances in high density freight service. In both Europe and Japan major sections of railroad lines are electrified and future plans include more extensive electrification. In the United States the Northeast Corridor Study has recommended extension of electrification. A major barrier to electrification of railroad lines is capital cost. More than half this cost is associated with the overhead wire installation. Thus improvements in the catenary-pantograph system which yield cost reduction in the catenary system may have a significant impact upon the future of electrification.

A primary factor governing the design of catenary-pantograph systems is the dynamic interaction between the catenary and the pantograph. The pantograph must follow the catenary maintaining a nominal contact force to insure electrical connection. The interaction force between the pantograph and catenary causes dynamic motions of the pantograph and catenary independently which result in variations in contact force. As train speed increases, these dynamic interaction problems become more severe, and to maintain sufficient contact force increased levels of nominal contact force are required which then result in increased wear. In terms of conventional catenary design either a more complex catenary design

such as a compound catenary is necessary or supporting poles are required to be spaced more closely to provide a constant effective catenary stiffness which minimizes the pantograph-catenary disturbances. With reduced dynamic interactions, the nominal design level of contact force may be reduced to decrease wear and yet maintain good electrical continuity.

While technically it is feasible to construct a nearly constant stiffness catenary, it is not economically feasible for the primary application areas in the United States. A simple low cost catenary system is desired which can meet dynamic performance requirements. In this study system performance improvements are sought through improved pantograph dynamic performance which allow use of simple catenary configurations with wider pole spacing and/or allow use of lower cost catenary materials such as aluminum. The development of an improved pantograph has the capability to allow increased operating speed and/or to allow the use of simple configurations and materials leading to reduced capital cost.

While the work presented here is focused on theoretical and experimental analysis of pantograph dynamics, the catenary dynamics of the pantograph-catenary system are treated in parallel under the same grant by my colleague, Kurt Armbruster in ref. [1,2]. Investigation into the benefits of these various pantograph-catenary systems is desired. Therefore the performance, in terms of loss-of-contact and contact force behavior, is analyzed for representative pantographs in ref. [2].

1.2 Research Objectives and Study Scope

The primary function of the electric railcar pantograph* is to maintain contact with the catenary contact wire at all train speeds in the presence of changing catenary wire heights and catenary irregularities. Many variously configured pantographs are presently in operation to accomplish this task. All of these pantographs work on the same principle (jointed arm linkage motion) and perform the same function (maintaining contact). A basis for evaluating these physically different pantograph designs and suggestions for new designs is provided by this study. To accomplish these research objectives effort has been undertaken to:

(1) Develop a dynamic nonlinear simulation model fully describing nonlinear effects on performance.

(2) Formulate a linearized version of the nonlinear model capable of giving dynamic information for a nominal operating range.

(3) Derive static relations yielding information on the steady uplift force characteristics.

(4) Experimentally characterize and test a specimen pantograph statically and dynamically.

(5) Verify and evaluate analytical models with experimentally obtained data.

This document summarizes the results achieved in these tasks. In Chapter 2 a nonlinear performance model for a generic pantograph configuration is developed. From this nonlinear model a linear performance model is formulated for use in parametric evaluations. In addition, static relations are derived characterizing the uplift force.

---

*The electric railcar pantograph is the physical mechanism on the top of electric railcars that tracks an overhead catenary contact wire while the train is moving, and which provides electrical connection.

Experimental performance data for a specimen pantograph has been obtained as described in Chapter 3. The data have been used to identify regions of performance over which the model is valid. Finally, the conclusions reached in the study are summarized in Chapter 4.

1.3 Literature Review

It is commonly known that two major components make up the typical pantograph design; that is the frame structure, and the head which is connected to the frame through a suspension unit. For this reason the linear 2-mass model has been adopted universally and first implemented by Morris [3] in 1964. Though the utility of the 2-mass model has been demonstrated by numerous researchers [3,4,5,6,7,8,9,10,11,12] it nonetheless represents a simplified description of the actual pantograph. The pantograph may be nonlinear in many respects; as in nonlinear frame geometry, stops in head suspension, and adverse friction.

Levy, et al. [7] 1968, recognized that many pantographs operate with stops in the head suspension, and subsequently included stop regions within their simulation models. While their effort is a step closer to representing these effects, break-away phenomenon (i.e. stops such that a specific amount of force is required to separate the two impinging elements) is accounted for by this author. Vinayagalingam [6] found that the 2-mass model compared well with experimental data for frequencies under 5 Hz. At higher frequencies the flexibility of the head assembly became significant, and a more realistic 3-mass model was then introduced.

Most recent work, for example [4,16], on both passive and active

pantograph design has been directed toward reduction of the pantograph dynamic head mass. Gostling and Hobbs [4] further state that head suspension be kept soft. Coxen, et al. [16] have reported on development of a simple high performance pantograph by British Rail and Brecknell Willis. The design includes a torsion spring suspension for a light set of collectors, air foils to overcome aerodynamic asymmetries, and a pneumatic cylinder as part of the frame suspension. This cylinder provides constant force at low velocities, and through selection of the orifice size, it serves as a spring and damper during periods of high frame velocity.

Wann [10] represented the pantograph as a two-mass mathematical model. Passive and several configurations of active pantograph models were studied, the results of subsequent simulations were evaluated. Active pantograph control is shown to offer potential for substantially improved system performance.

Active elements have been introduced into several recent pantograph designs. Hydraulic actuators were incorporated by Sikorsky Aircraft, [12] 1970, into the frame of a Stemman pantograph. Two configurations were tested. For the first, a ram at the base drove the frame in response to a signal indicating motion in the head suspension. As the head moved up, the frame was driven up beneath it. In the second, a 'Dual' configuration, a second ram was included between the frame and pantograph head. For neither configuration was a stable control system achieved.

Behjaev, et al. [17] 1977, has discussed a TS-IM type pantograph with an active pneumatic cylinder designed to stabilize contact pressure

on the catenary. The system also provides a means for raising the pantograph from its lowered position. Vinayagalinyam [5] has designed a hydraulic servovalve to detect head accelerations and components so as to reduce contact force variation. Simulations suggest that the servovalve reduced pantograph-catenary contact force variations to acceptable levels under single span catenaries at speeds of up to 250 km/h.

Most pantograph models have been developed in conjunction with catenary models, and have increased markedly in complexity over the past two decades. Elkins [8] proposed modal analysis of the catenary-pantograph system whose results could easily be compared with experimental data. Hobbs [9] produced a pantograph catenary numerical model and conducted experiments to verify it. In order to evaluate the Brecknell-Willis British Rail pantograph, he conducted frequency response tests by exciting the head hydraulically with up to 300 N (675 lb) at up to 40 Hz. Initial results did not conform to those expected from a linear system. An improved BW-BR pantograph was designed to minimize friction. Response of this system conformed much more closely to those expected of a linear system.

The Faiveley pantograph has been evaluated by a number of authors. Grey [14] measured aerodynamic lifting forces, spring constants for the head support and damping between frame and base. Peters [13] evaluated performance of both single and dual stage Faiveley pantographs in operation under a catenary. These tests were run with a steady contact force of 90 N (20 lb) and a pantograph head mass of 15 kg (33 lbm). Significant improvement in performance was achieved by increasing contact force to 125 N (28 lb) and reducing head mass from 15 kg to 13 kg.

Peters reported that 45% of the time in separation was spent during non-destructive separations of 2-5 ms. He showed that unacceptable contact behavior occurred when the standard deviation of the contact force equaled 1/3 of the mean force.

Gostling, et al. [4], tested an experimentally modified BR-BW pantograph aforementioned in ref. [9]. From the laboratory tests it was shown to have low friction ($\pm$ 4 N), and small dynamic frame and head mass (12 kg and 7 kg respectively) for which other pantograph designs are typically twice these values. Experiments on test track runs demonstrated that performance was very good up to 175 km/h, so that a production version was worthy of serious consideration.

CHAPTER 2

PANTOGRAPH MODEL DEVELOPMENT

2.1 Model Formulation

An analytical model has been developed to determine pantograph performance characteristics. Two common pantograph configurations have been identified including a symmetric frame similar to the August Stemman pantograph, and an asymmetric frame similar to the Faively or Brecknell Willis pantographs. In the present study a nonlinear generic pantograph model has been developed which represents a wide variety of basic pantograph configurations, and includes the effects of catenary contact wire disturbances and irregularities. This model can be coupled with the model of the catenary described in ref.[2] to form a complete system model.

The physically symmetric frame pantograph shown in Figure 2.1 exhibits a scissors action about a center line on which the top center joint (control bar) moves vertically. In the model which is representative of pantographs such as the August Stemman pantograph, a light weight linkage between the two base pivots preserves symmetric motion of the two upper links and of the two lower links about either side of the vertical symmetry line. The uplift force originates from the tensioned base spring, located near the two base hinges, causing the two lower links to rotate upward simultaneously.

A physically asymmetric frame pantograph depicted in Figure 2.2 exhibits a jointed arm motion where the control bar is constrained to move vertically. Both the symmetric and asymmetric frames can be considered to be equivalent in motion characteristics by arranging the symmetric type's linkage on one side of the symmetry line with minor

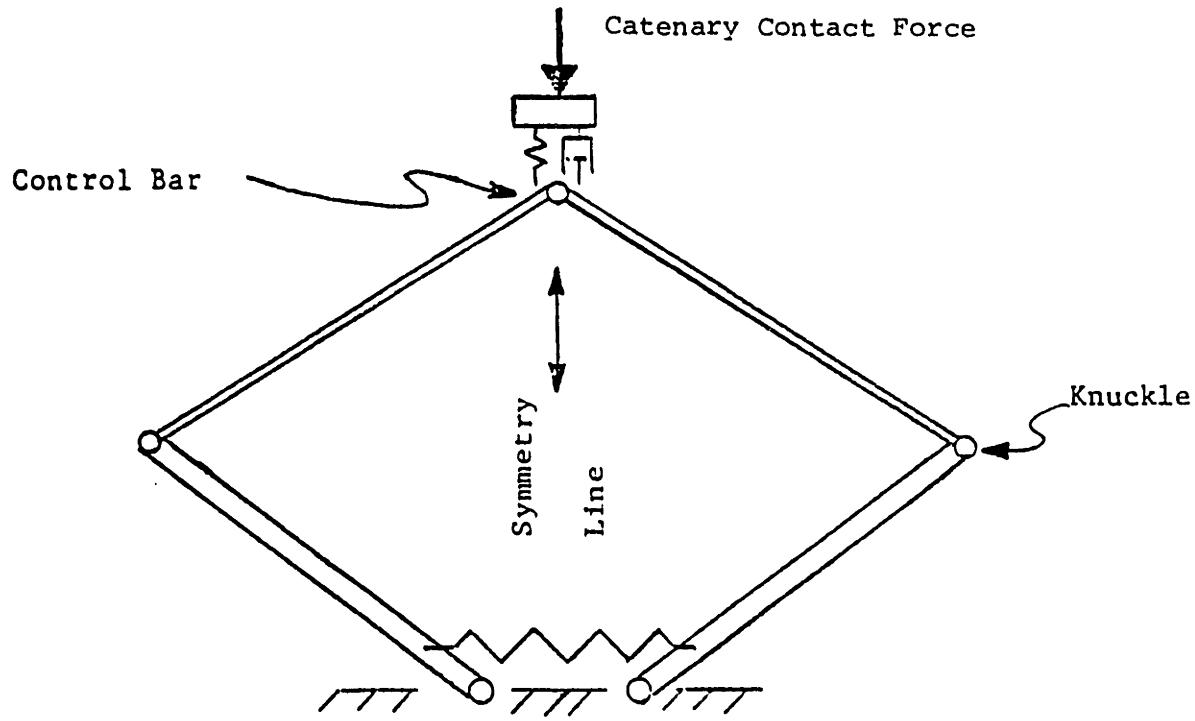

FIGURE 2.1: SYMMETRIC PANTOGRAPH CONFIGURATION

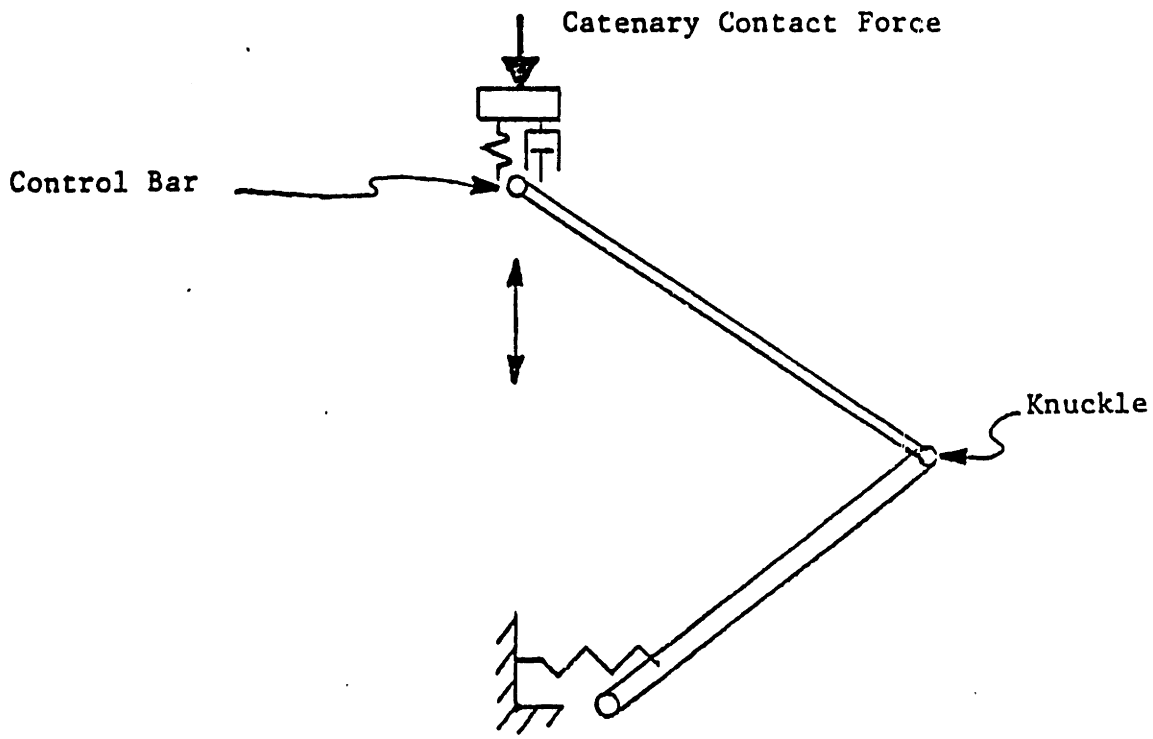

FIGURE 2.2: ASYMMETRIC PANTOGRAPH CONFIGURATION

modifications. For the typical pantograph there is one base pivot at which the frame lower link is attached to the railcar roof. The uplift force is then provided by a base spring with one end attached to the pivoted lower link and the other attached to a railcar roof fixture.

Both the physically symmetric and physically asymmetric frames support a head suspension and head mass at the control bar. The head mass has motion relative to the control bar through the head suspension which accomodates the absorption of high frequency catenary disturbances.

Considering the physical form of typical pantographs, a dynamic performance model may be formulated in which the frame linkage masses are lumped and the frame stiffness and damping aggregated into equivalent stiffness and damping elements, while representing the head suspension and mass with their existing mass, stiffness and damping values. Figure 2.3 represents the pantograph configurations in terms of equivalent frame mass and general suspension G with specific head suspension elements and catenary contact force. From Figure 2.3 a general two degree-of-freedom linear model for the pantograph has been formulated, and its performance characteristics can be evaluated for the suspension configurations shown in Figure 2.4 which represent the dominant types of classical linear suspensions.

The pantograph physical configuration is inherently geometrically nonlinear, thus prior to developing a linear model, a fully nonlinear model must be developed and then the linear model derived from it. In the derivation, since the lower link rotates about a fixed pivot, and the upper link rotates and translates in direct relation to the lower link angular orientation, the selection of the angular position of the

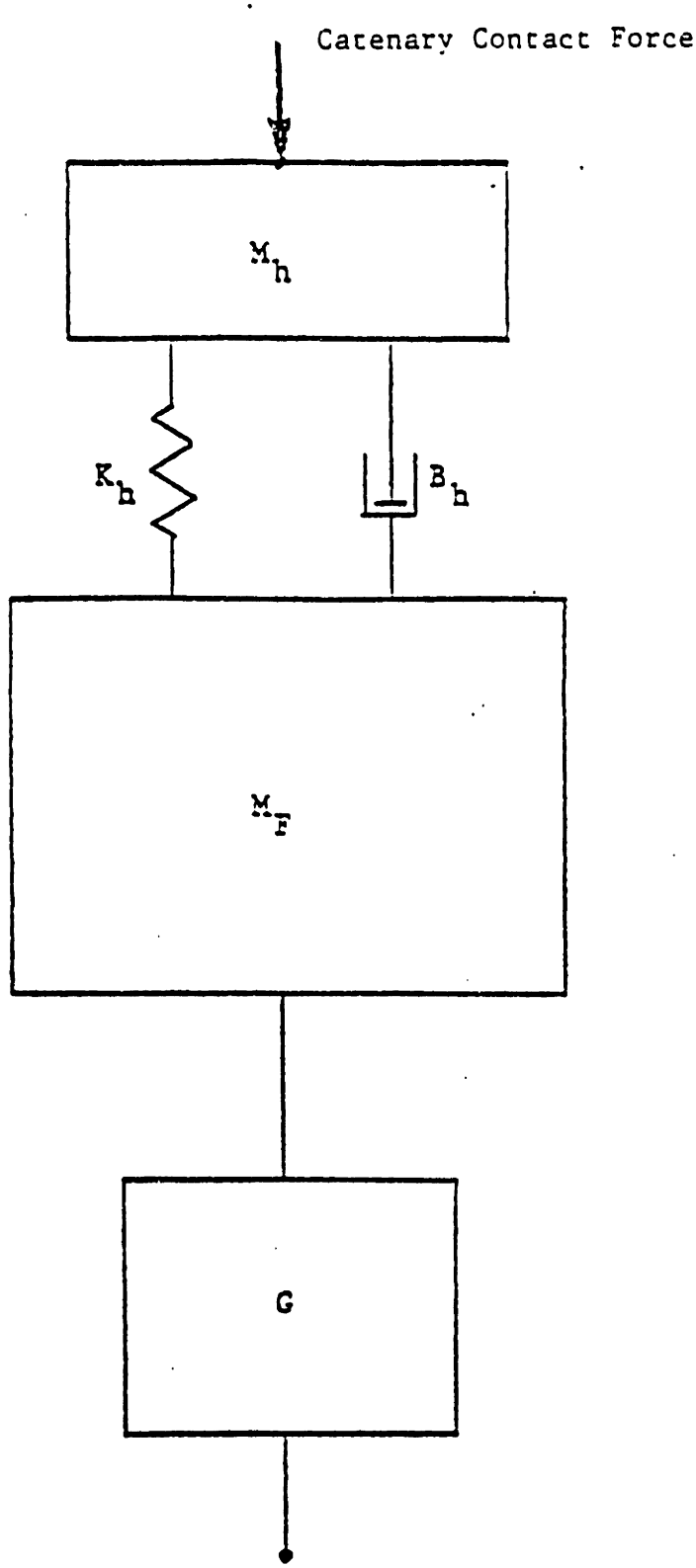

FIGURE 2.3: GENERAL LINEAR PANTOGRAPH MODEL

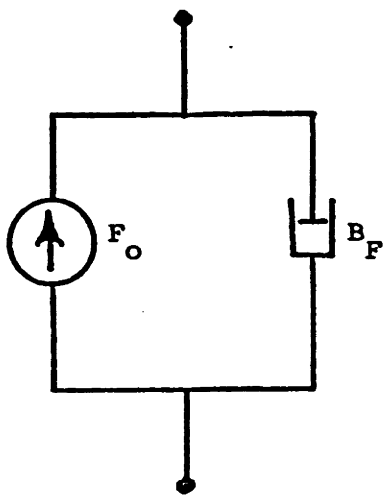

Constant Force Suspension

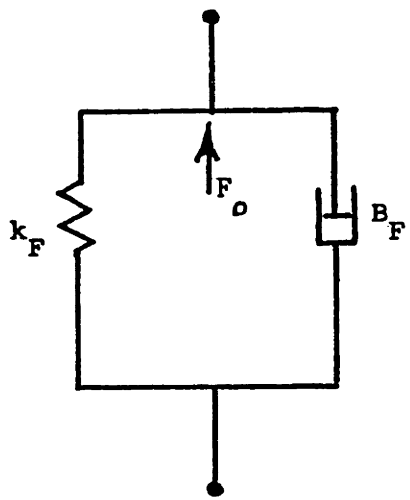

Mechanical Stiffness and Damping

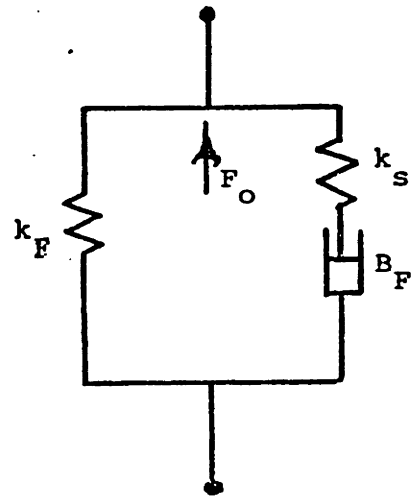

Mechanical Stiffness and Compliance Mounted Damper

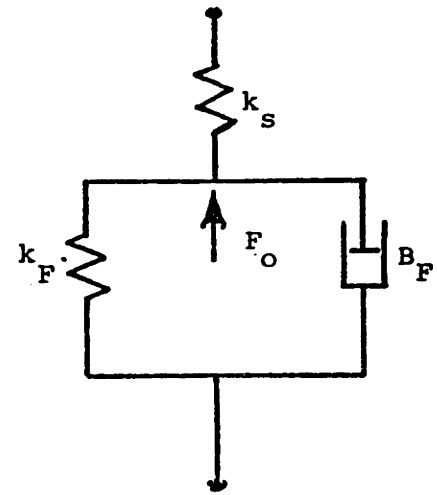

Equivalent Mechanical Suspension for Pneumatic Orifice Damped Suspension

FIGURE 2.4: SUSPENSION FORMS

lower link as the describing generalized coordinate is natural. The other generalized coordinate necessary to describe the dynamics is the head mass absolute vertical height. This coordinate conveniently measures the distance from the railcar roof to the contacting surface of the pantograph head, along with yielding dynamic information on the head mass. In summary, the degrees-of-freedom are the angular position of the lower link associated with the frame configuration and the absolute position of the pantograph head.

A nonlinear model based upon the two degrees-of-freedom has been developed to investigate performance indices and evaluate the limitations of linear models. The following section details the physical description of the analytical nonlinear model. It not only incorporates the geometric nonlinearities, but in addition includes suspension element nonlinearities.

Three principle pantograph models have been developed and are summarized as:

(1) A nonlinear dynamic model in which rigid link motions and absolute head motion are excited through vertical catenary interaction.

(2) A static model, derived from the nonlinear model, in which height is determined from equilibrium load.

(3) A linear model, derived from the nonlinear model, from which effective parametric relations are generated.

These models allow computation of performance behavior such as loss-of-contact and dynamic tracking force variation. In addition, evaluations comparing experimental results and parametric studies are performed.

2.2 Nonlinear Model

A nonlinear analytical model describing electric railcar pantograph dynamics is used for computation of tracking force and loss-of-contact. The operational model is capable, through appropriate substitution of system parameters, of representing a wide spectrum of existing pantographs. The degrees of freedom for the pantograph shown in Figure 2.5 are:

θ_1, the frame lower link angular position; and

y_h, the absolute position of the head.

The operational model directly incorporates the nonlinear geometry of the linkage. By addition of a constraint equation, the control bar along with the pantograph head is restricted to move along a straight vertical line. With the assumption of rigid jointed links, angular positions of the links about the joints are geometrically related to the frame vertical height. Thus, only one degree of freedom θ_1 is required to represent the frame motion when the flexibility of the frame elements is neglected. The head structure is constrained to move vertically with respect to the top of the upper link (i.e. the control bar). The necessary constraint for this case is included in Appendix A. A secondary coordinate describing relative head movement from the control bar of the frame is useful for determining head suspension separation and force.

The analytical model includes a lumped mass and moment of inertia (m_1 and I_1) for the rigid lower link, a lumped mass and moment of inertia (m_2 and I_2) for the rigid upper link, a concentrated mass m_k at the knuckle representing the extra mass required for the joint, a concentrated mass m_c at the top of the upper link to represent the control bar, and

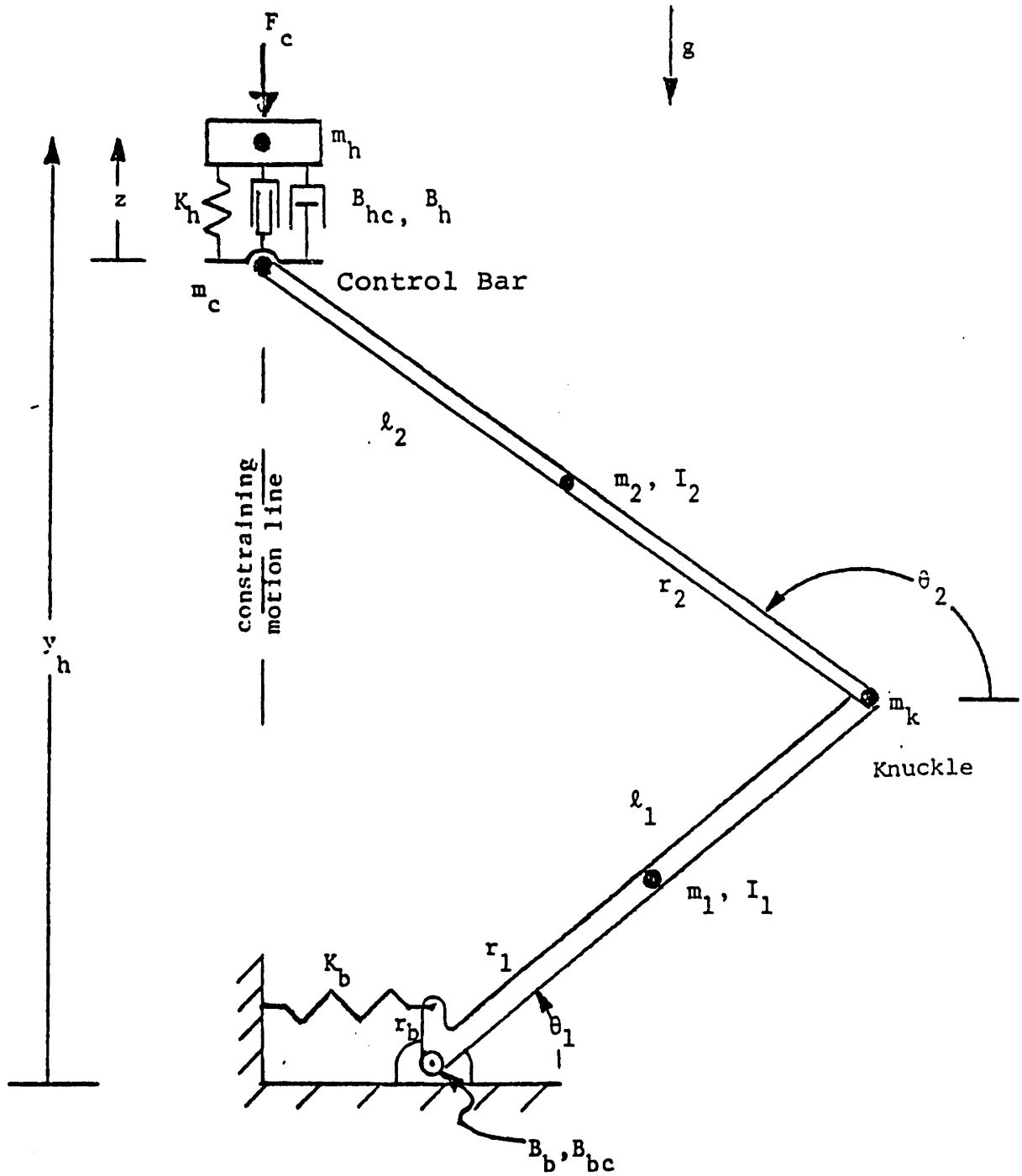

FIGURE 2.5: NONLINEAR MODEL

and a lumped mass m_h to represent the head. The head mass is separated from the control bar of the frame with a head spring, K_h, a head damper, B_h, and coulomb friction in the head suspension B_{hc} arising from suspension parts binding and rubbing. The frame suspension consists of a pretensioned base spring K_b acting on a small moment arm r_b which is a rigid part of the lower link, a torsion damping B_b located at the base pivot to account for frame hysteresis and friction, and coulomb friction B_{bc} located at the base pivot arising from frame linkage binding. Finally, a spring K_f is included during simulation between the head mass and applied actuator force to represent deformation in the head structure, (head deflection has been observed during pantograph tests). The applied contact force F_c represents the pantograph head contact with the catenary while gravity forces act on each of the five lumped masses.

The equations of motion for the model have been coded into FORTRAN and implemented in a nonlinear, time domain digital computer simulation program. The derivation of the governing equations of motion is given in Appendix A and can be summarized in two nonlinear differential equations as:

$$I\ddot{\theta}_1 + C\dot{\theta}_1^2 = Q \tag{2.1}$$

$$m_h\ddot{y}_h + B_h\left[\dot{y}_h - \left(\ell_1\cos\theta_1 - \ell_1\frac{\sin\theta_1\cos\theta_2}{\sin\theta_2}\right)\dot{\theta}_1\right] + K_h\left[y_h - (\ell_1\sin\theta_1 + \ell_2\sin\theta_2)\right]$$

$$= -F_c - m_h g - B_{hc}\,\mathrm{sgn}\left[\dot{y}_h - \left(\ell_1\cos\theta_1 - \ell_1\frac{\sin\theta_1\cos\theta_2}{\sin\theta_2}\right)\dot{\theta}_1\right] \tag{2.2}$$

where I is the generalized inertia, C is the centripetal coefficient, and Q is the generalized force. I, C, and Q consist of many terms that are fully described in Appendix A. Equation (2.1) is derived from a force balance on the frame and equation (2.2) is derived from a force balance on the head mass.

A comparison of results from these nonlinear equations with experimental results is given in Section 3.5.

2.3 Static Model

The pantograph force-deflection characteristic may be derived using a pantograph static analysis. By eliminating all terms involving dynamic variables from the governing dynamic equations, the static equilibrium equations may be derived from the nonlinear dynamic model differential equations (2.1) and (2.2).

The static analysis parameters are determined from the reduced nonlinear equations as outlined in Appendix B. The static analysis includes the gravity forces on all five lumped masses, the horizontal force F_b in the base spring, and the applied force for equilibrium F_c. With the appropriate algebraic manipulation of the deduced static relations, the equation to calculate the required load F_c placed on top of the pantograph to offset its uplift force is:

$$F_c = \frac{F_b r_b \sin(\theta_1+\theta_o) - (m_1 r_1 + m_k \ell_1) g \cos\theta_1 - m_2 g (\ell_1 \cos\theta_1 - r_2 \cos\theta_2 \frac{\ell_1 \sin\theta_1}{\ell_2 \sin\theta_2})}{(\ell_1 \cos\theta_1 - \ell_1 \frac{\sin\theta_1 \cos\theta_2}{\sin\theta_2})}$$

$$- m_c g - m_h g \qquad (2.3)$$

where the base spring force is:

$$F_b = \text{PRETEN} + K_b r_b \cos(\theta_1 + \theta_o) \qquad (2.4)$$

Static performance for the prototype pantograph has been outlined and compared with theory in Section 3.3.

2.4 Linear Model

Many of the models utilized to study pantograph behavior described in the literature are linear models. Linear models are especially useful in parametric design studies, however, their validity must be checked with the fully nonlinear model. The nonlinear analytical model has been linearized to form the general linear model illustrated in Figure 2.6. The linearization was accomplished about two absolute coordinates, y_h position of head mass, and y_c vertical height of the frame control bar. The form of this linearization is equivalent to the generic model shown in Figure 2.3 with the second frame suspension, mechanical stiffness and damping, implemented from Figure 2.4.

The two-mass system includes a frame mass M_F, a head mass M_H, a head suspension consisting of head damping B_H, connected between the frame and head structure, in parallel with the head stiffness K_H. In addition, a frame suspension consisting of damping B_F, is connected between the vehicle roof and pantograph frame, and is in parallel with the frame spring rate K_F and steady uplift force F_o. The contact force F_c is the applied time varying contact force due to catenary interaction.

The final linearized equations from Appendix C are:

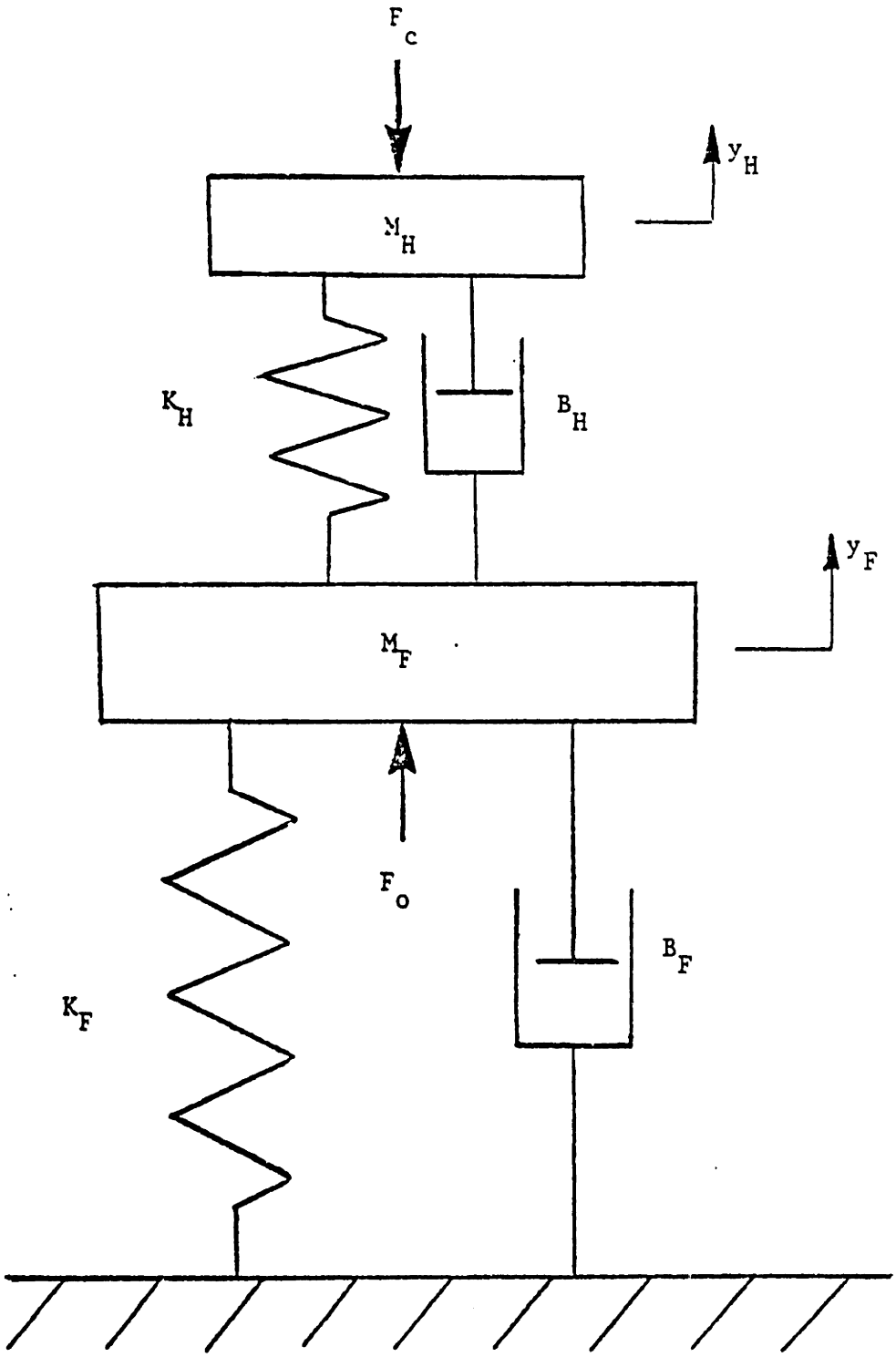

FIGURE 2.6: LINEAR PANTOGRAPH MODEL

$$M_F\ddot{y}_F = -(K_F + K_H)y_F - (B_F + B_H)\dot{y}_F + K_H y_H + B_H \dot{y}_H \tag{2.5}$$

$$M_H\ddot{y}_H = K_H y_F + B_H \dot{y}_F - K_H y_H - B_H \dot{y}_H - F_c \tag{2.6}$$

The first equation represents the force balance for the effective frame mass, while the second equation represents the force balance for the head mass. Determination of parameter values for the linearized model is described in the following section.

2.5 Parameter Values for Test Pantograph

Closed form expressions have been derived (see Appendix C) to relate the physical link masses and inertias, joint damping, and base spring stiffness of the asymmetric nonlinear model to the effective frame mass, damping, and stiffness of the linear model. These effective parameter values are a function of the pantograph operating height because of the nonlinear geometry, and are plotted in Figures 2.7, 2.8 and 2.9 for the August-Stemman pantograph type. The effective linear frame mass and damping coefficient increase with height, as the effective frame stiffness is essentially zero over a wide range of heights. A tabular summary of the effective linear pantograph frame parameters for three operating heights are summarized in Table 2.1, along with parametric data cited in the literature by authors associated with British Rail and General Electric. The test pantograph has both a higher effective linear frame mass and head mass than the other pantographs. The head stiffness is approximately equal for all units with the test pantograph slightly larger, while the effective frame stiffness at the design point is essentially zero for all units. The models cited in the literature assume the constant force design

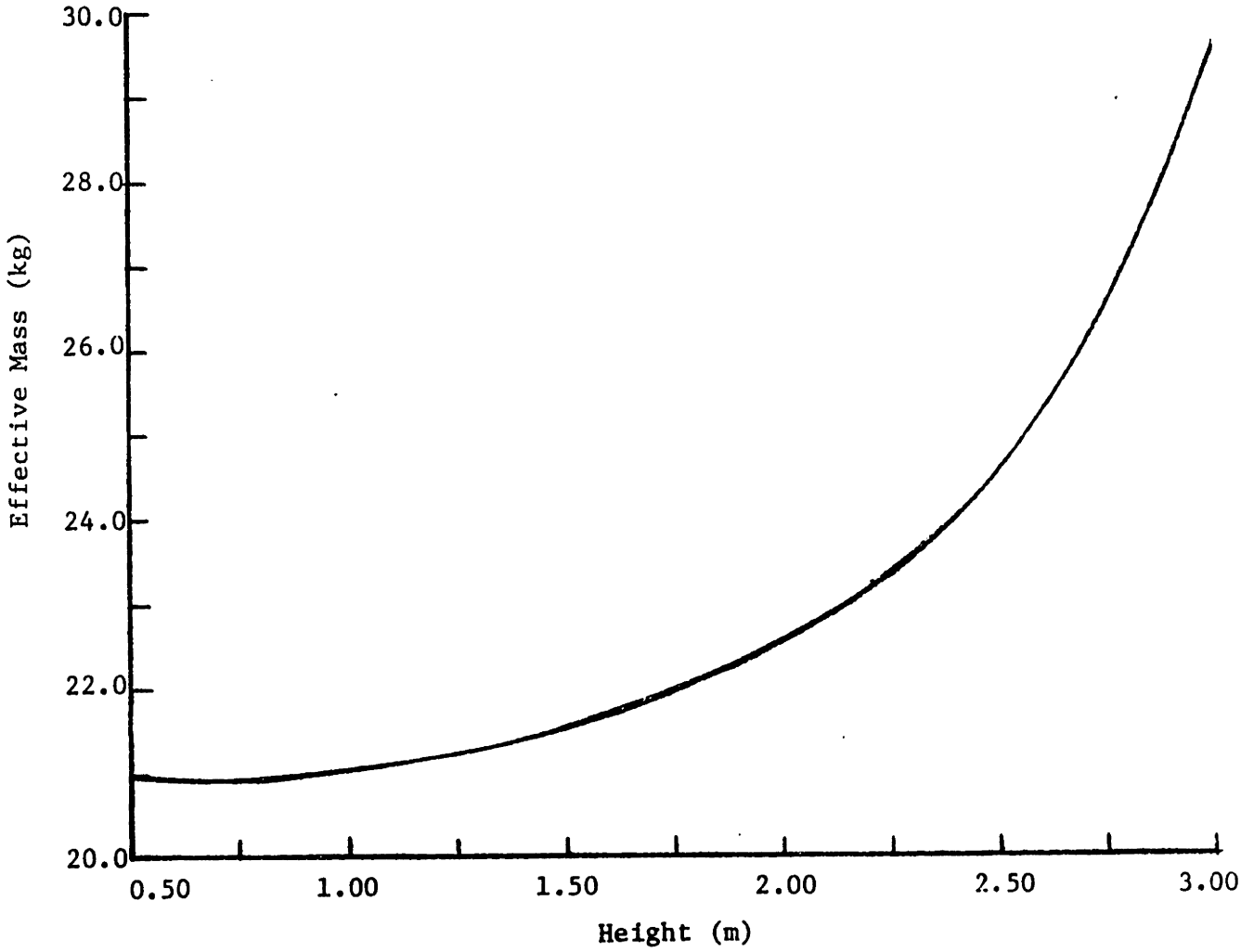

FIGURE 2.7: EFFECTIVE FRAME MASS FROM LINEARIZATION

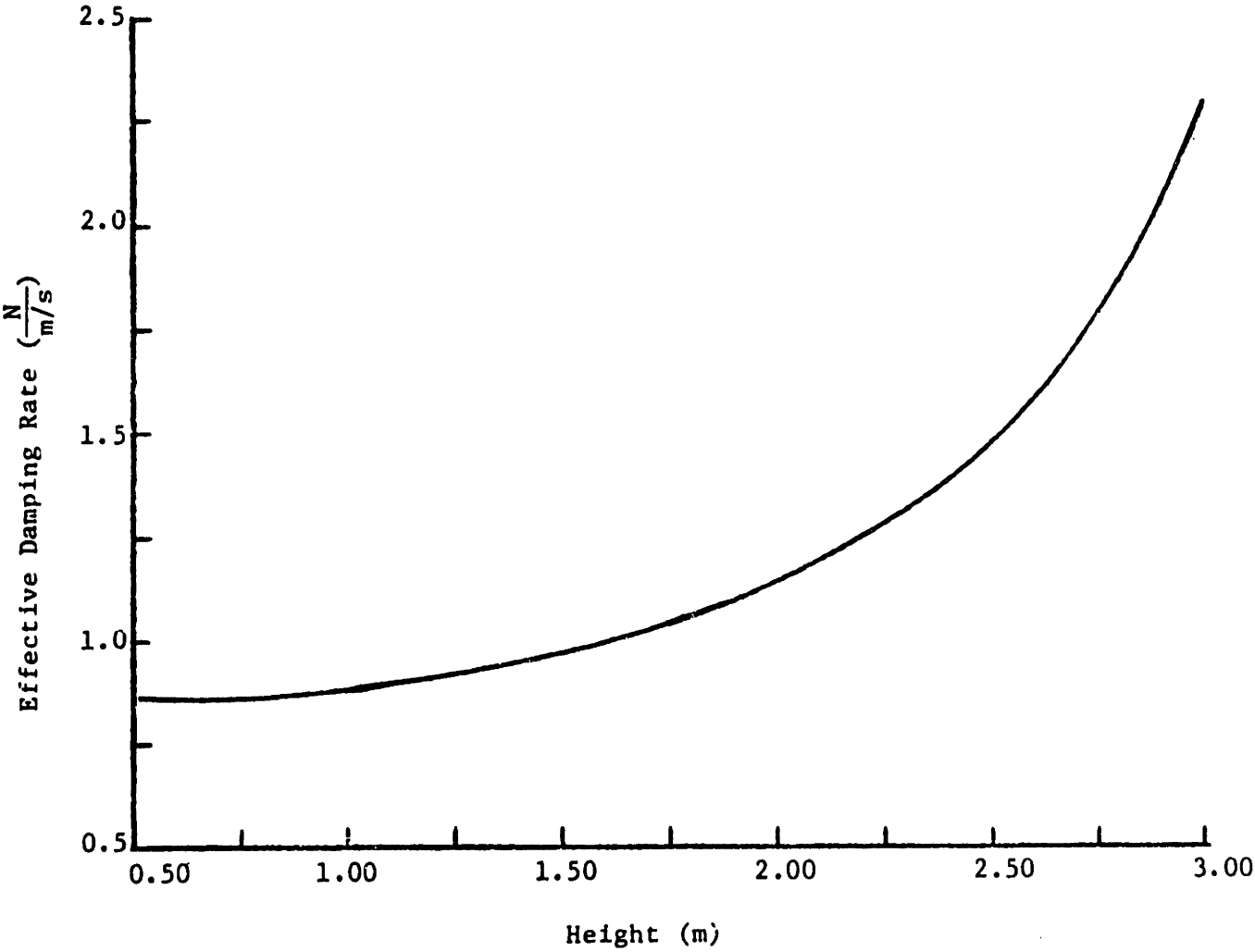

FIGURE 2.8: EFFECTIVE FRAME DAMPING RATE FROM LINEARIZATION

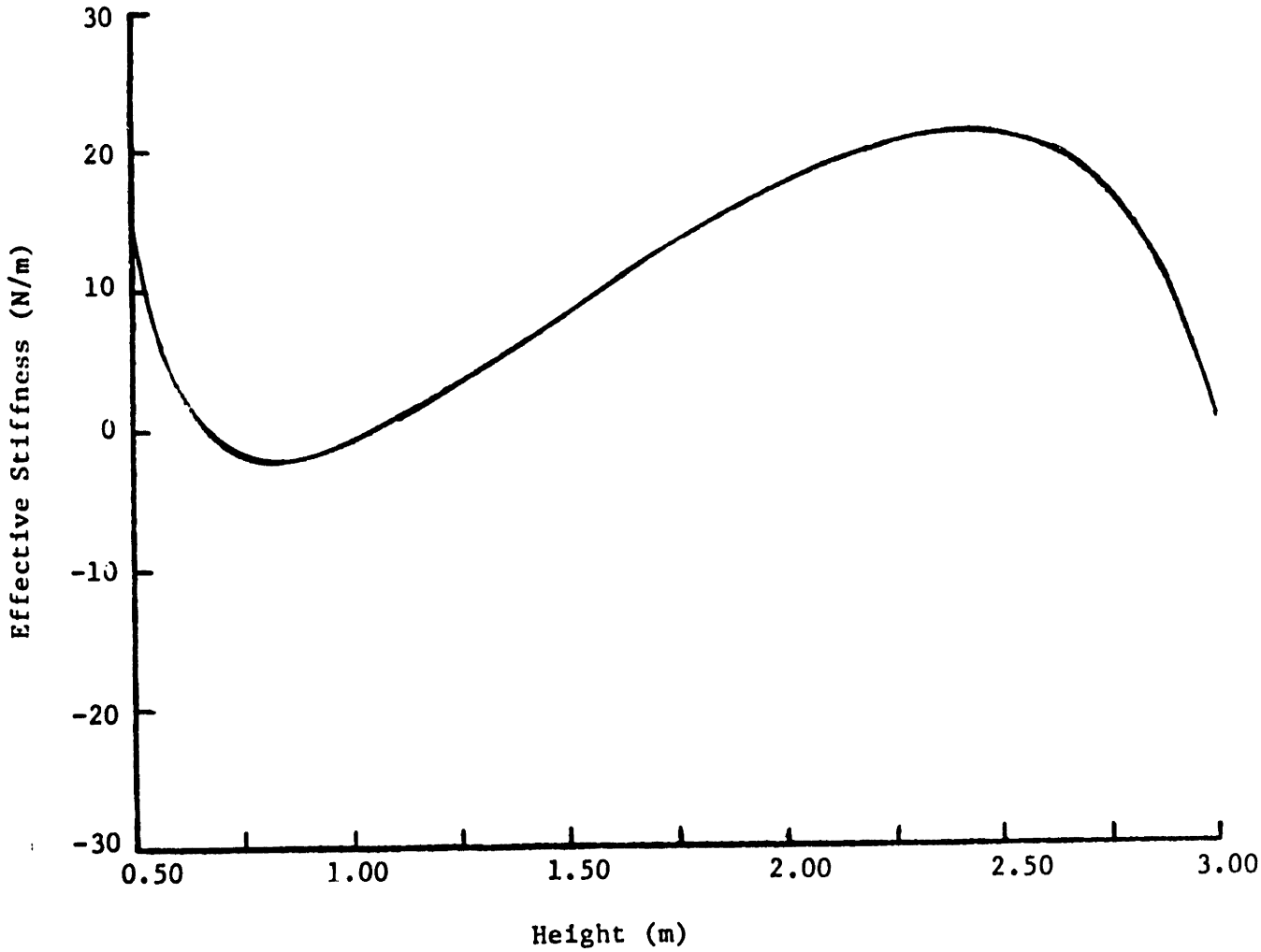

FIGURE 2.9: EFFECTIVE FRAME STIFFNESS FROM LINEARIZATION

TABLE 2.1

PANTOGRAPH PARAMETER VALUES

PARAMETER	Ref. [8]	Ref. [5]	Ref. [7]	EFFECTIVE VALUES FROM NONLINEAR MODEL OF AUGUST-STEMMAN		
				Height of 1.0 m	Height of 2.0 m	Height of 3.0 m
Frame Mass M_F (kg)	17.25	17.25	18.4	21.0	22.5	29.7
Frame Stiffness K_F (N/m)	0.0	0.0	0.0	-1.0	17.0	0.0
Frame Damping B_F (N/m/s)	36.0	30.0	70.0	0.9*	1.1*	2.3*
Head Mass M_H (kg)	9.1	9.0	12.7	13.1	13.1	13.1
Head Stiffness K_H (N/m)	7000	7000	7000	9580.0	9580.0	9580.0
Head Damping B_H (N/m/s)	130	70	140	300.0*	300.0*	300.0*

*Estimated from design data

goal (the first frame suspension in Figure 2.4) can be met at the operating point. The linear model has been implemented into a time-domain computer program and a steady state frequency-domain computer program in ref. [2].

2.6 Effects of Pantograph Nonlinearities

Comparison of the linear pantograph model with the developed nonlinear pantograph model is discussed in this section. The principle analysis in references [5], [7], [8], and others typically consisted of the dynamic behavior of a two-mass pantograph model similar to that shown in Figure 2.6. This model physically consists of a head mass, frame mass, head suspension spring and damper between the two masses, a damper and steady uplift force between the frame mass and vehicle roof, and finally a disturbing catenary force acting on the head. Some authors implemented variations in this baseline model to analyze particular features; for example, the flexure of the head structure was modeled with more than one mass in reference [6]. In the present study the linear model of the literature has been changed with the addition of a frame spring between the frame mass and vehicle roof to represent finite stiffness in the frame suspension.

The parameter values used in the linear model are derived directly from the lienarization of the nonlinear model, their characteristics are shown in Figures 2.7, 2.8, and 2.9. The nonlinear model used in this comparison is that described in Section 2.2 and configured to the prototype described in Section 3.1. The comparison takes place at an operating height of 2.0 meters. At this height the linear model's effective frame mass is 22.77 kg, while the effective frame damping and

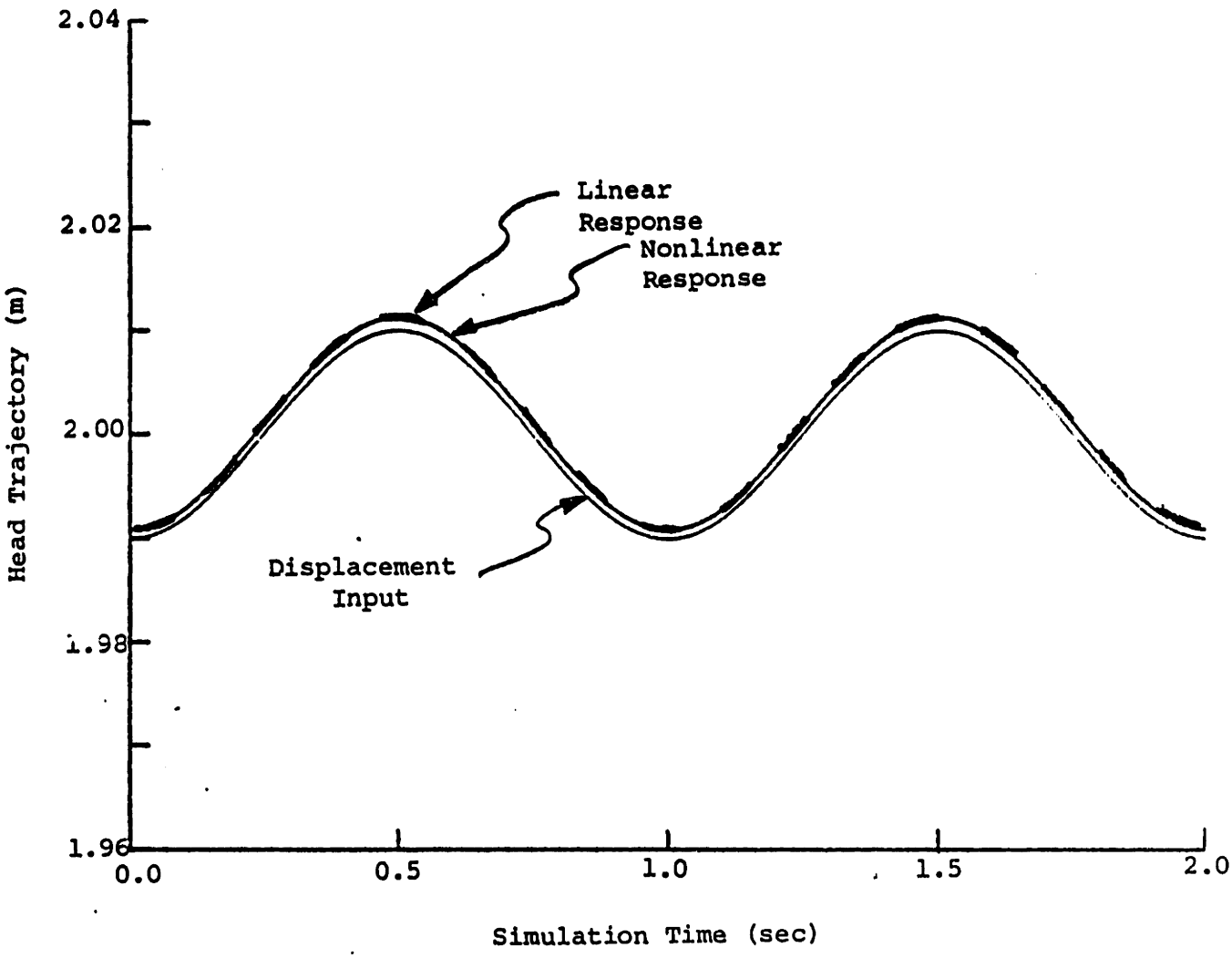

FIGURE 2.10: MODEL COMPARISON AT 1 Hz FOR $\pm$ 1cm

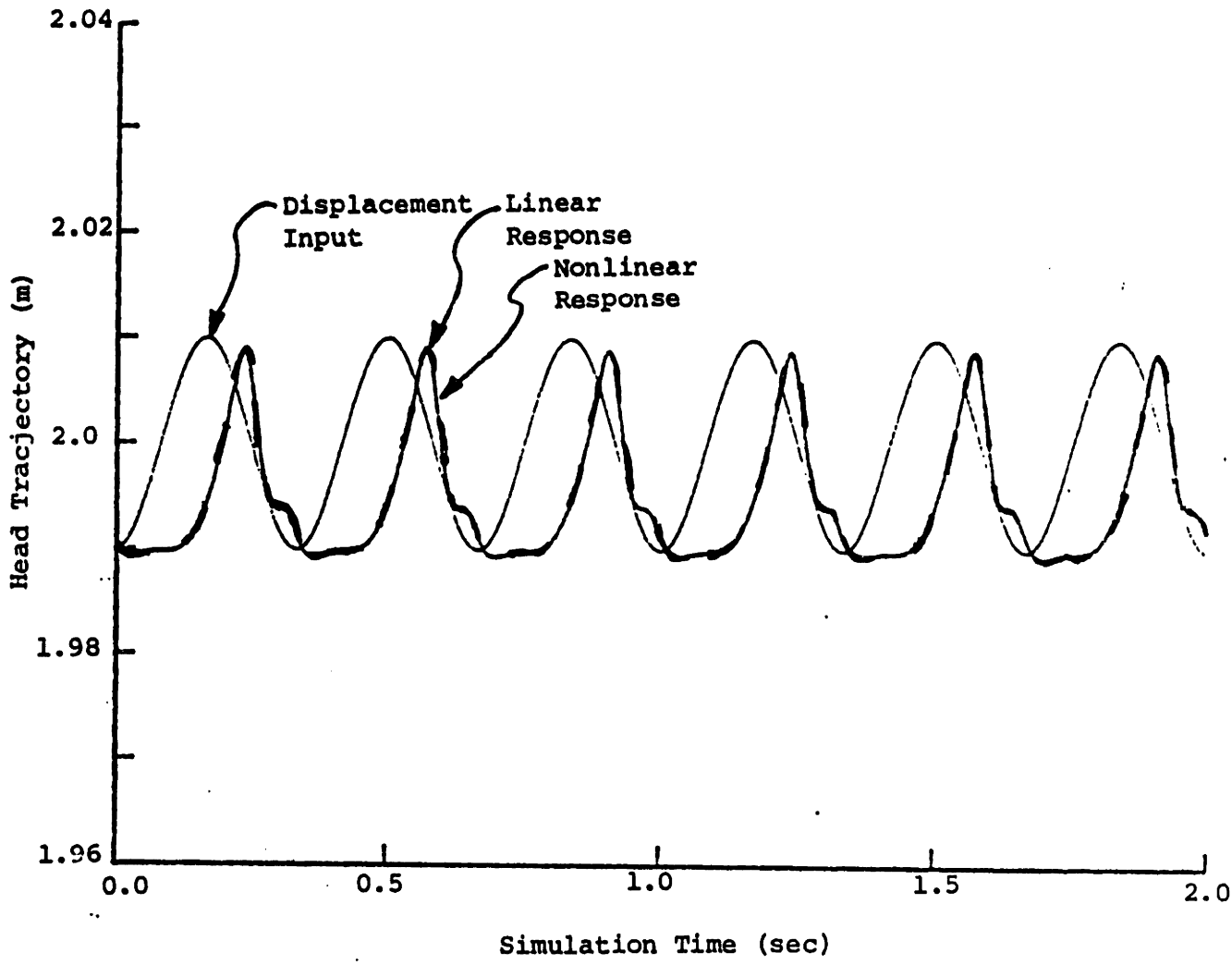

FIGURE 2.11: MODEL COMPARISON AT 3 Hz FOR $\pm$ 1 cm

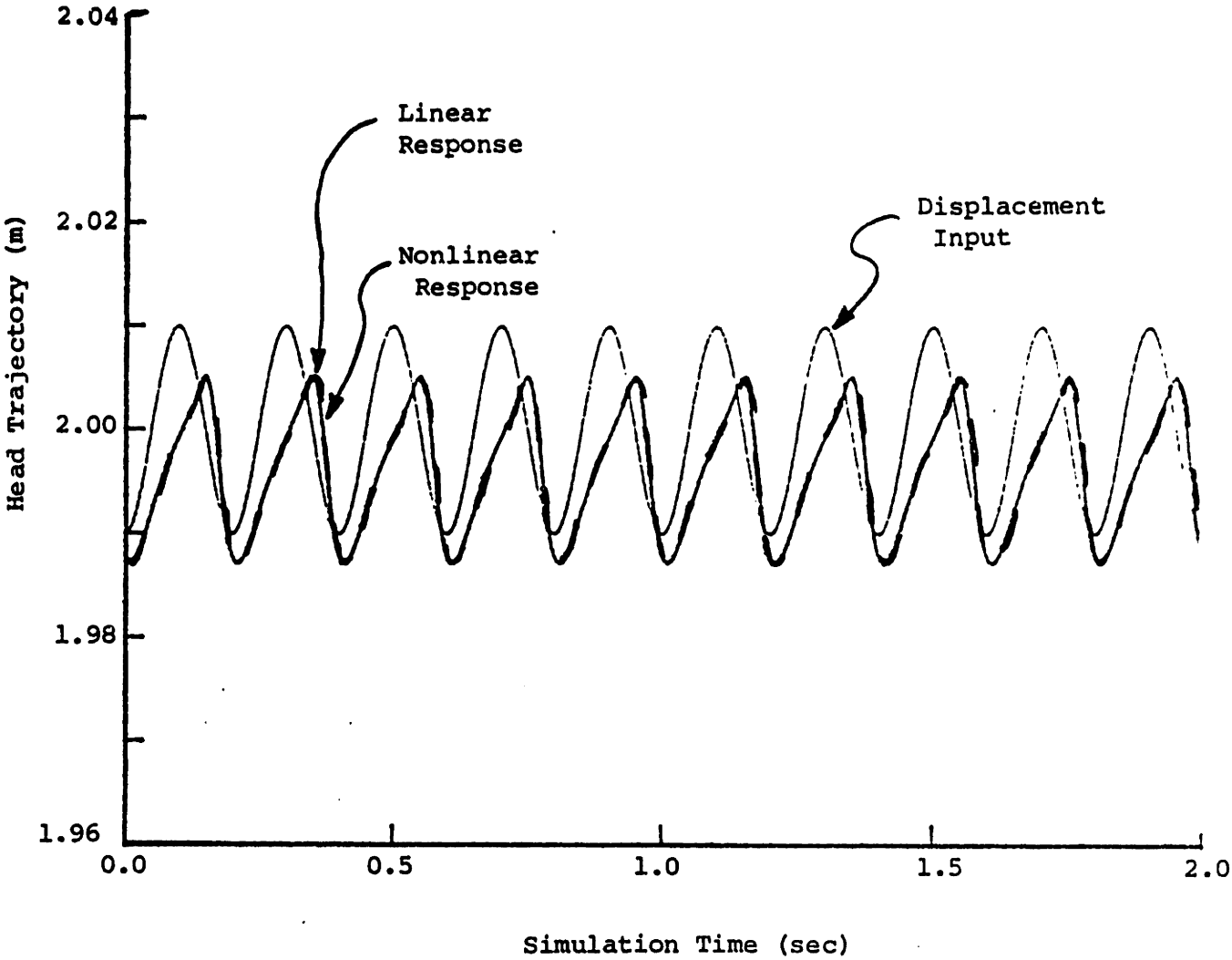

FIGURE 2.12: MODEL COMPARISON AT 5 Hz FOR $\pm$ 1 cm

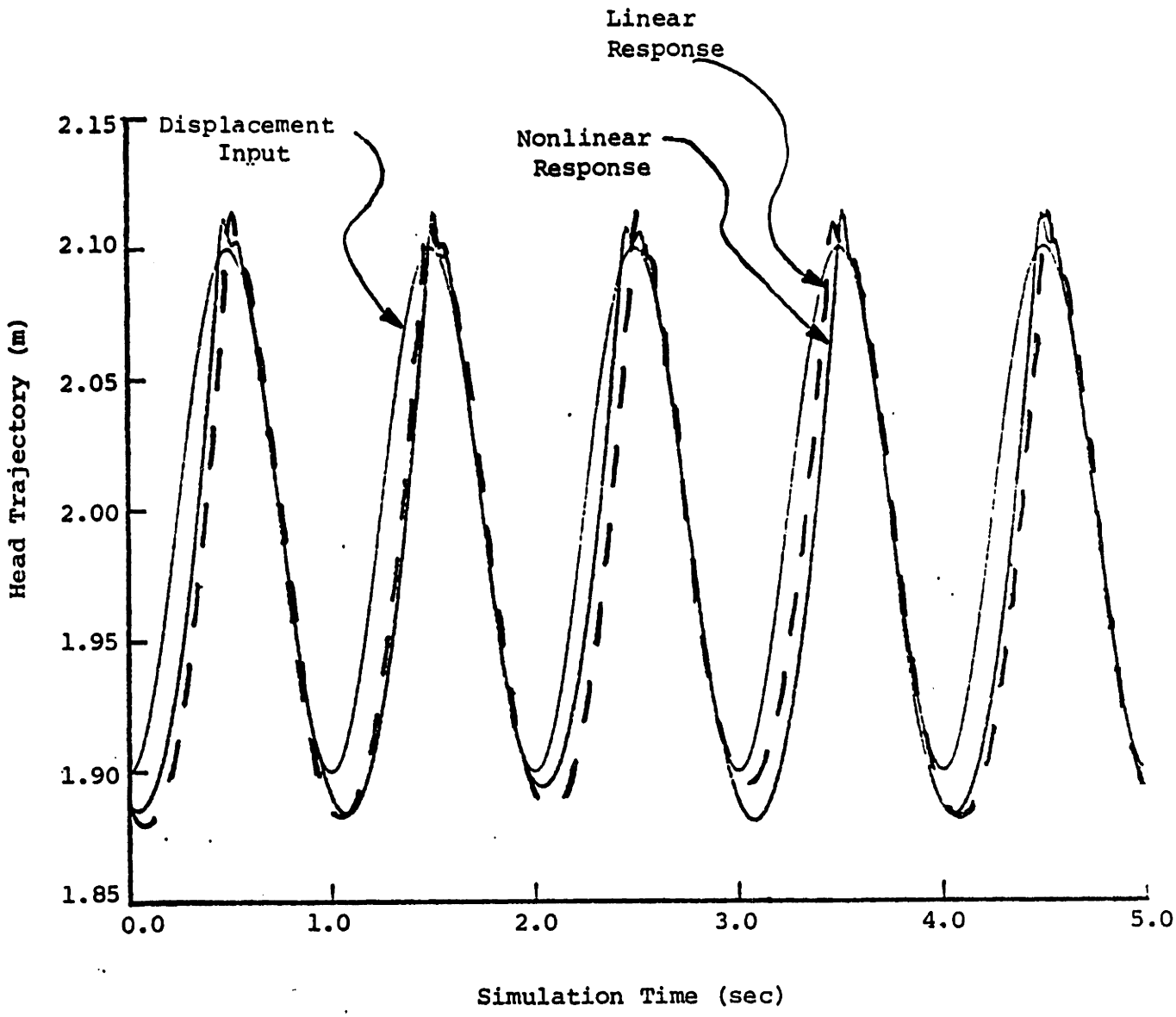

FIGURE 2.13: MODEL COMPARISON AT 1 Hz FOR $\pm$ 10 cm

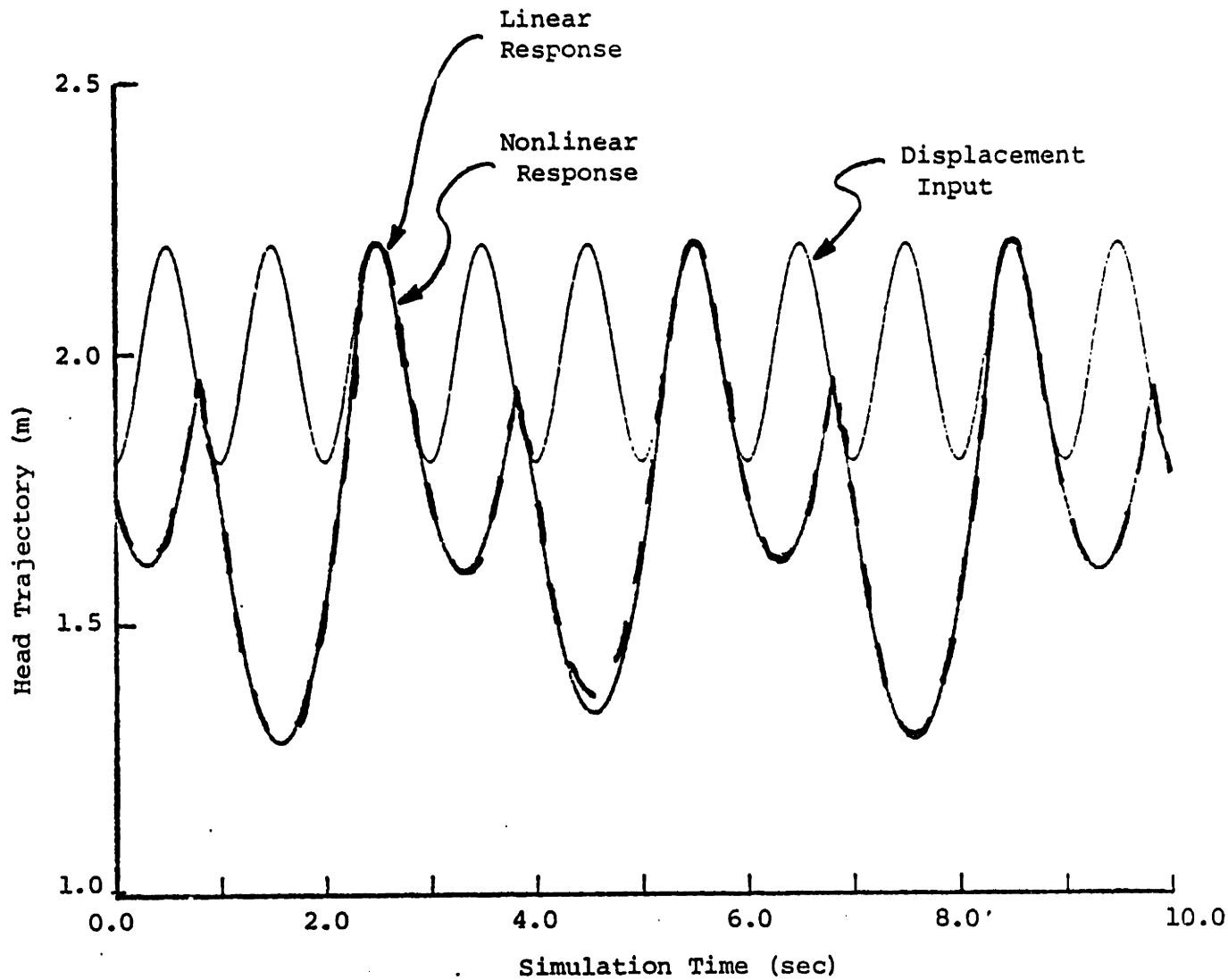

FIGURE 2.14: MODEL COMPARISON AT 1 Hz FOR $\pm$ 20 cm

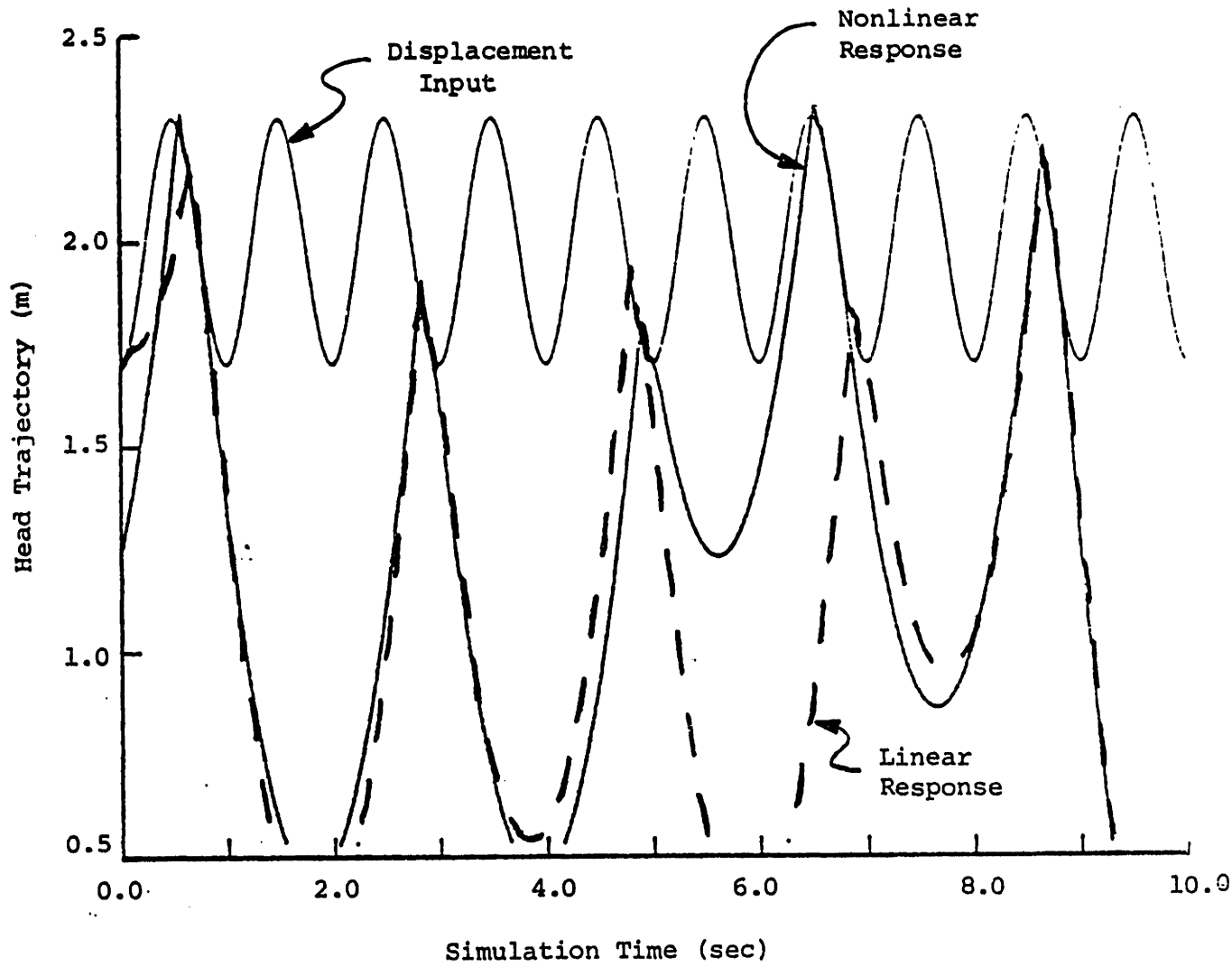

FIGURE 2.15: MODEL COMPARISON AT 1 Hz FOR $\pm$ 30 cm

linear model no longer provides a good representation of pantograph response. For typical pantograph catenary interaction the frequency and amplitude of disturbances are in a range which often allows use of the linear model.

Turning to the stop nonlinearity incorporated in the head suspension, two plots, Figure 2.16 and 2.17, indicate the advantage of the purely linear head suspension over the head suspension composed of the stop and break-away elements. Figure 2.16 shows the head trajectories to a sinusoidal input (dotted curve) of both suspension types at 1 Hz with amplitude 10 cm; the response which incorporates the stop suspension (dashed curve) has longer periods of loss-of-contact and larger displacements than the response which incorporates the linear suspension (solid curve). Figure 2.17 indicates the contact force for both cases; the upper curve shows the stop characteristic's force response, while the lower curve shows the linear characteristics force response. The stop suspension contact force is progressively growing, yet not too different from linear case.

The effects of coulomb friction in the head suspension is detailed in Figures 2.18 and 2.19. Three cases of coulomb friction (i.e. 0, 10 N, 20 N) are considered. With reference to the head trajectories of Figure 2.18, the solid curve pertains to no friction, while the dashed curve pertains to 10 Newtons of coulomb friction, and the double dashed curve representing the pantograph head trajectory has 20 Newtons of coulomb friction. As coulomb friction is increased less desirable tracking response occurs as signified by the larger displacements of the 20 Newton case (double dashed curve). Figure 2.19, contact forces for the three

cases, shows that coulomb friction causes larger spike values of contact force.

The effects of coulomb friction at the base pivot are studied in Figures 2.20 and 2.21, head trajectories and contact forces respectively. Three cases of coulomb friction (i.e., 0, 10 Nm, 20 Nm) in the frame are considered. As seen by Figure 2.20 for all amounts of friction there is little effect and similar trajectories occur, and Figure 2.21 supports this by showing peak values of contact force are approximately 1000 Newtons for all amounts of friction.

Finally, a simulation was run that included all of the baseline nonlinearities (i.e., frame geometry, head suspension stop element, and coulomb friction for head suspension and base pivot of 10 N and 1 Nm respectively). The two trajectories (dashed curve for baseline nonlinearities) plotted in Figure 2.22 indicate that multiple suspension element nonlinearities compound the undesirable response. As expected Figure 2.23 demonstrates large contact force values for the case including all the baseline nonlinear elements.

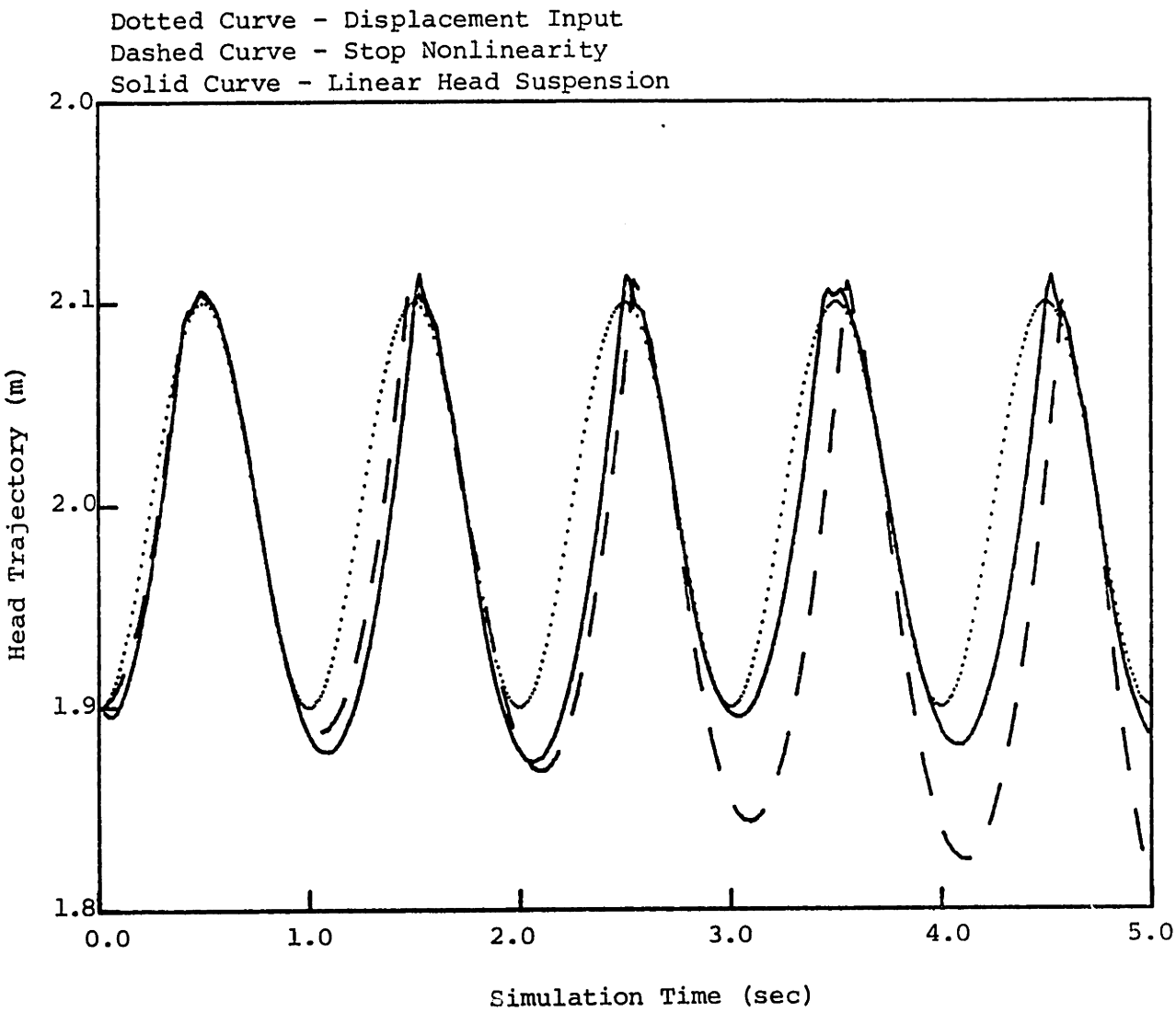

FIGURE 2.16: BEHAVIOR WITH HEAD SUSPENSION STOP

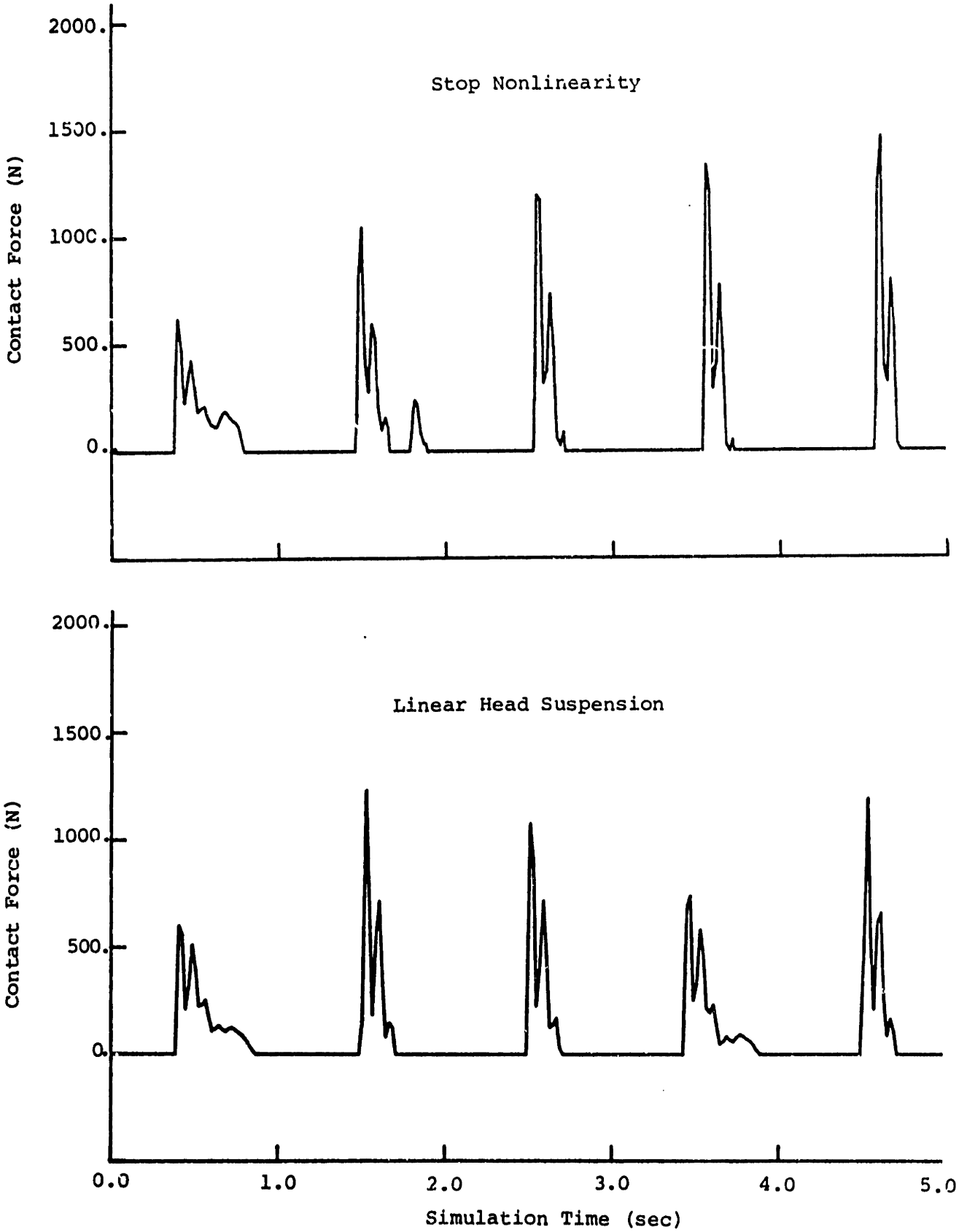

FIGURE 2.17: CONTACT FORCE WITH HEAD SUSPENSION STOP

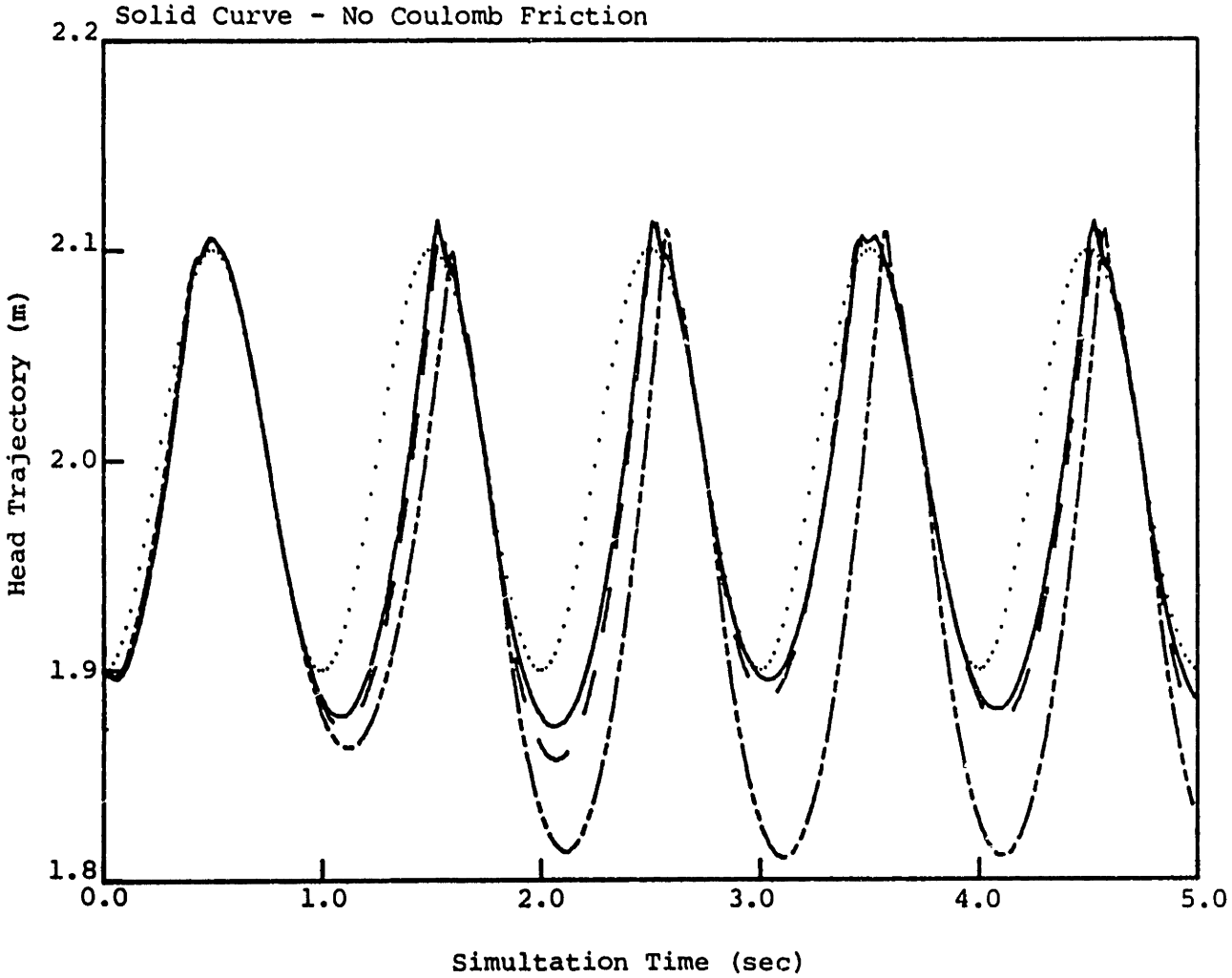

FIGURE 2.18: BEHAVIOR WITH HEAD SUSPENSION COULOMB FRICTION

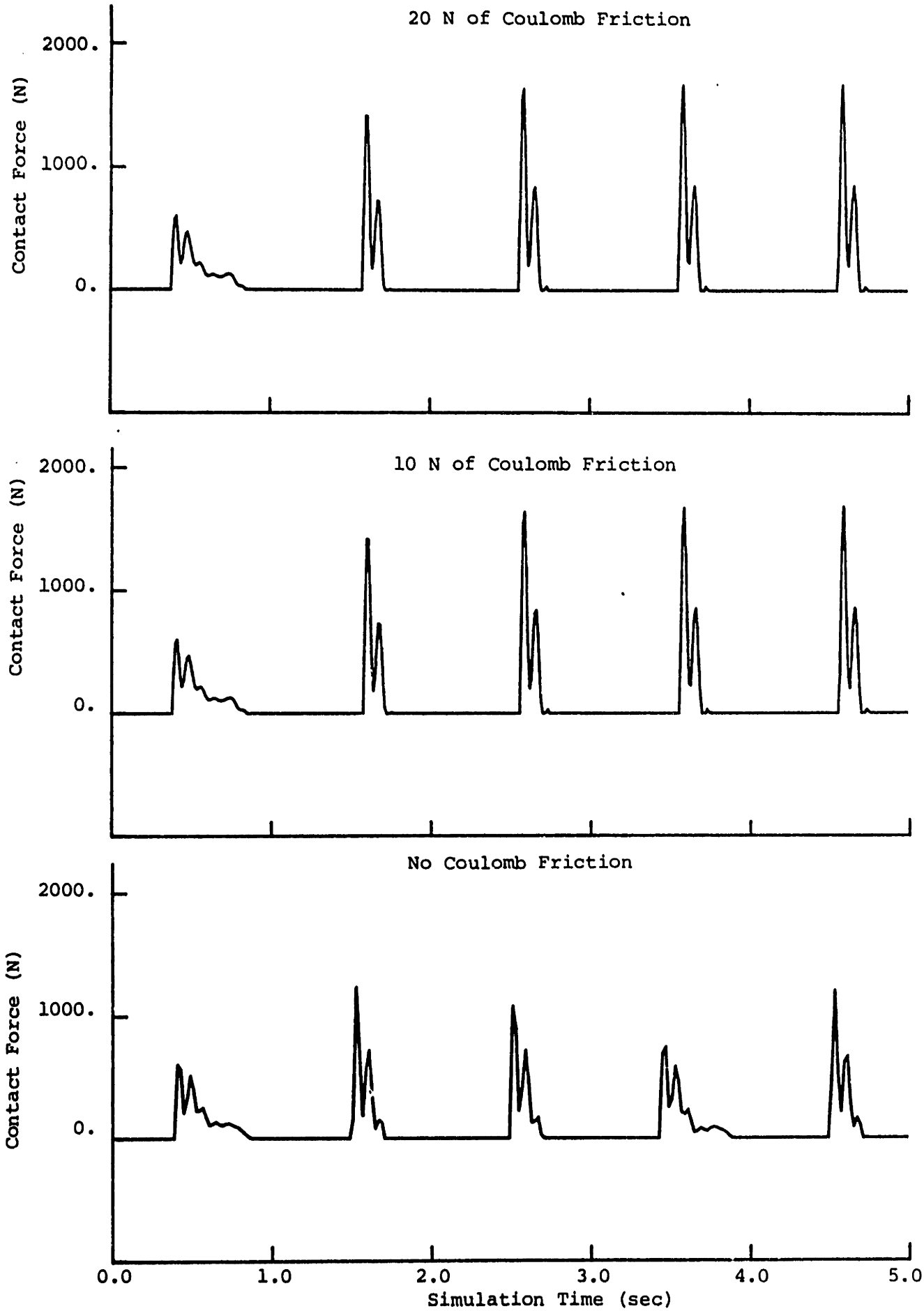

FIGURE 2.19: CONTACT FORCE WITH HEAD SUSPENSION COULOMB FRICTION

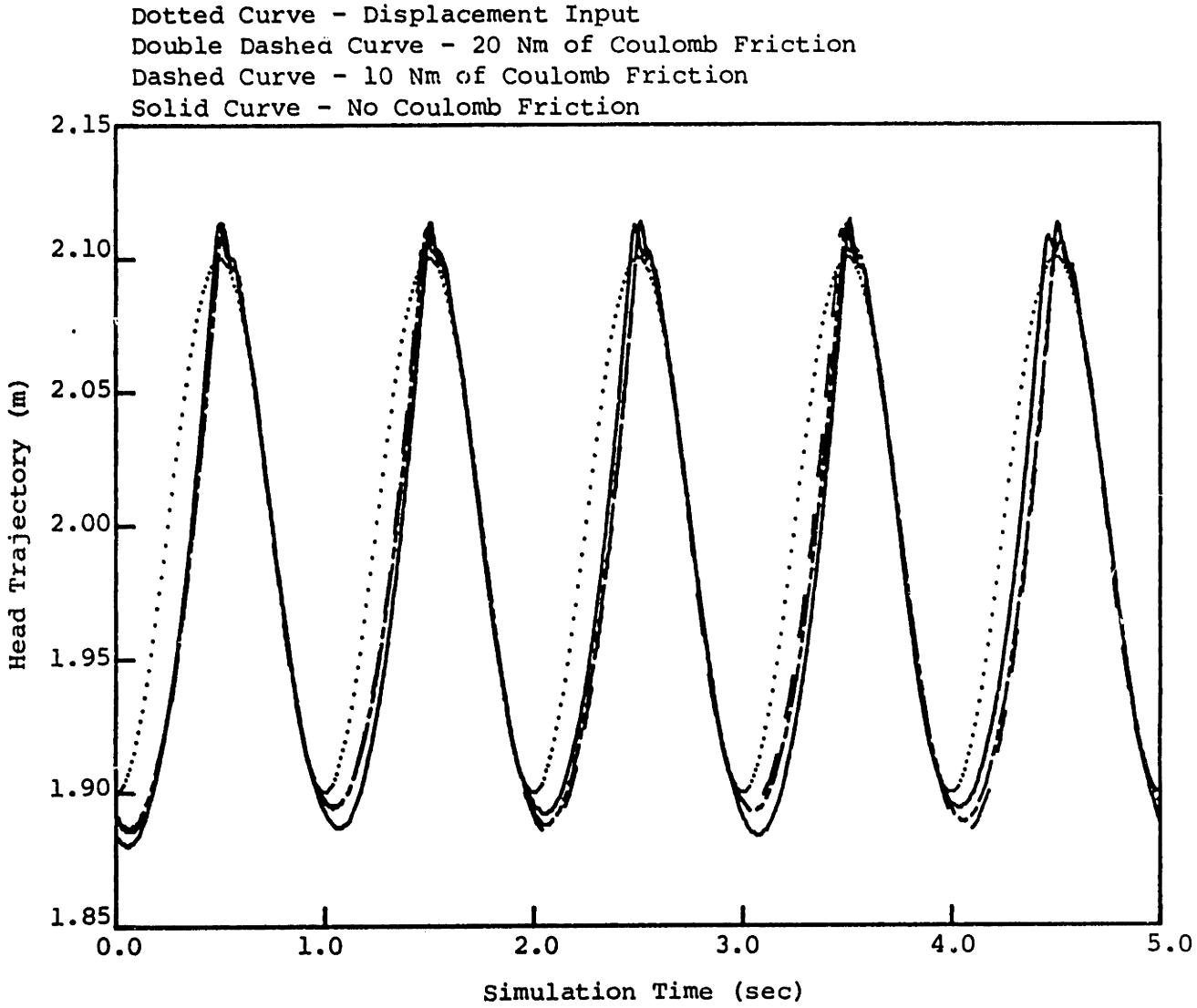

FIGURE 2.20: BEHAVIOR WITH BASE PIVOT COULOMB FRICTION

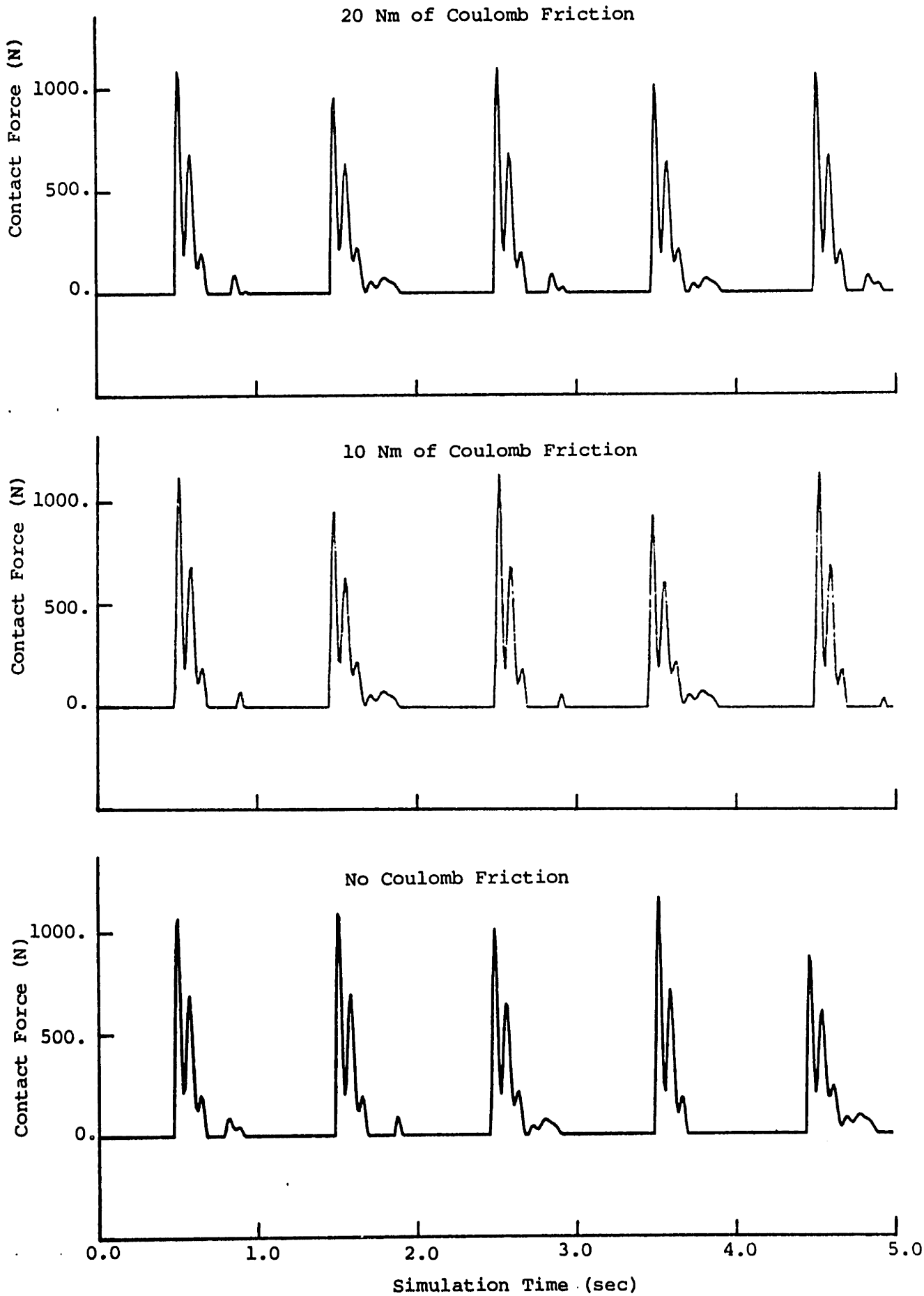

FIGURE 2.21: CONTACT FORCE WITH BASE PIVOT COULOMB FRICTION

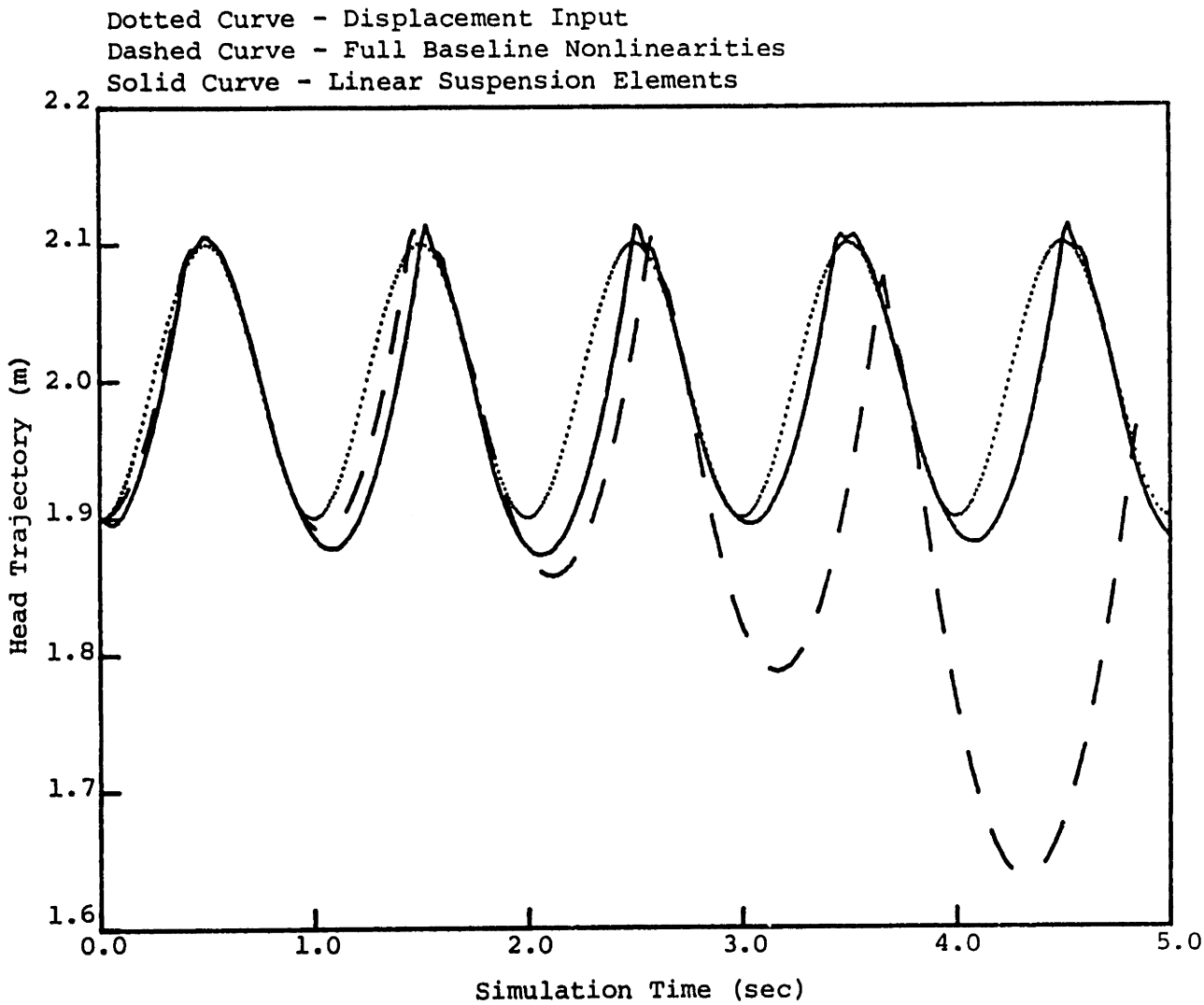

FIGURE 2.22: BEHAVIOR WITH BASELINE NONLINEARITIES

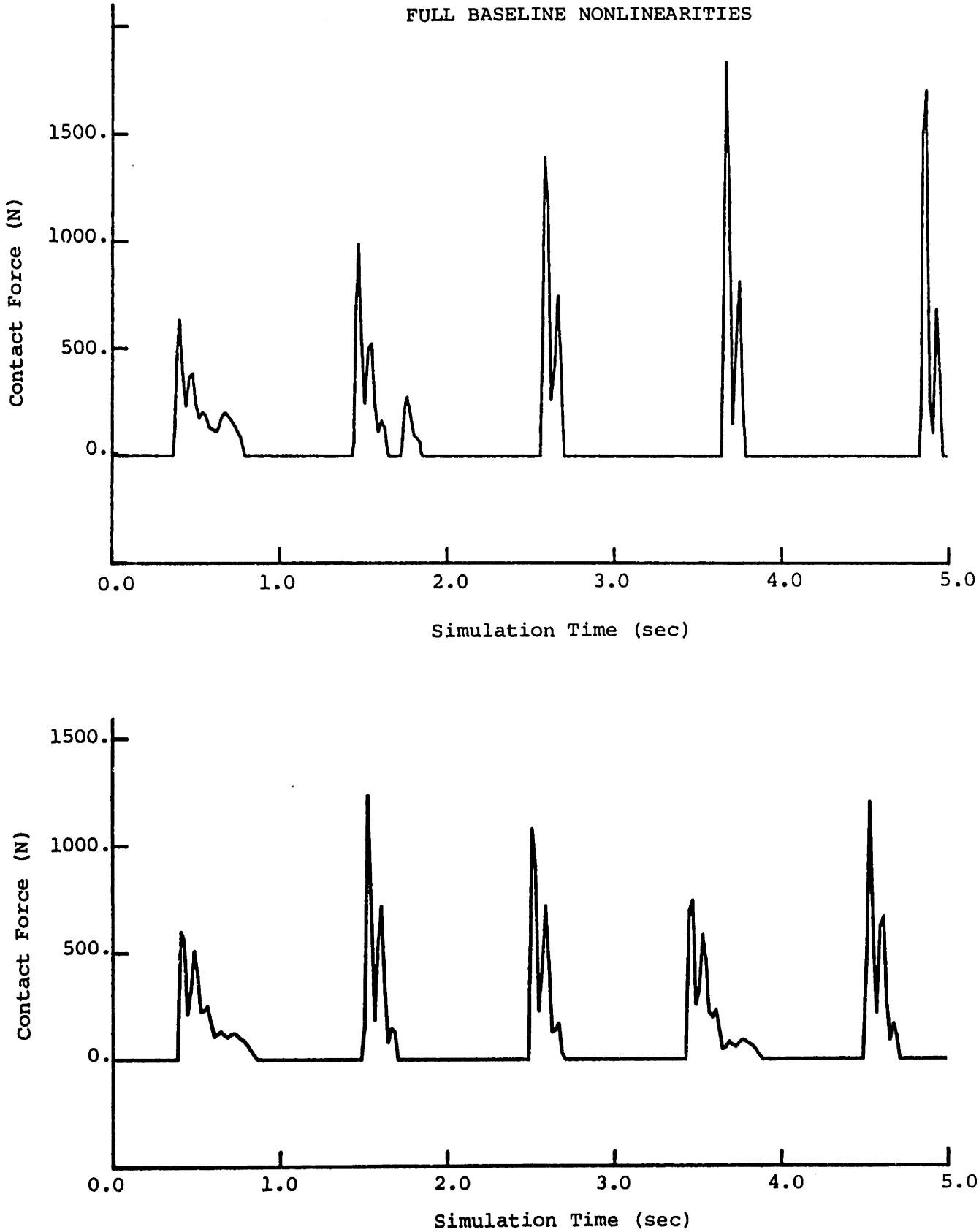

FIGURE 2.23: CONTACT FORCE WITH BASELINE NONLINEARITIES

CHAPTER 3

TEST PANTOGRAPH ANALYTICAL AND EXPERIMENTAL PERFORMANCE

3.1 Description of Test Pantograph

In this Chapter the results of an experimental evaluation of a test pantograph are discussed. The speciman is an August Stemman Pantograph Type BS129 (frame 1972) which has been installed at the Transportation Systems Center for evaluation. The test pantograph is shown schematically in Figure 3.1.

The gross motion of the test pantograph is dominated by the scissors action of the frame. The frame moves symmetrically about a center symmetry line, as the control bar moves vertically on this line. From the control bar location a suspension is attached supporting the head structure. This head suspension has no dynamic effect unless a 260 N compressive force across the head suspension is exceeded. Thus, this characteristic of the pantograph results in only gross motion of the frame during operation unless large irregularities occur, at which point the head suspension has a significant role in the tracking behavior.

Geometric and inertial parameter values determined directly from disassembly and component measurement of the pantograph are summarized in Table 3.1.

All lengths were measured explicitly during disassembly. The mass and center-of-mass of each member comprising the upper link was noted, and then the effective mass and center-of-mass for the overall upper link was computed. The lower link was assumed uniform in density, therefore its center-of-mass is half of its total length. The small moment arm r_b,

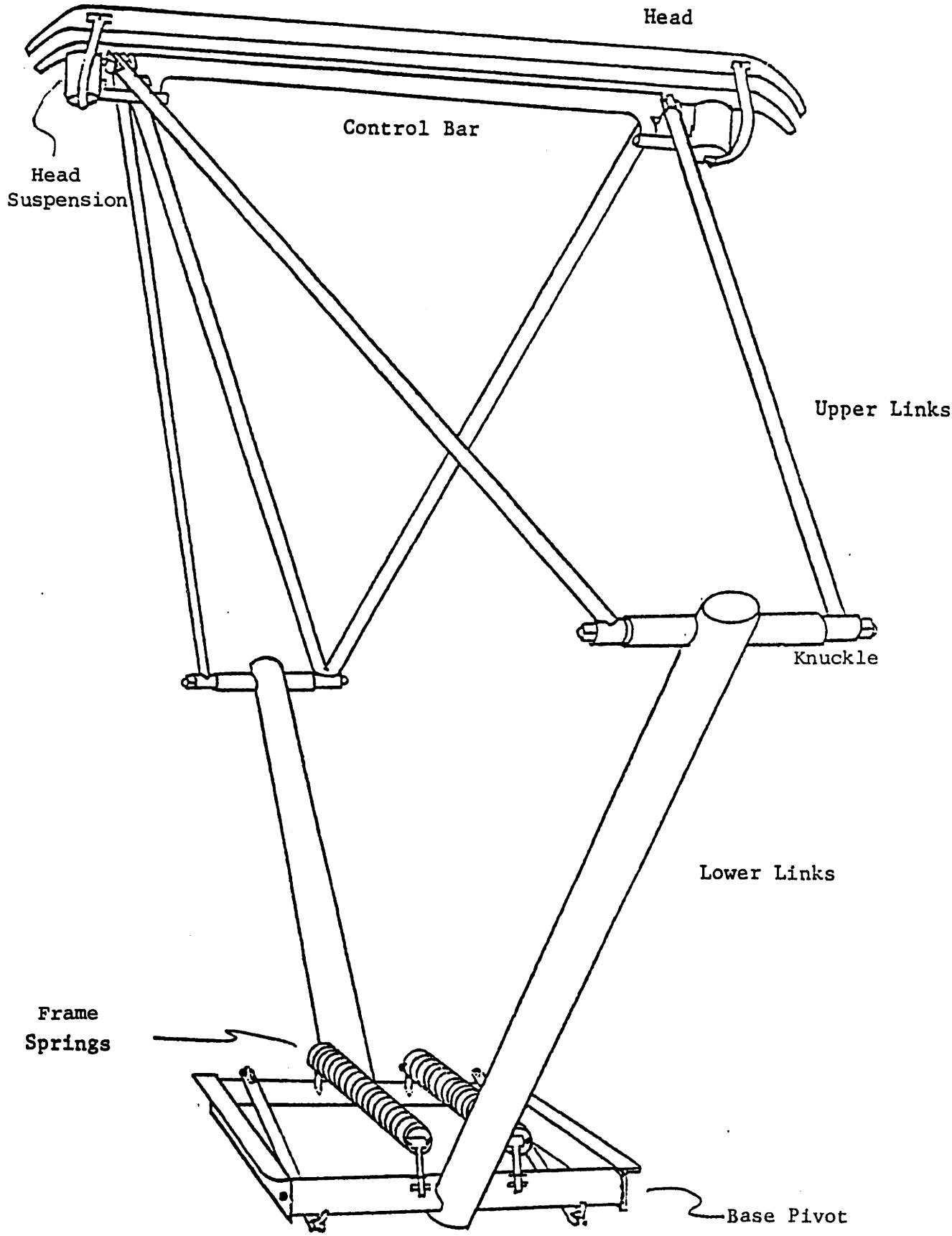

FIGURE 3.1: August Stemman Pantograph
Type BS129 (1972)

TABLE 3.1

PARAMETER VALUES AND DESCRIPTION
FOR
AUGUST STEMMAN PANTOGRAPH

ℓ_1	=	1.640 m,	length of lower link
ℓ_2	=	2.1415 m,	length of upper link
r_1	=	0.823 m,	distance to c-of-m on lower link from base pivot (assumed uniform)
r_2	=	0.974 m,	distance to c-of-m on upper link from knuckle
r_b	=	0.130 m,	moment arm length about point G to where force F_b acts
offst	=	0.500 m,	distance to base pivot from line of symmetry
θ_o	=	0.97 rad,	angle between moment arm r_b, and centerline of lower link
m_1	=	30.85 kg,	mass of lower link (TSC report data)
m_2	=	19.10 kg,	mass of upper link
m_h	=	13.10 kg,	mass of head
m_c	=	7.075 kg,	concentrated control bar mass at top of frame attached to upper link
m_k	=	5.72 kg,	concentrated knuckle mass attached to lower link
I_1	=	7.305 kgm,	moment of inertia for lower link about c-of-m (calculated)
I_2	=	7.650 kgm,	moment of inertia for upper link about c-of-m (calculated)
K_h	=	9580.0 N/m,	head suspension spring rate
K_b	=	65000.0 N/m,	spring rate for base frame spring
B_b	=	$10.0\frac{Nm}{rad/s}$,	rotational damping at base pivot (nominal estimate)
B_{bc}	=	1.0 Nm,	rotational coulomb friction at base pivot
B_h	=	$300.0\frac{N}{m/s}$,	head suspension damping rate (design data estimate)
B_{hc}	=	10.0 N,	head suspension coulomb friction

TABLE 3.1: Continued

BRKWY	= 260.0 N,	precompression force in head suspension assembly, amount of force required to separate head from frame
PRETEN	= 11650.0 N,	pretension force in base spring, (design data estimate)
g	= 9.81 m/s^2,	gravity

and angle θ_o, establishing the point at which the base spring force acts, were measured carefully reducing any error corresponding to these sensitive parameters.

All pantograph member masses were measured directly during disassembly, excepting the lower link mass. The lower link mass was taken from reference [15] with a small estimated amount of mass (10%) subtracted due to the mass surrounding the base pivot. The small nominal mass at the base has a minor effect on the pantograph dynamics. Moments of inertia, I_1 and I_2, about the centers-of-mass for the lower and upper links have been calculated considering slender uniform rods.

Head suspension springs were isolated and force deflection curves plotted to determine the head suspension spring rate K_h in the break-away configuration. With the same procedure the amount of force (BRKWY) required to initiate movement of relative parts within the precompressed head suspension unit was determined. The head suspension unit consists of a precompressed spring held against stops, as shown schematically in Figure 3.2. In order to model the stop characteristic and break-away characteristic the head was connected to the frame with a nonlinear suspension configuration as shown in Figure 3.3. The z-coordinate describes the relative movement of the head from the control bar, while the y_c-coordinate describes the absolute motion of the control bar.

The nonlinear stiffness force deflection law is shown in Figure 3.4. The force deflection plot falls into three regions. In Region I, the suspension is very stiff $K_{h,stf}$ (200 kN/m) because the pantograph head contacts the stops, and therefore, essentially no relative movement occurs except for structural elasticity. When the force across the sus-

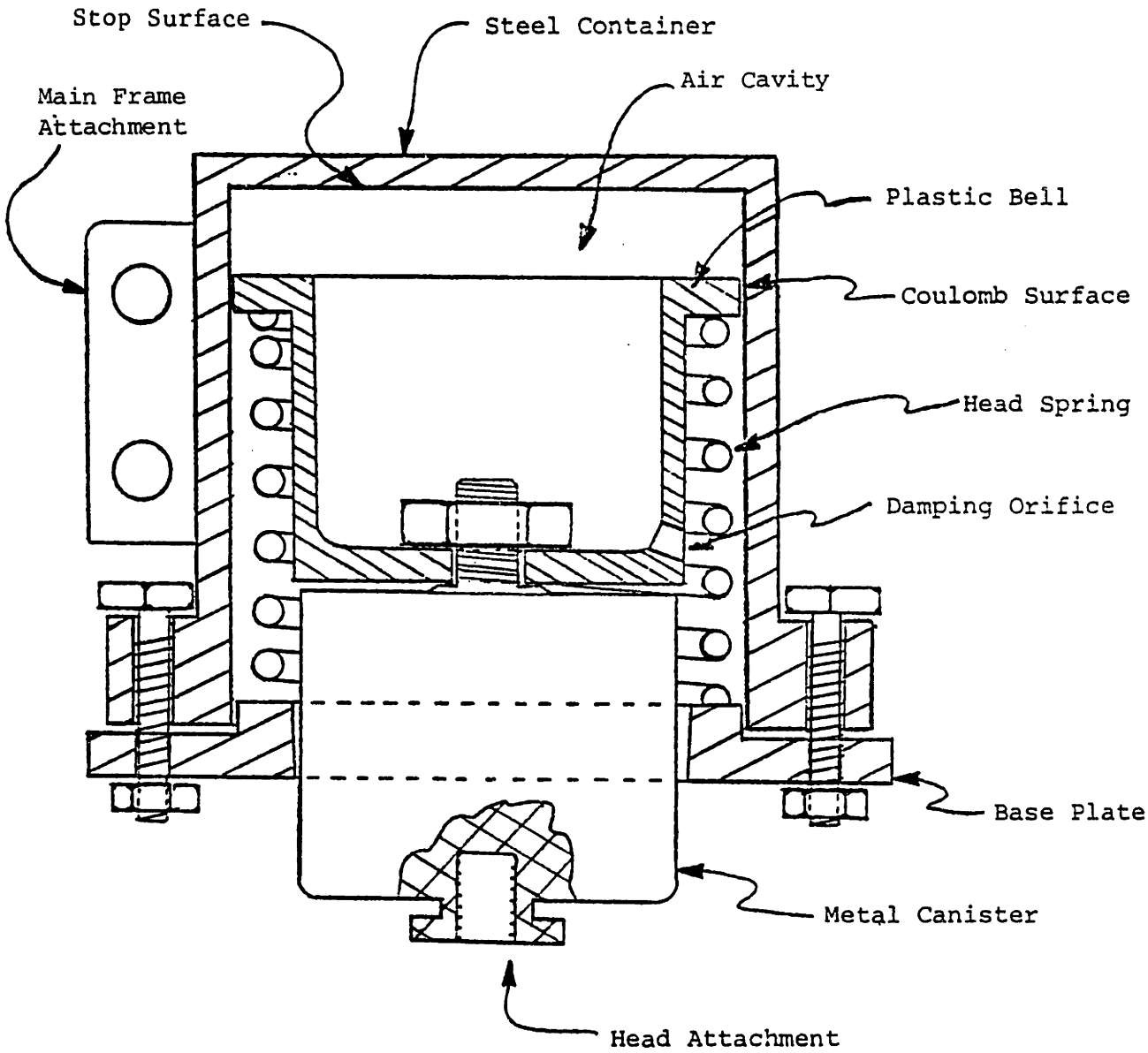

FIGURE 3.2: CUT-AWAY OF SPRING-PLUNGER-DAMPER HEAD SUSPENSION UNIT

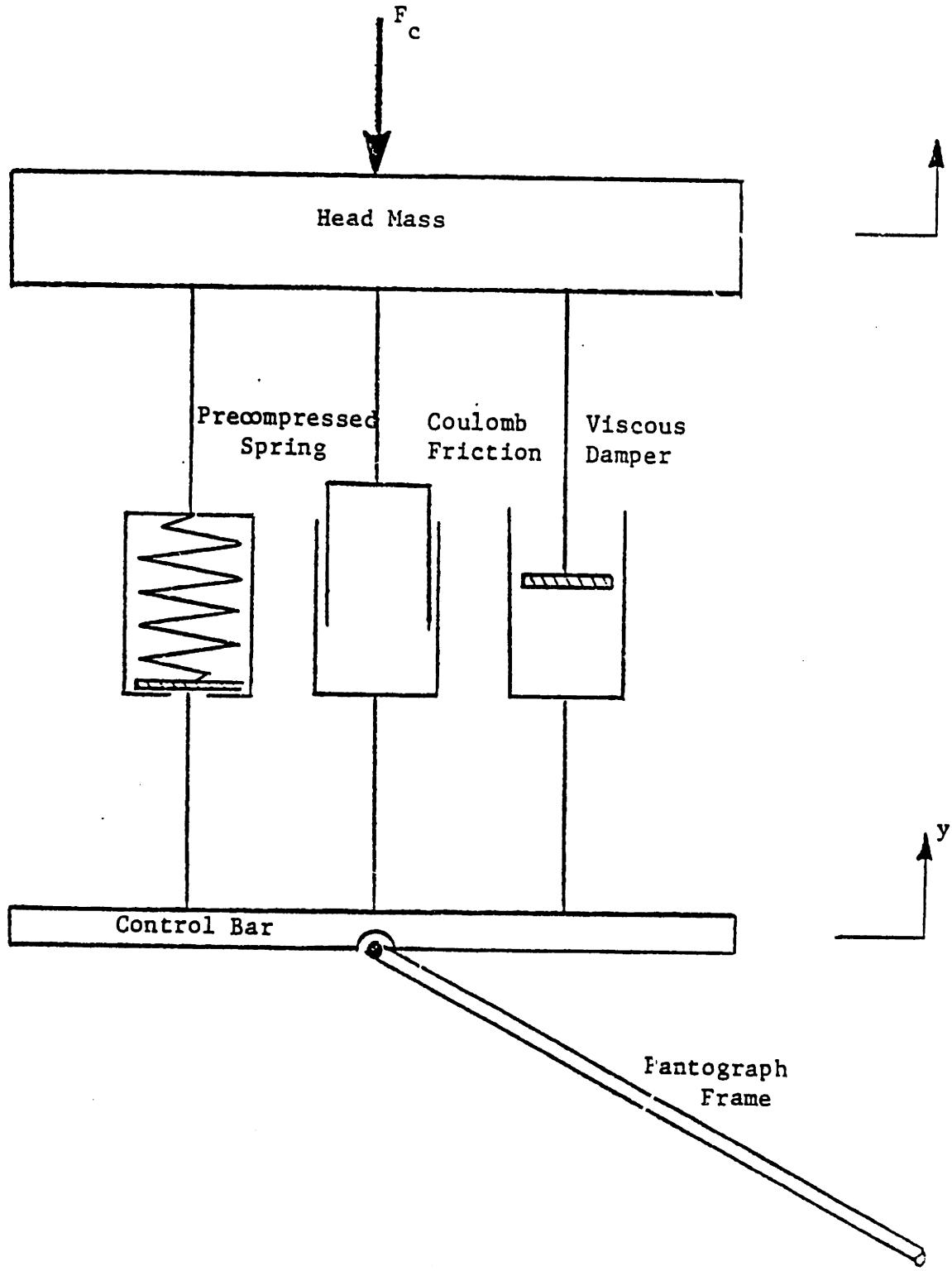

FIGURE 3.3: MODEL OF TEST PANTOGRAPH HEAD SUSPENSION

pension exceeds 260 N, the head suspension stiffness is dependent only on the intentional spring stiffness K_h (9580.0 N/m), and operation occurs in Region III. Region II is the smooth transition between the two stiffness values, and occurs within 1.0 mm, as indicated in Figure 3.4, exhibiting no sudden discontinuities. As a result of the particular head stiffness behavior and during small force excitation the 260 N break-away force is rarely exceeded and relative head motion remains negligible, staying within 1.0 mm of movement. It is helpful to note that the soft spring region occurs for negative z displacement, and hence greatest motion will occur in Region III. Equations (3.1) use a linear-exponential-linear form with the appropriate constant values $F_{01} = 397.33$, $F_{02} = 263.15$, $B = 3038.6$, $z_o = 0.000378$ to satisfy the compressive head suspension force F_h in the three regions; that is:

$$\begin{array}{lll} \text{Region I,} & z > 0.1 \text{ mm} & F_h = F_{01} + K_{h,stf} z \\ \text{Region II,} & 0.1 \text{ cm} > z > 0.0 & F_h = F_{02} - e^{B(z+z_o)} \\ \text{Region III,} & z < 0 & F_h = K_h z + BRKWY \end{array} \qquad (3.1)$$

A nonlinear damping rate B_h, within the impact region, is also utilized to account for increased dissipation of energy upon impact of the head on the stops. The nonlinear damping characteristics are shown in Figure 3.5, and indicate a small nominal damping rate representative of break-away viscous damping due to air passing through the small orifice in the head suspension shown in Figure 3.2, and an increased damping rate corresponding to positive motion within the impact region. During break-away the damping is dominated by the nominal damping value.

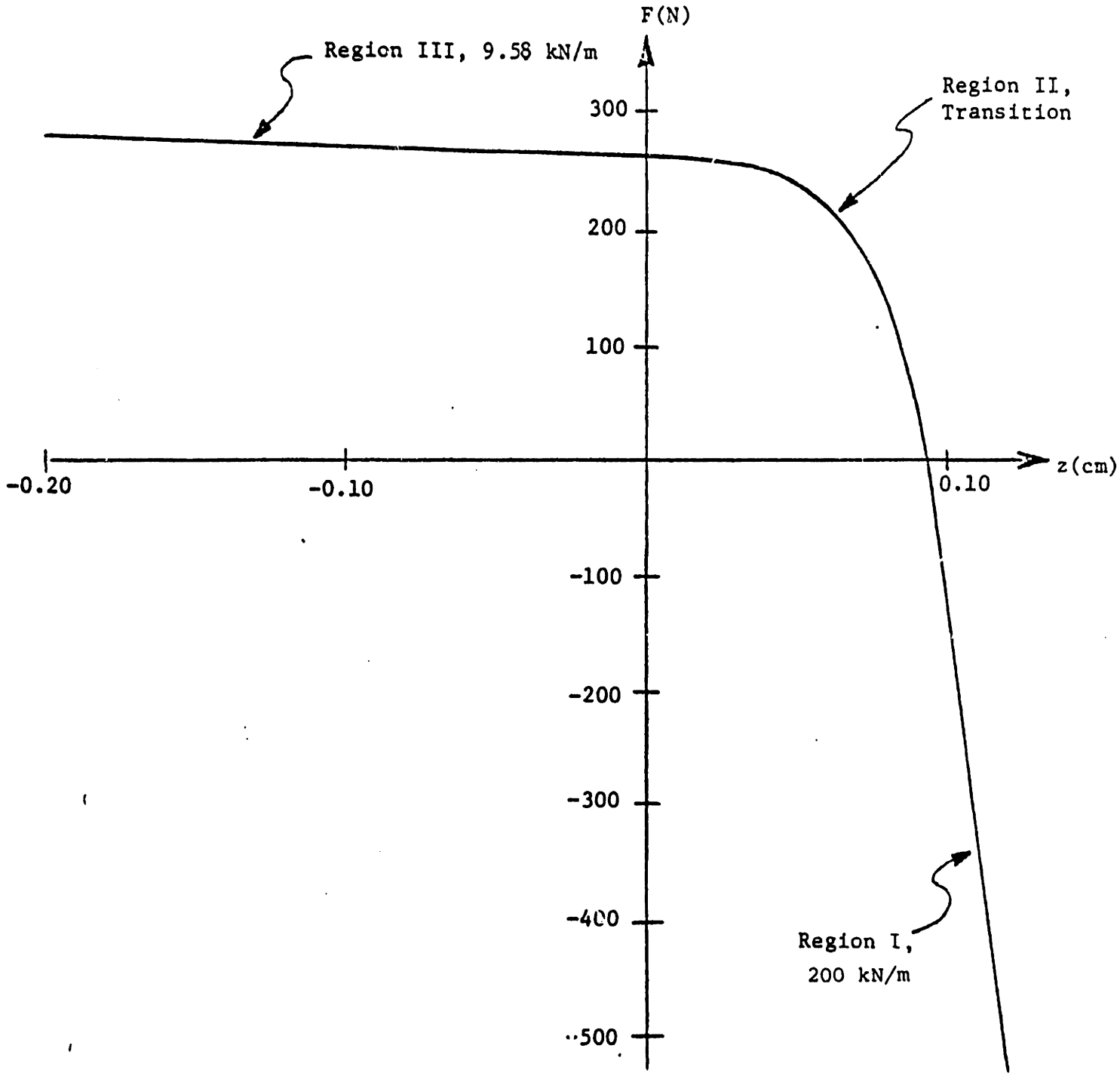

FIGURE 3.4: HEAD SUSPENSION FORCE-DEFLECTION CHARACTERISTICS

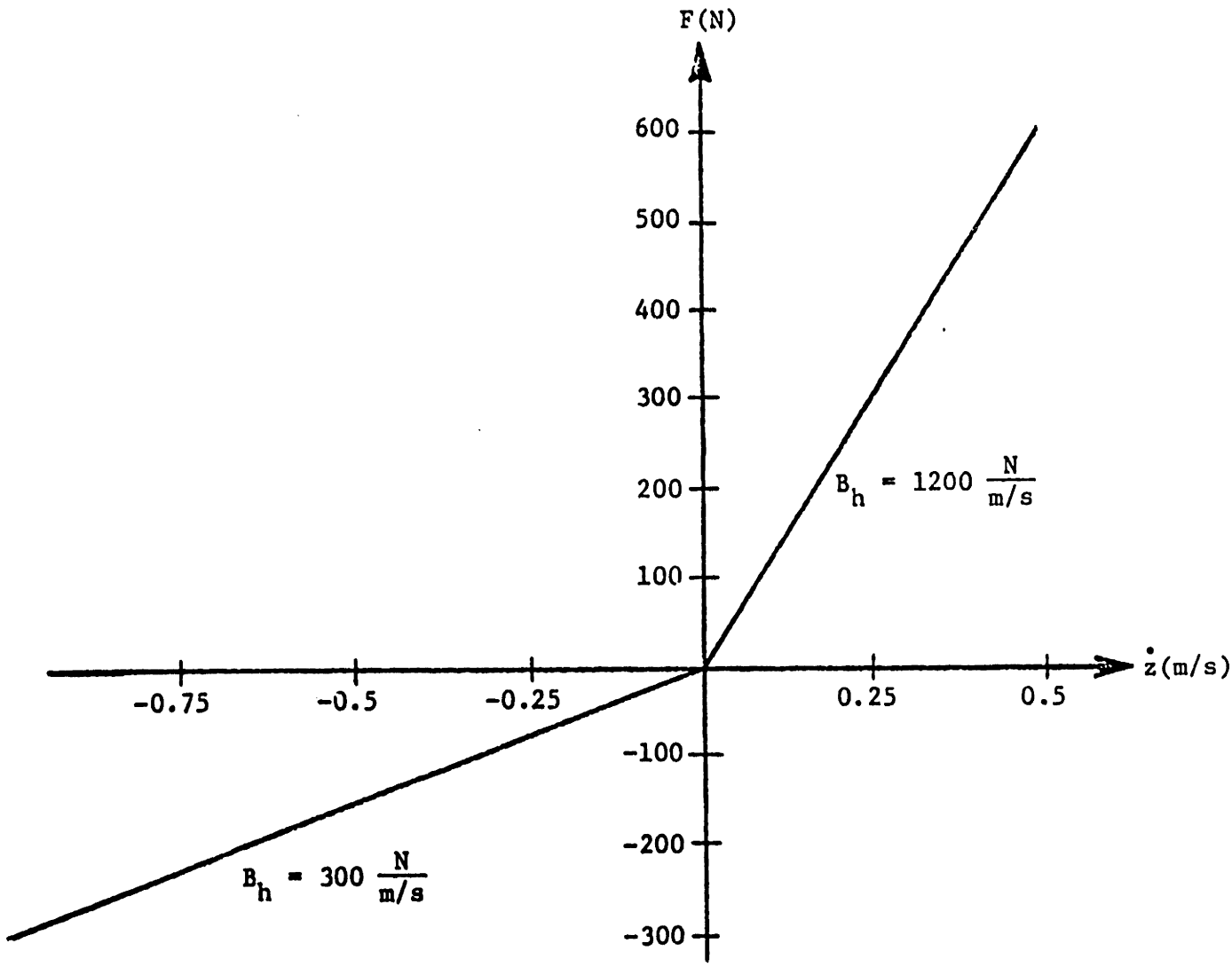

FIGURE 3.5: HEAD SUSPENSION DAMPING CHARACTERISTICS WITHIN IMPACT REGION

In addition, coulomb friction in the head suspension is utilized and is estimated from break-away tests performed on the test pantograph. It was found to be approximately 10 N.

The base spring K_b operates on the previously described moment arm r_b. Its spring rate is 65,000 N/m and has a pretension (PRETEN) of 11,650 N when the moment arm is vertical. A small nominal rotational damping rate B_b and rotational coulomb friction B_{bc} located at the base pivot are included and do not have much effect on the pantograph tested.

3.2 Experimental Test Facility

The dynamic characteristics of the test pantograph have been measured experimentally using facilities at the transportation Systems Center. The facility contains a Gilmore hydraulic excitation unit providing the displacement input to the pantograph head. The unit provides a sinusoidal displacement input with amplitudes from 0 to 5 cm peak-to-peak.

The analytical model consists of two degrees-of-freedom, frame motion and absolute head motion. Hence, it is of interest to monitor the frame response and relative displacement of the head with respect to the frame which yields absolute dynamic information on the head. Therefore, the ram input, relative head displacement, and frame motion have been measured.

One premise of the testing schedule is that the catenary wire response is below 20 Hz, and as discussed in Refs.[1,2] only substantial amplitudes occur below 10 Hz. Within this frequency range of interest, individual link resonances may become of concern; hence, capability to determine link vibration behavior is provided by placement of accelerometers at selected frame locations, such as the center of the most flexible member.

Figure 3.6 illustrates the instrumented pantograph which includes a:

Hydraulic Ram	-	providing displacement input
Ram LVDT	-	measuring displacement input
Head LVDT	-	measuring relative head displacement
DCDT	-	measuring frame motion
Base LVDT	-	providing a check on frame motion
Accelerometer	-	providing link vibration behavior

To collect the dynamic data the following experimental procedure was followed:

*Rigidly attach pantograph head to hydraulic ram

*Excite the head over a range of frequencies (1 to 20 Hz)

*Obtain steady operating conditions

*Record 20 seconds of data with the above mentioned instruments on 5 channels of tape

*Reduce data with A/D converter and computer analysis

With the center of the head rigidly attached to the hydraulic actuator, input displacement to the head was provided with amplitudes from 0.3 cm to 1 cm. The actuator provided a quasi sinusoidal input displacement with frequencies from 1 Hz to 20 Hz. The hydraulic ram input displacement was measured with an LVDT housed within the hydraulic unit. A Shavetz LVDT with a 5 cm stroke was implemented to measure displacement across the head suspension. A Collins DCDT with a 10 cm range was used to measure frame vertical motion at the control bar which only moves vertically. To provide a check on frame motion measurements, another Shavetz LVDT with a 1.25 cm stroke was installed at the base. The center of a link member was instrumented with a Columbia accelerometer to measure link vibration behavior.

Two recording techniques were employed: One was on-line strip chart recording, the other was FM recording on a 14 channel Racal recorder. The recorded data were later reduced to digital form with a

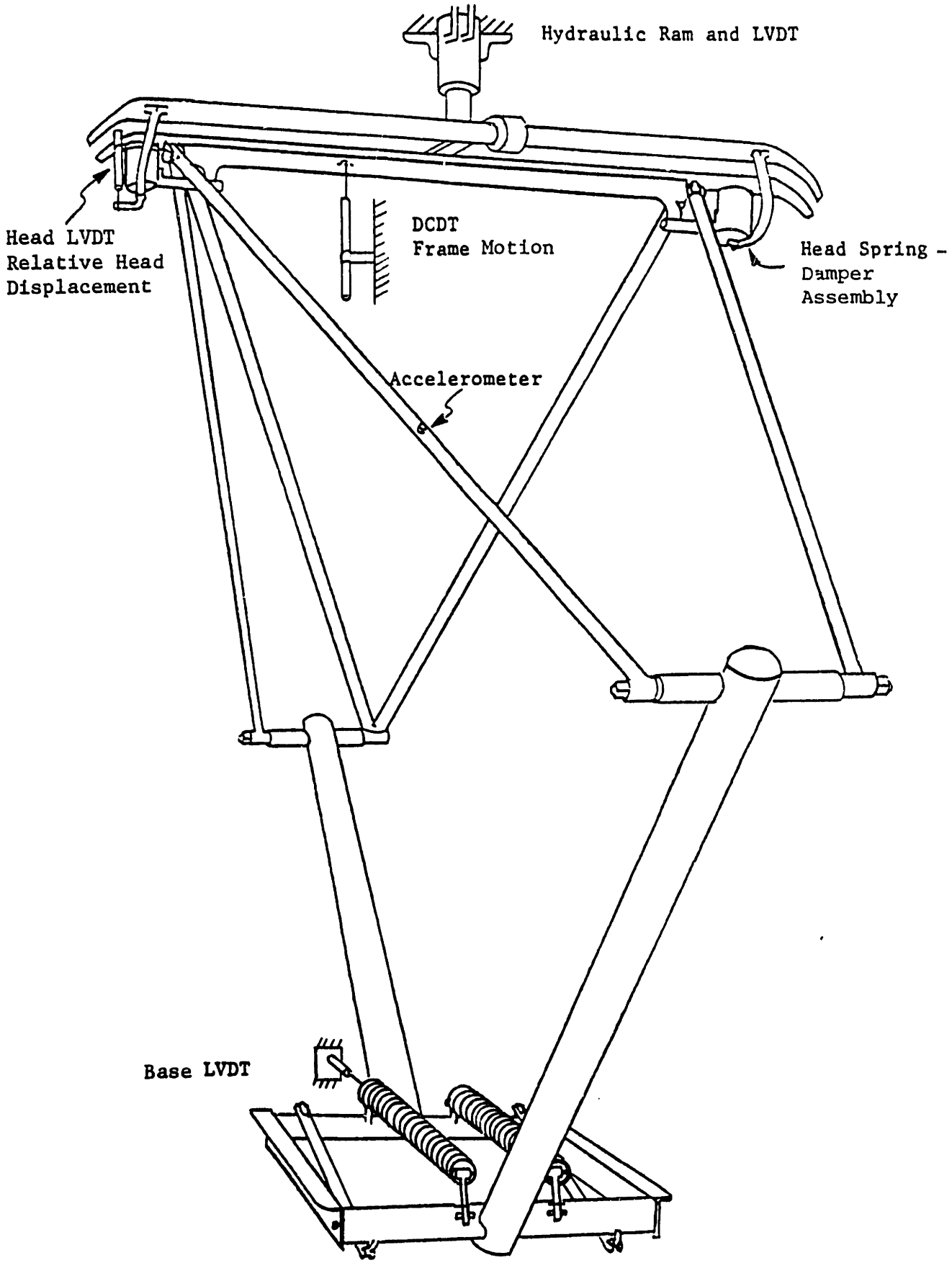

FIGURE 3.6: INSTRUMENTED AUGUST STEMMAN PANTOGRAPH

Datel A/D converter and stored on disks for further data analysis. In addition, final form strip chart displays and time histories were produced for each of the 20 frequencies tested. To identify the frequency content of the input and output displacements, spectral analysis was performed and is summarized in Section 3.4.

3.3 Static Performance

The static force-deflection relation for the pantograph has been given in Equation (2.3). The equilibrium load depends on the operating height and the configuration of the base spring. To provide control over the experiment the base spring tension has been adjusted to yield the nominal 90 N uplift force at an operating height of 2.0 meters. For this base spring configuration the theoretical force-deflection curve has been plotted in Figure 3.7.

Data collected on the test pantograph determining the equilibrium heights as a function of load is shown with horizontal bars in Figure 3.7. The horizontal bars are representative of all the equilibrium positions achieved for a given loading. By design the uplift force exerted by the pantograph is nearly constant at approximately 90 N. This constant force design, along with frame linkage hysteresis, accounts for the variety of equilibrium positions (i.e. horizontal bars) achieved for a particular loading. The characteristic is most easily noticed at a height of 1 meter where the theory predicts an almost constant force, in concurrence with the pantograph experimental data where a loading at any nearby height also tends to be in equilibrium. Over the complete range of data the analytical and experimental results are in close agreement. Additional parametric studies of the pantograph static performance

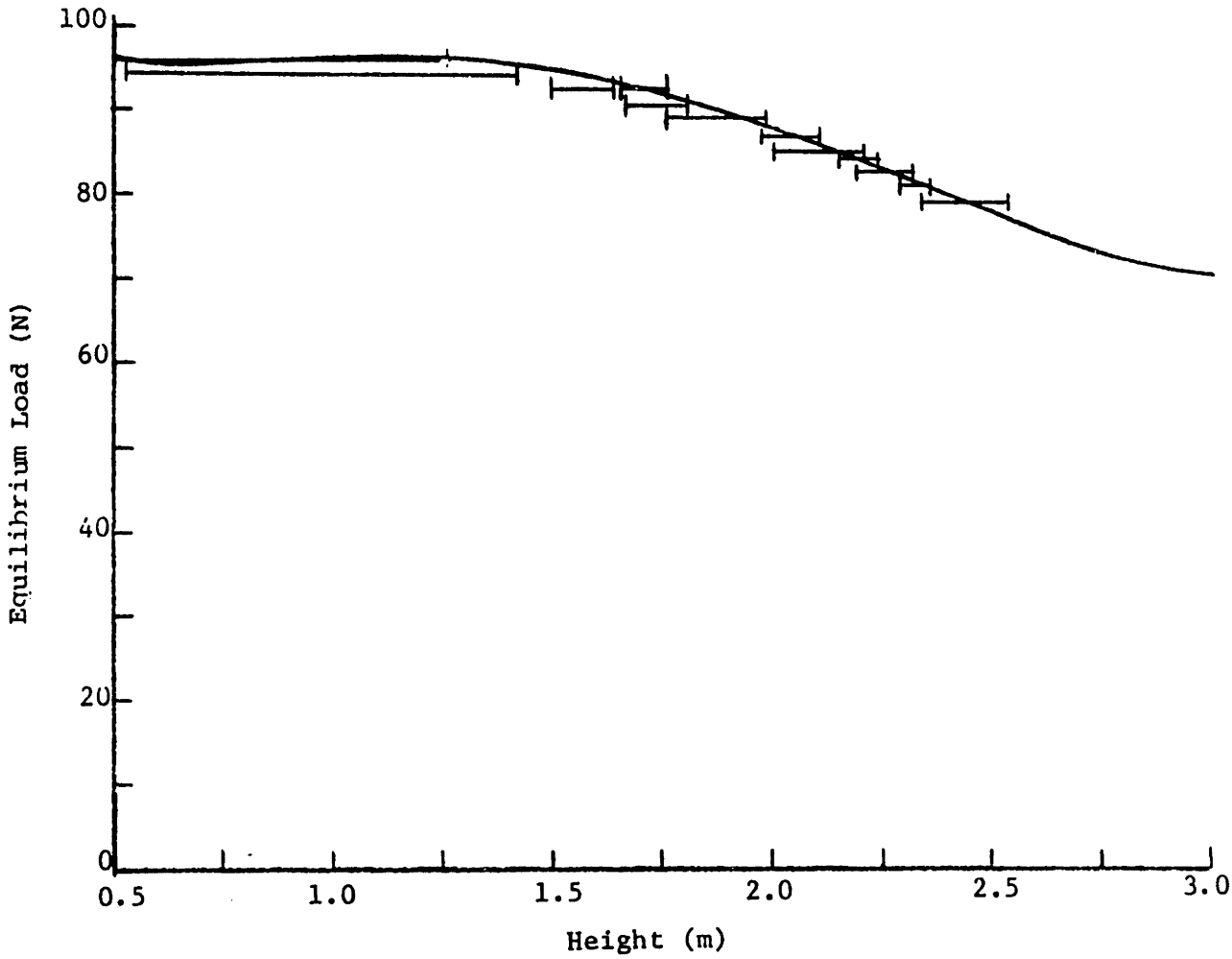

FIGURE 3.7: PANTOGRAPH THEORETICAL AND EXPERIMENTAL STATIC FORCE-DEFLECTION CHARACTERISTICS

have indicated that the force-deflection characteristic is sensitive to pantograph lengths. A variation in length of link members of more than 1% results in significant changes in the force-deflection curve, especially near the extremes of frame extension.

3.4 Dynamic Experimental Performance Data

Dynamic experimental data in the form of time histories of pantograph motion for fifteen frequencies are included in this section with corresponding theoretical plots computed using the nonlinear dynamic model. The data are summarized in Figures 3.8 through 3.22. The lower set of theoretical data may be compared with the upper set of experimental data. In either case, the top plot represents the input displacement of the ram, the center plot represents the relative head displacement, and bottom plot represents the frame motion.

Reviewing the experimental data the LVDT shows that there is no relative motion across the head suspension at frequencies below 6 Hz, and below 4 Hz the frame moves in direct correspondence to the displacement input of the head structure. Between 4 Hz and 6 Hz no head suspension separation occurs, while amplitude growth of the frame response is apparent as shown by the DCDT measurement. These data are indicative of the head structure in flexure.

At and above 6 Hz, the force developed across the head suspension exceeds the 260 N clamping force and subsequently head suspension breakaway occurs as measured by the head LVDT. A significant change in the response amplitude of both the frame motion measurement and relative head displacement measurement is evident, while the phase lag of the frame response increases. Bouncing behavior is prevalent as the head and frame

re-establish contact. Initial impact is so extensive that a small amount of penetration occurs. Structural elasticity causes a temporary separation and then once again a large break-away occurs. Impact location is seen in the periodic input time history curve. The input displacement sinusoid at the 6 Hz frequency is distorted substantially. Figures 3.23 and 3.24, display the frequency content of the input displacement, at 5 Hz and 6 Hz respectively. The 6 Hz input has much harmonic distortion at amplitudes of 20 db while the 5 Hz input has harmonic distortion at amplitudes of 40 db below the fundamental.

Input frequencies in the neighborhood above 6 Hz (i.e. 7, 8, and 9 Hz) yield smaller relative head and frame amplitude response, while near 6 Hz a system resonance is present.

At 10 Hz, the data of Figure 3.17 show a large response at every second cycle of input and the system responds predominantly at 5 Hz, a subharmonic, rather than at the 10 Hz input. Figures 3.25 and 3.26 show the frequency content of the ram input and frame output at 9 and 10 Hz. As indicated in Figure 3.26, although the dominant input frequency is at 10 Hz the greatest frame response is at 5 Hz, a subharmonic. At 9 Hz, the data in Figure 3.25 indicate no subharmonic response, while the largest frame response is at the input frequency of 9 Hz.

The 11 Hz input is marked with distortion, as there exists some amount of distortion in all inputs above 5 Hz. The 11 Hz system response is primarily subharmonic with a whole cycle of no relative head break-away, then subsequent large relative response in the next cycle.

The 12 Hz data of Figure 3.19 illustrates the largest response of any

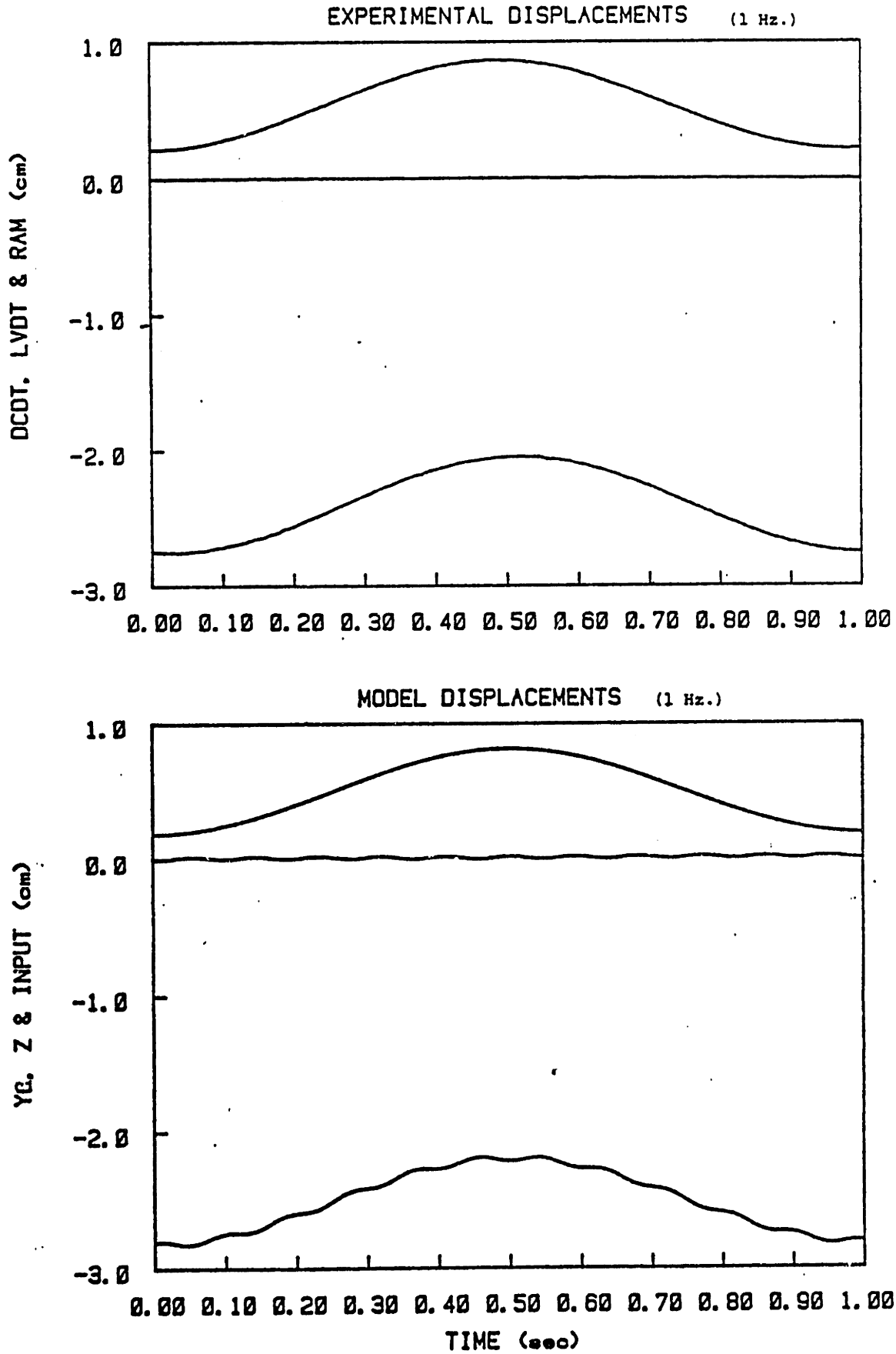
EXPERIMENTAL DISPLACEMENTS (1 Hz.)
DCDT, LVDT & RAM (cm)
1.0
0.0
-1.0
-2.0
-3.0
0.00 0.10 0.20 0.30 0.40 0.50 0.60 0.70 0.80 0.90 1.00
MODEL DISPLACEMENTS (1 Hz.)
YG, Z & INPUT (cm)
1.0
0.0
-1.0
-2.0
-3.0
0.00 0.10 0.20 0.30 0.40 0.50 0.60 0.70 0.80 0.90 1.00
TIME (sec)

FIGURE 3.8

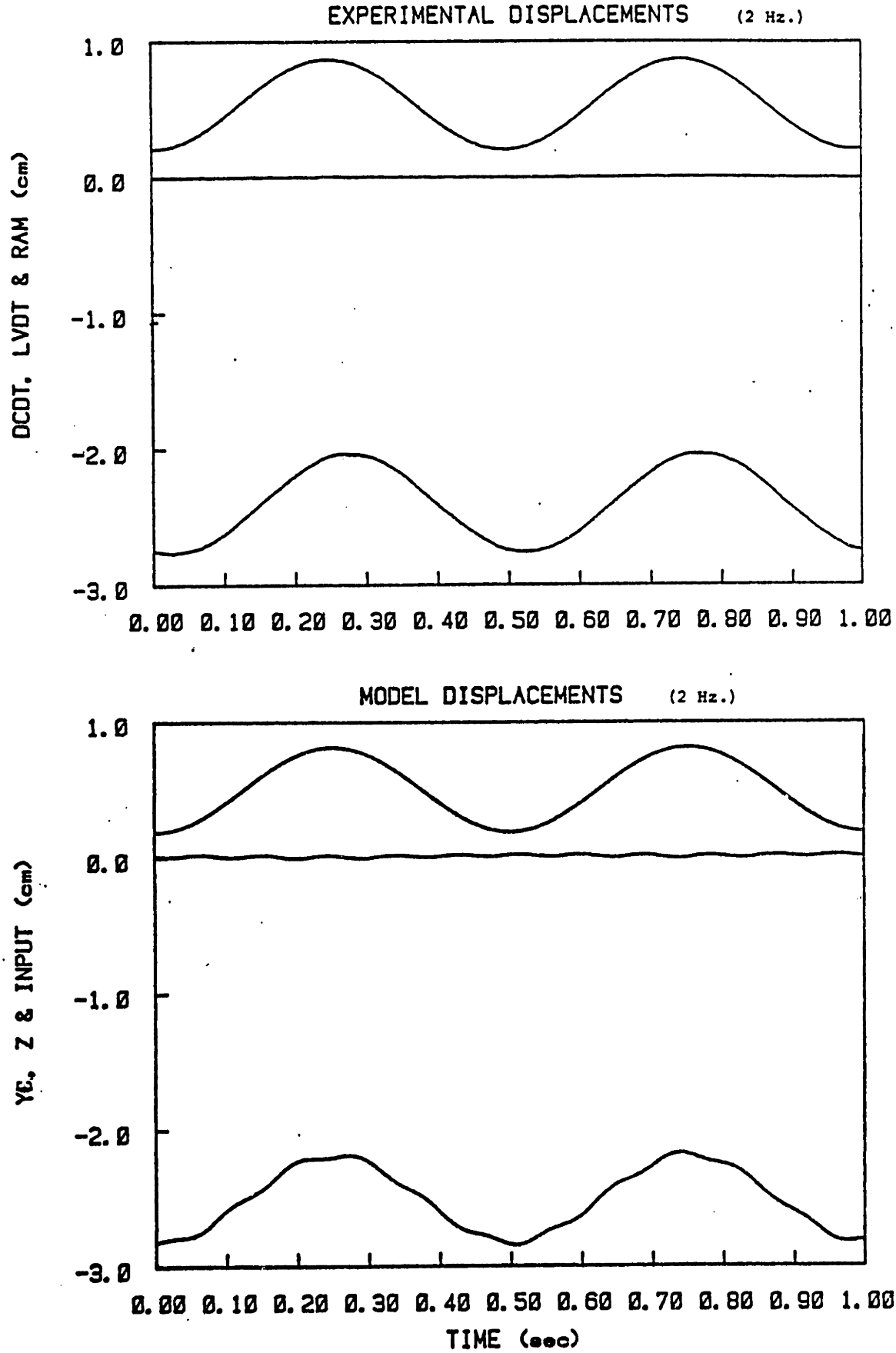
EXPERIMENTAL DISPLACEMENTS (2 Hz.)
DCDT, LVDT & RAM (cm)
1.0
0.0
-1.0
-2.0
-3.0
0.00 0.10 0.20 0.30 0.40 0.50 0.60 0.70 0.80 0.90 1.00
MODEL DISPLACEMENTS (2 Hz.)
YC, Z & INPUT (cm)
1.0
0.0
-1.0
-2.0
-3.0
0.00 0.10 0.20 0.30 0.40 0.50 0.60 0.70 0.80 0.90 1.00
TIME (sec)

FIGURE 3.9

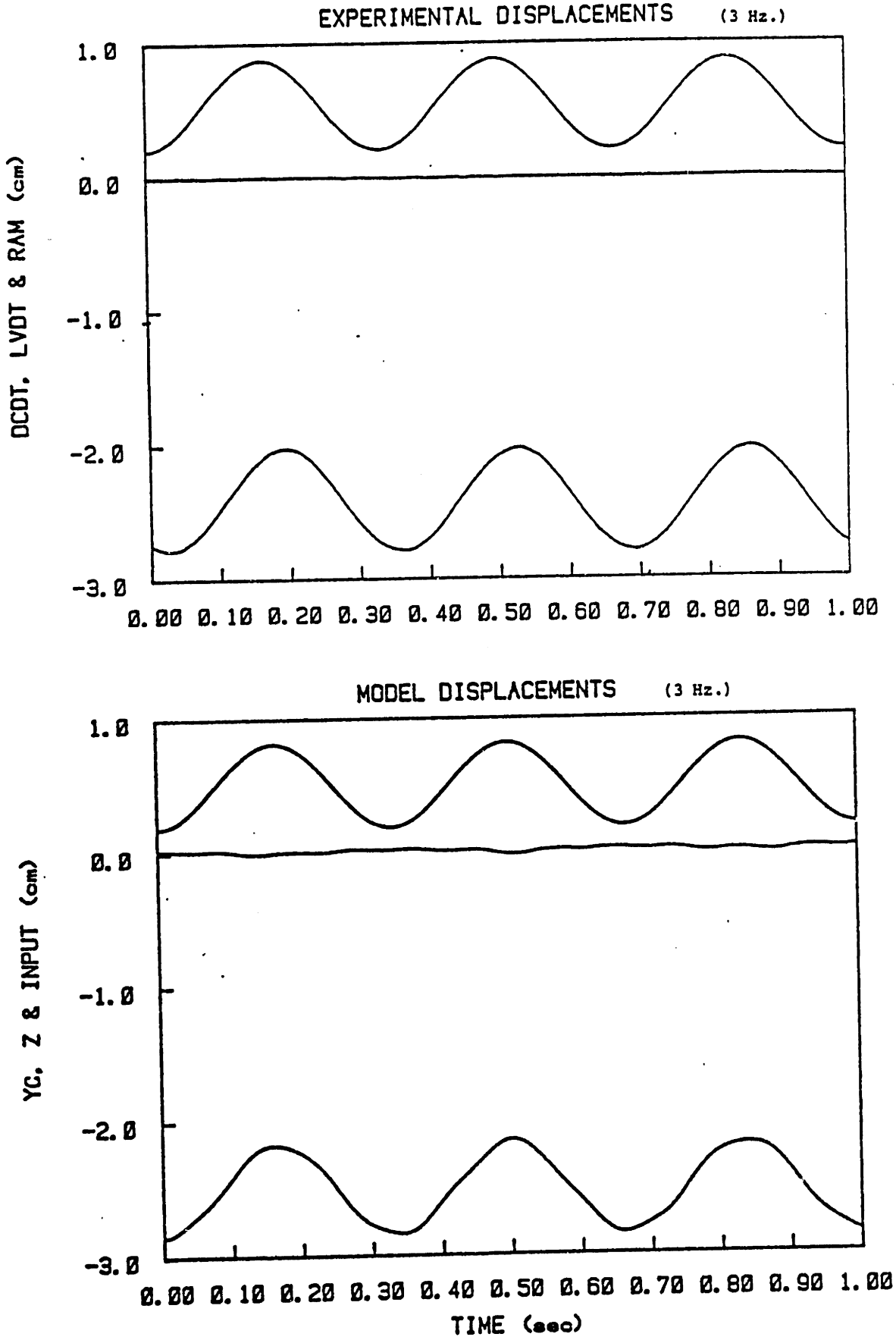
EXPERIMENTAL DISPLACEMENTS (3 Hz.)
DCDT, LVDT & RAM (cm)
1.0
0.0
-1.0
-2.0
-3.0
0.00 0.10 0.20 0.30 0.40 0.50 0.60 0.70 0.80 0.90 1.00
MODEL DISPLACEMENTS (3 Hz.)
YC, Z & INPUT (cm)
1.0
0.0
-1.0
-2.0
-3.0
0.00 0.10 0.20 0.30 0.40 0.50 0.60 0.70 0.80 0.90 1.00
TIME (sec)

FIGURE 3.10

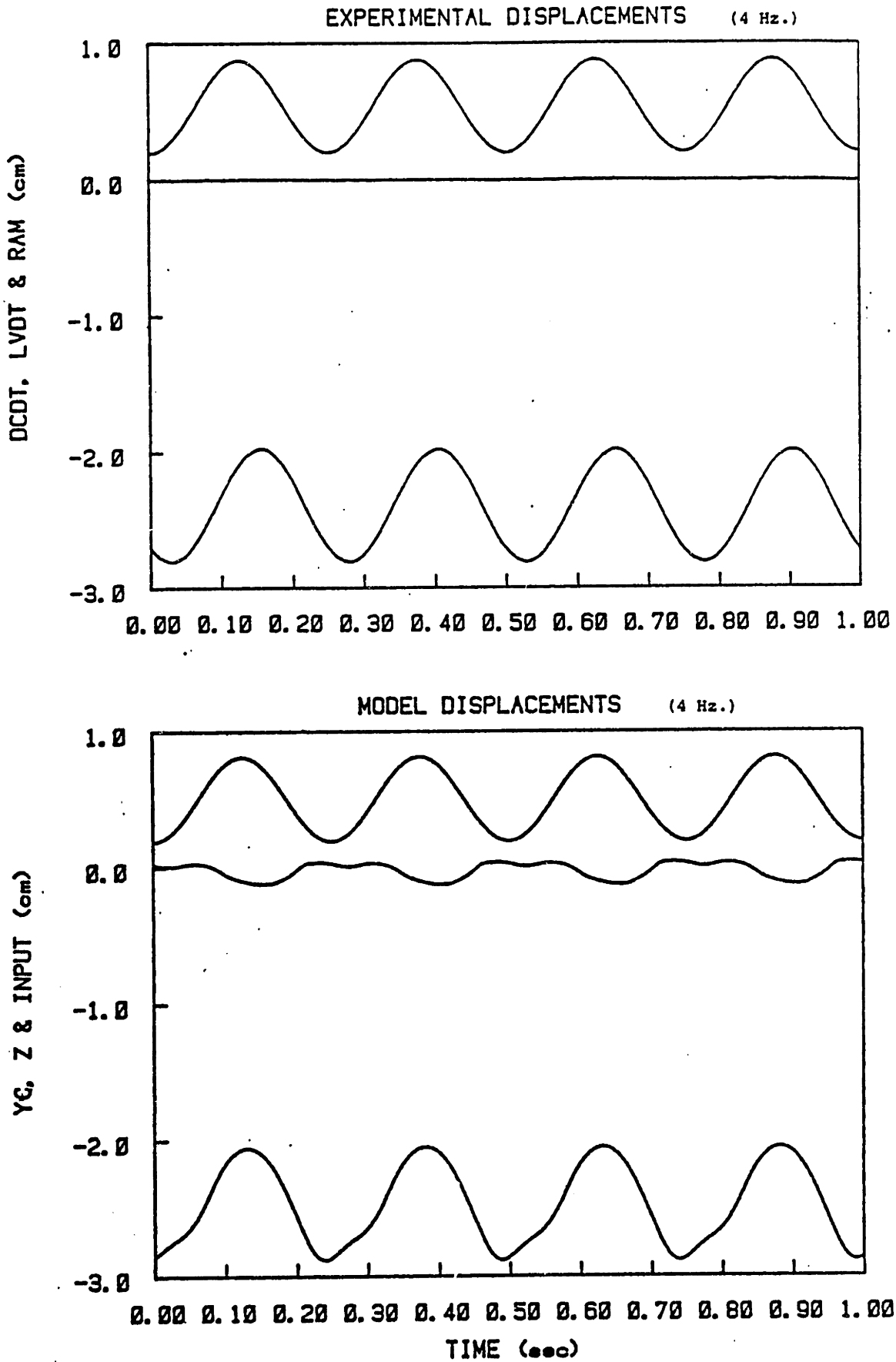
EXPERIMENTAL DISPLACEMENTS (4 Hz.)
DCDT, LVDT & RAM (cm)
1.0
0.0
-1.0
-2.0
-3.0
0.00 0.10 0.20 0.30 0.40 0.50 0.60 0.70 0.80 0.90 1.00
MODEL DISPLACEMENTS (4 Hz.)
YC, Z & INPUT (cm)
1.0
0.0
-1.0
-2.0
-3.0
0.00 0.10 0.20 0.30 0.40 0.50 0.60 0.70 0.80 0.90 1.00
TIME (sec)

FIGURE 3.11

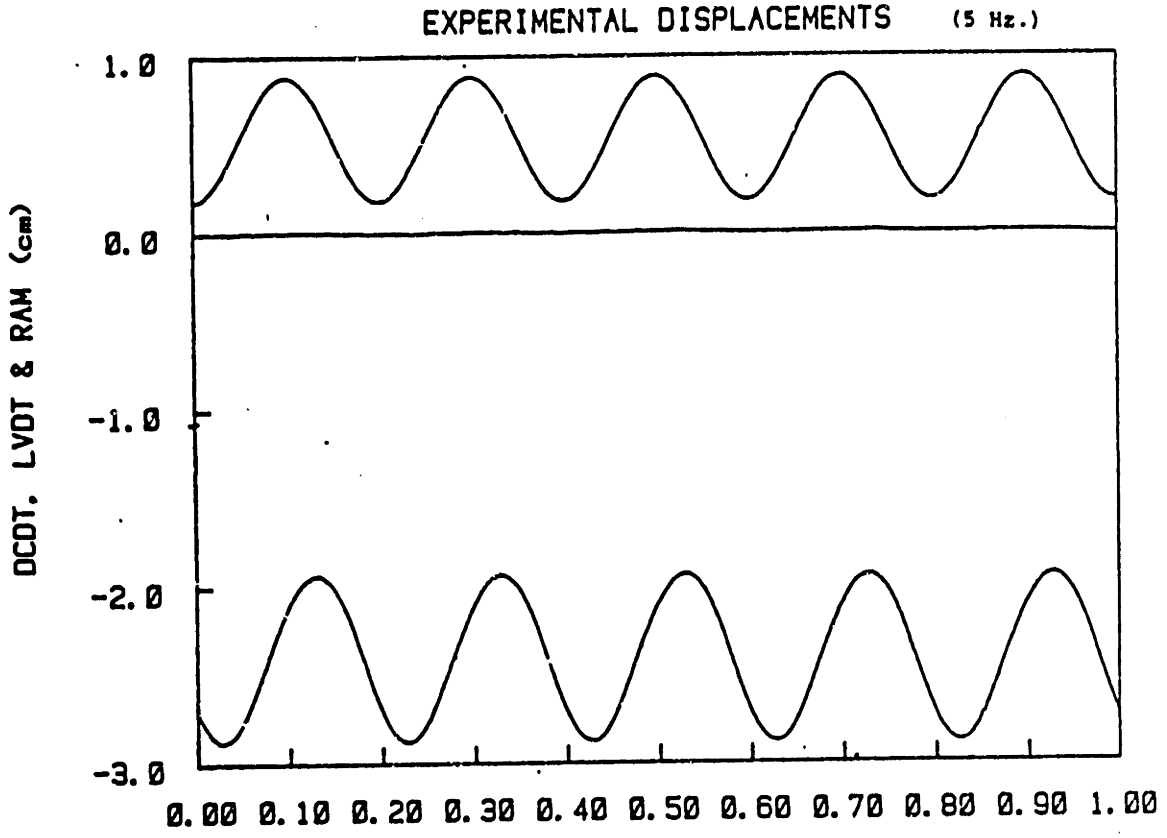
EXPERIMENTAL DISPLACEMENTS (5 Hz.)
DCDT, LVDT & RAM (cm)
1.0
0.0
-1.0
-2.0
-3.0
0.00 0.10 0.20 0.30 0.40 0.50 0.60 0.70 0.80 0.90 1.00

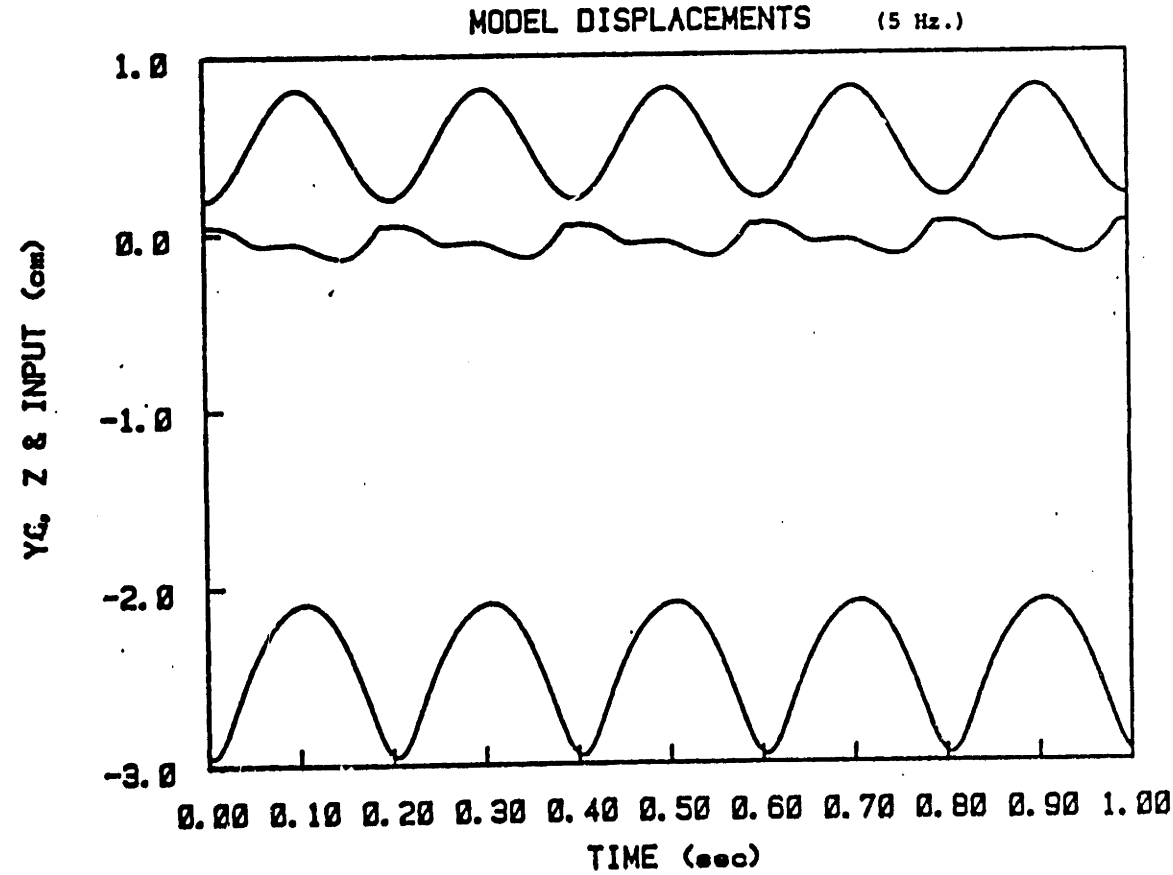
MODEL DISPLACEMENTS (5 Hz.)
YG, Z & INPUT (cm)
1.0
0.0
-1.0
-2.0
-3.0
0.00 0.10 0.20 0.30 0.40 0.50 0.60 0.70 0.80 0.90 1.00
TIME (sec)

FIGURE 3.12

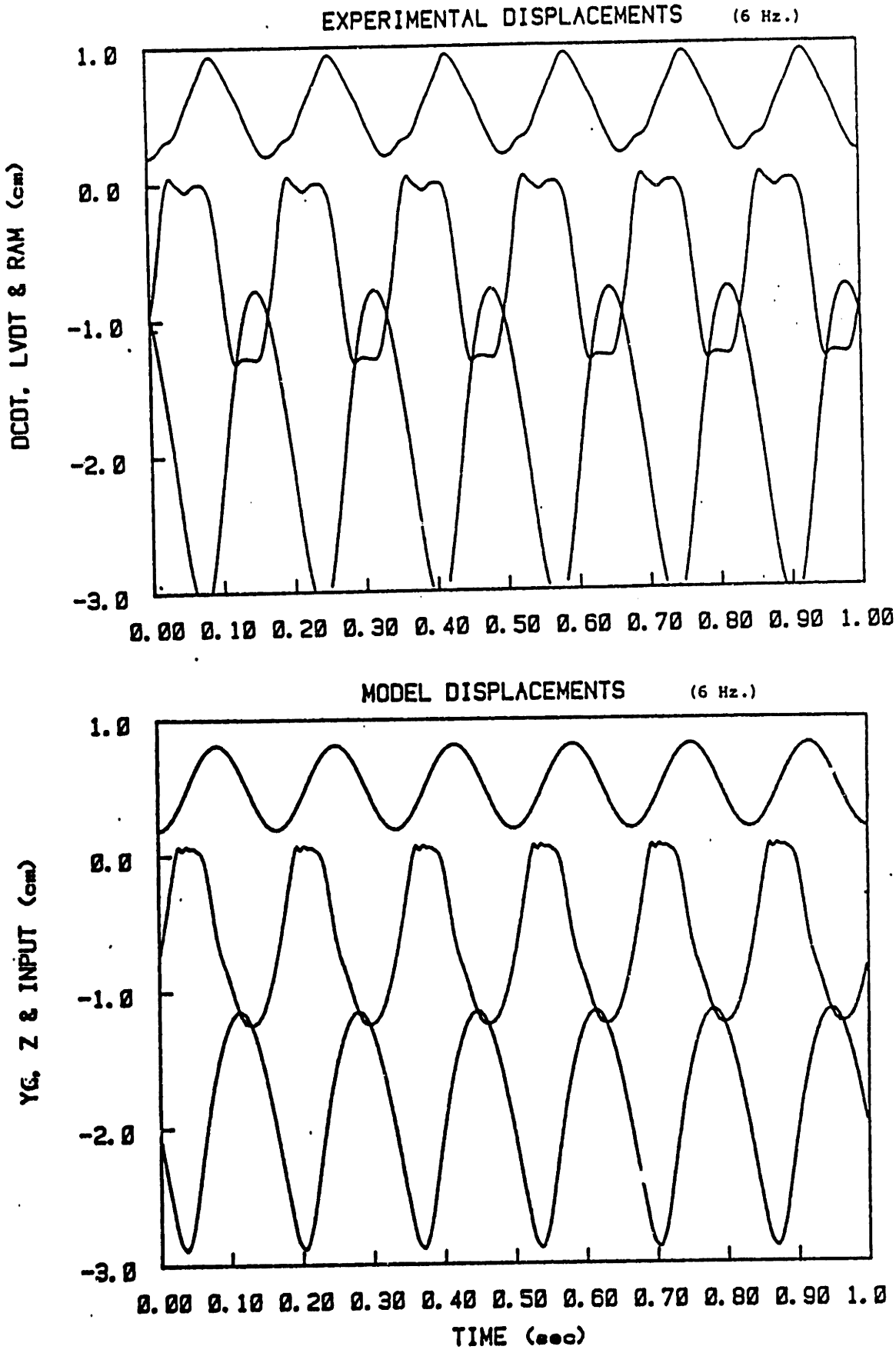
EXPERIMENTAL DISPLACEMENTS (6 Hz.)
DCDT, LVDT & RAM (cm)
1.0
0.0
-1.0
-2.0
-3.0
0.00 0.10 0.20 0.30 0.40 0.50 0.60 0.70 0.80 0.90 1.00
MODEL DISPLACEMENTS (6 Hz.)
YG, Z & INPUT (cm)
1.0
0.0
-1.0
-2.0
-3.0
0.00 0.10 0.20 0.30 0.40 0.50 0.60 0.70 0.80 0.90 1.0
TIME (sec)

FIGURE 3.13

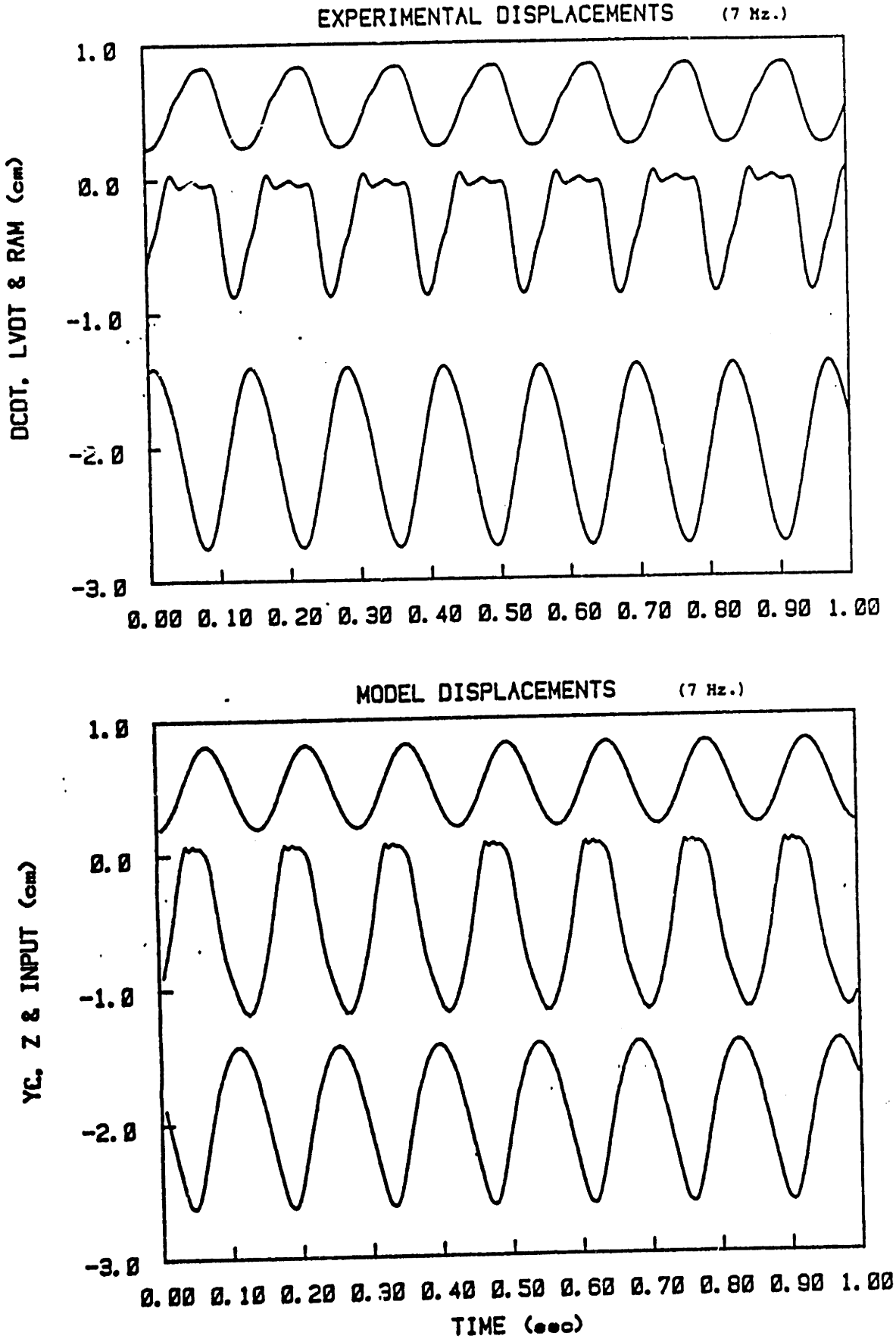
EXPERIMENTAL DISPLACEMENTS (7 Hz.)
DCDT, LVDT & RAM (cm)
1.0
0.0
-1.0
-2.0
-3.0
0.00 0.10 0.20 0.30 0.40 0.50 0.60 0.70 0.80 0.90 1.00
MODEL DISPLACEMENTS (7 Hz.)
YC, Z & INPUT (cm)
1.0
0.0
-1.0
-2.0
-3.0
0.00 0.10 0.20 0.30 0.40 0.50 0.60 0.70 0.80 0.90 1.00
TIME (sec)

FIGURE 3.14

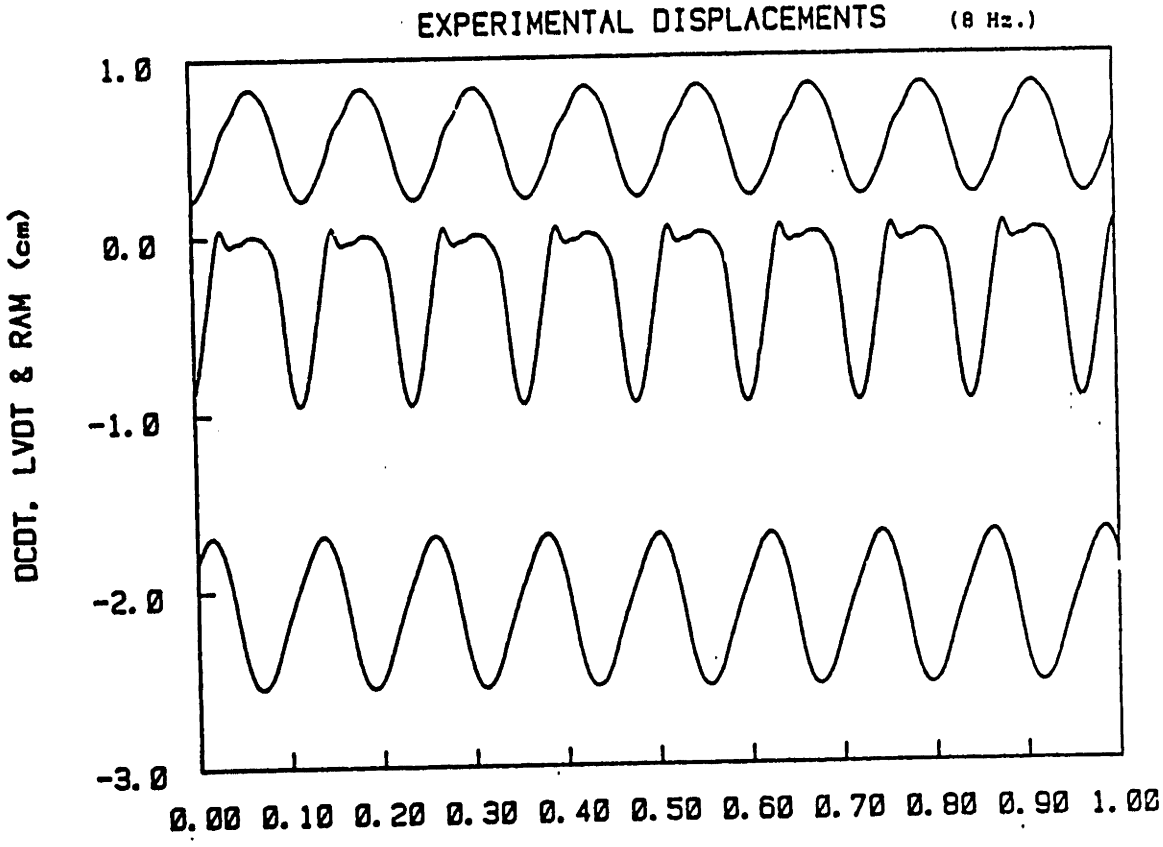
EXPERIMENTAL DISPLACEMENTS (8 Hz.)
DCDT, LVDT & RAM (cm)
1.0
0.0
-1.0
-2.0
-3.0
0.00 0.10 0.20 0.30 0.40 0.50 0.60 0.70 0.80 0.90 1.00

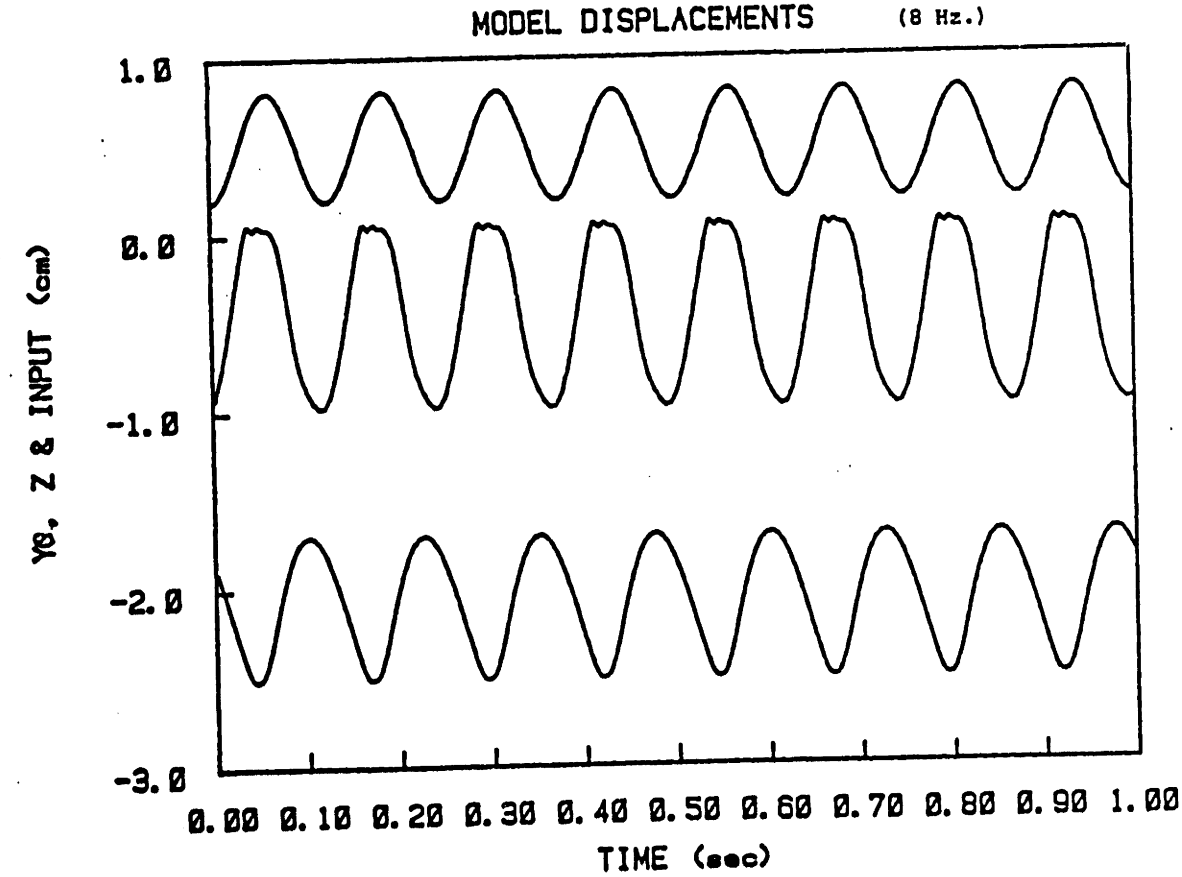
MODEL DISPLACEMENTS (8 Hz.)
Y0, Z & INPUT (cm)
1.0
0.0
-1.0
-2.0
-3.0
0.00 0.10 0.20 0.30 0.40 0.50 0.60 0.70 0.80 0.90 1.00
TIME (sec)

FIGURE 3.15

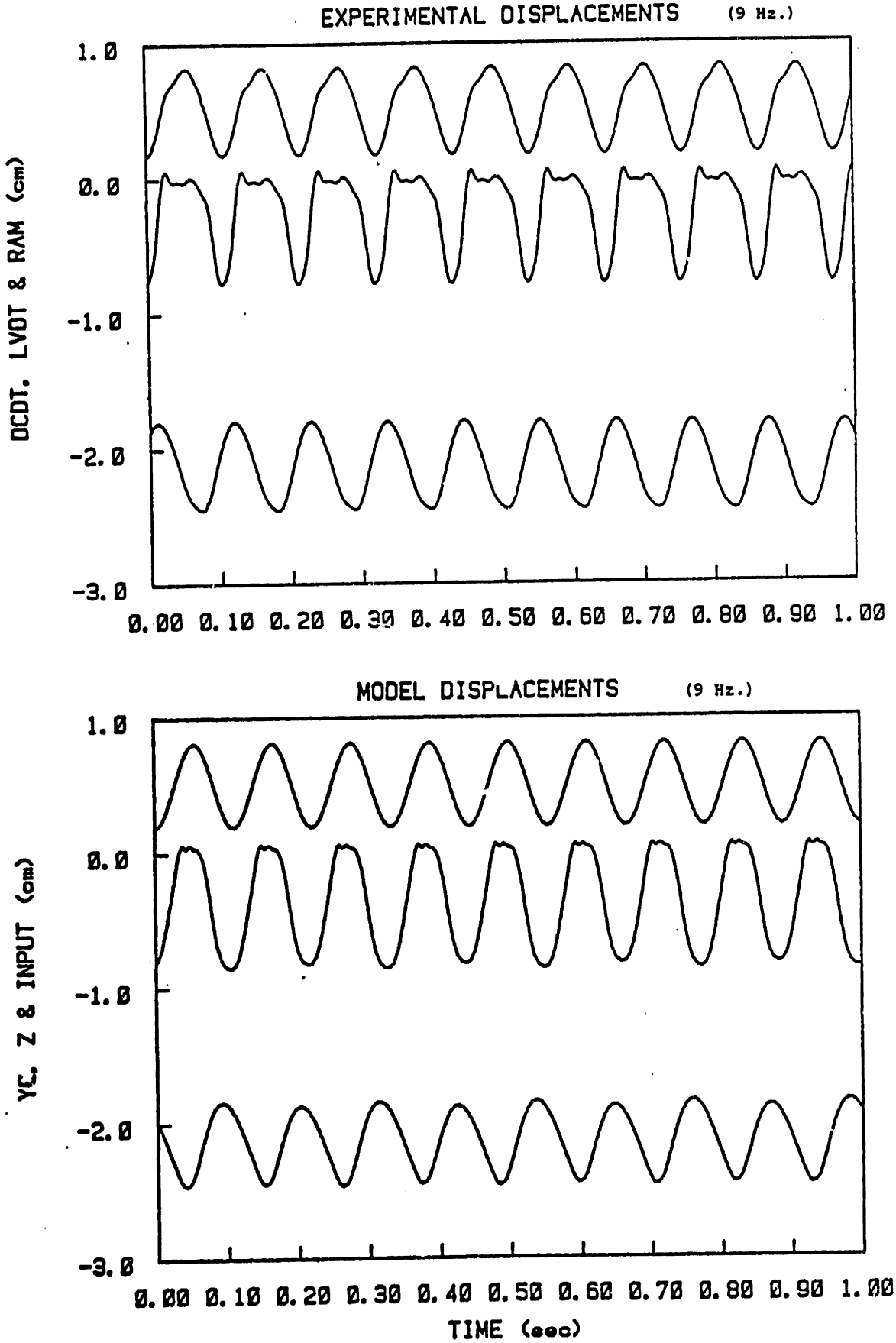
EXPERIMENTAL DISPLACEMENTS (9 Hz.)
DCDT, LVDT & RAM (cm)
1.0
0.0
-1.0
-2.0
-3.0
0.00 0.10 0.20 0.30 0.40 0.50 0.60 0.70 0.80 0.90 1.00
MODEL DISPLACEMENTS (9 Hz.)
YC, Z & INPUT (cm)
1.0
0.0
-1.0
-2.0
-3.0
0.00 0.10 0.20 0.30 0.40 0.50 0.60 0.70 0.80 0.90 1.00
TIME (sec)

FIGURE 3.16

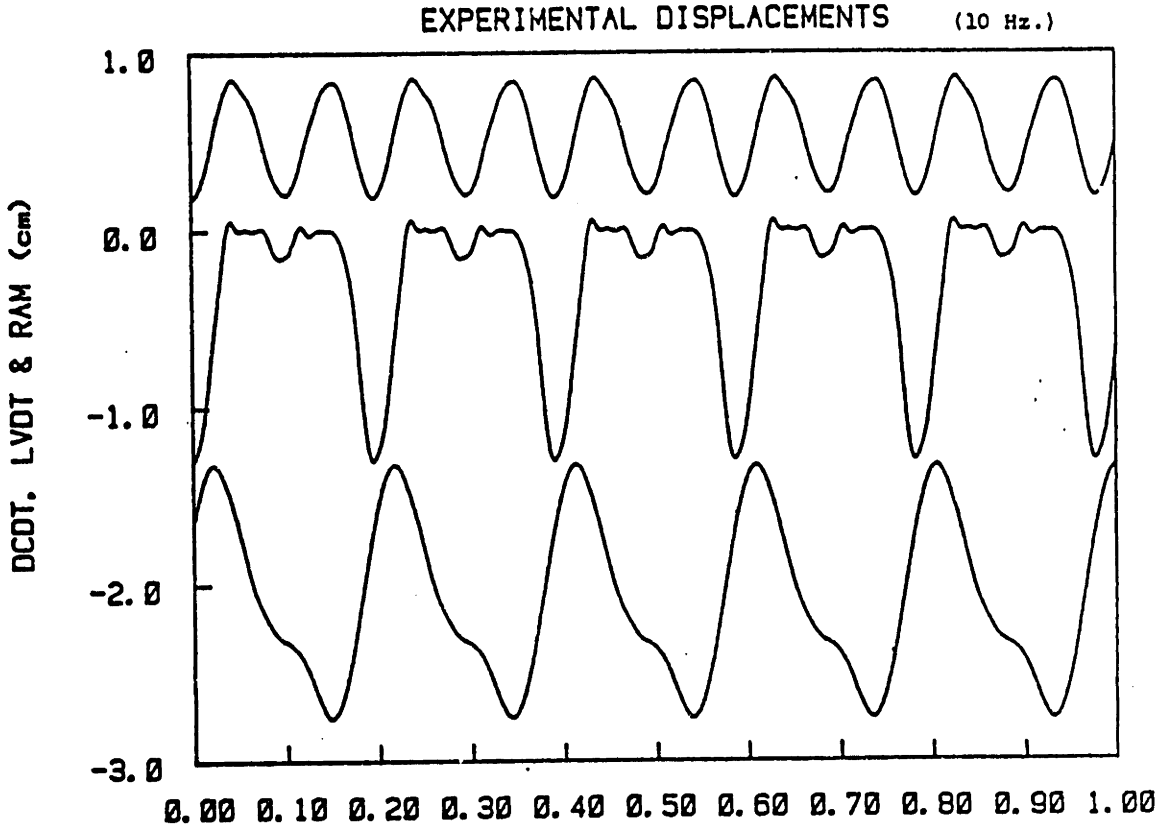
EXPERIMENTAL DISPLACEMENTS (10 Hz.)
DCDT, LVDT & RAM (cm)
1.0
0.0
-1.0
-2.0
-3.0
0.00 0.10 0.20 0.30 0.40 0.50 0.60 0.70 0.80 0.90 1.00

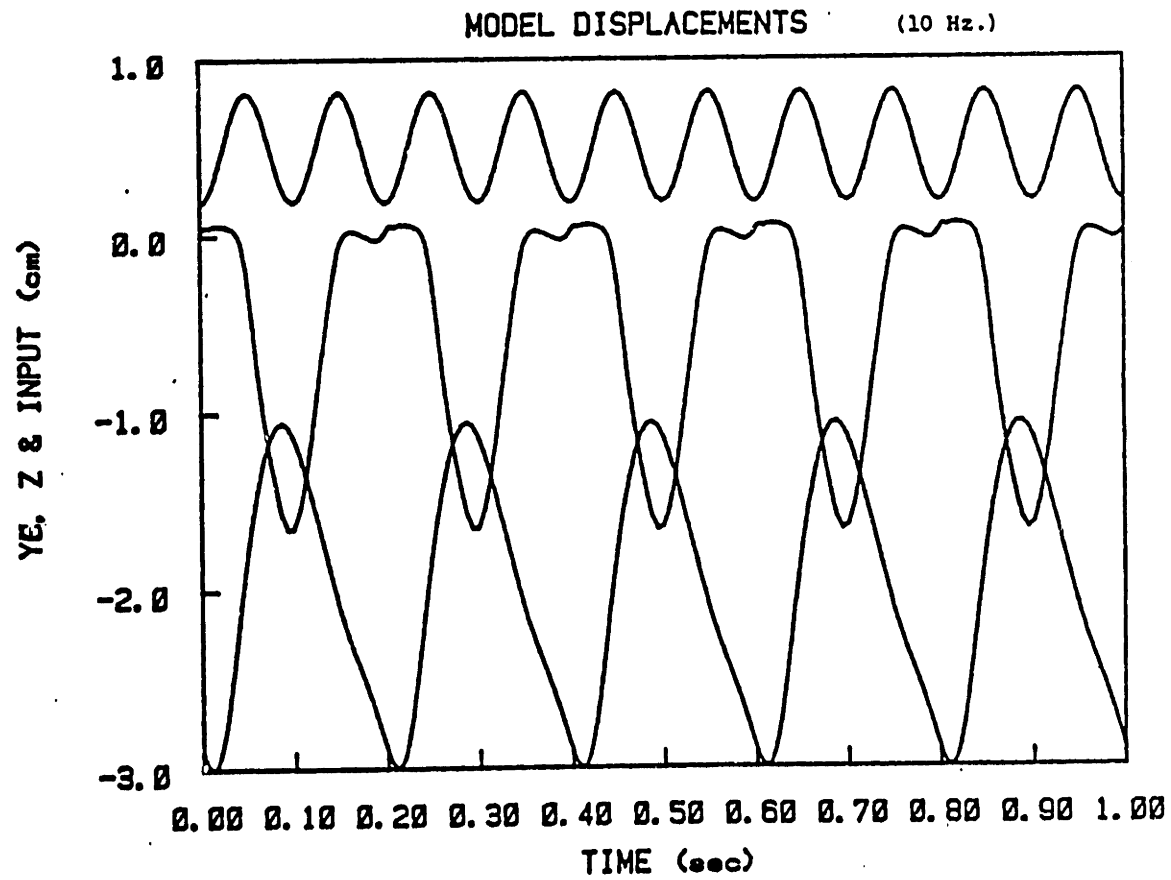
MODEL DISPLACEMENTS (10 Hz.)
YE, Z & INPUT (cm)
1.0
0.0
-1.0
-2.0
-3.0
0.00 0.10 0.20 0.30 0.40 0.50 0.60 0.70 0.80 0.90 1.00
TIME (sec)

FIGURE 3.17

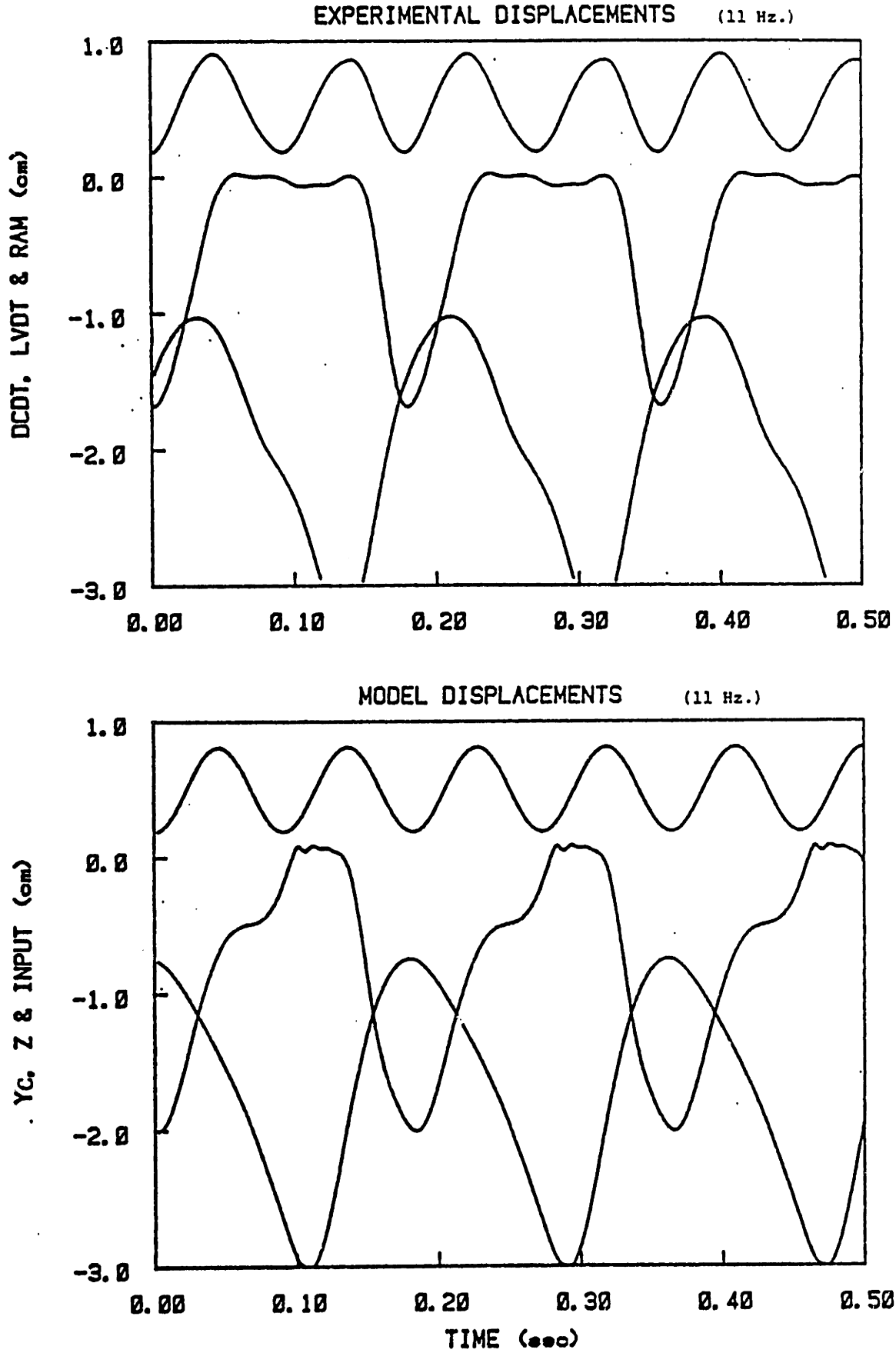
EXPERIMENTAL DISPLACEMENTS (11 Hz.)
DCDT, LVDT & RAM (cm)
1.0
0.0
-1.0
-2.0
-3.0
0.00
0.10
0.20
0.30
0.40
0.50
MODEL DISPLACEMENTS (11 Hz.)
Yc, Z & INPUT (cm)
1.0
0.0
-1.0
-2.0
-3.0
0.00
0.10
0.20
0.30
0.40
0.50
TIME (sec)

FIGURE 3.18

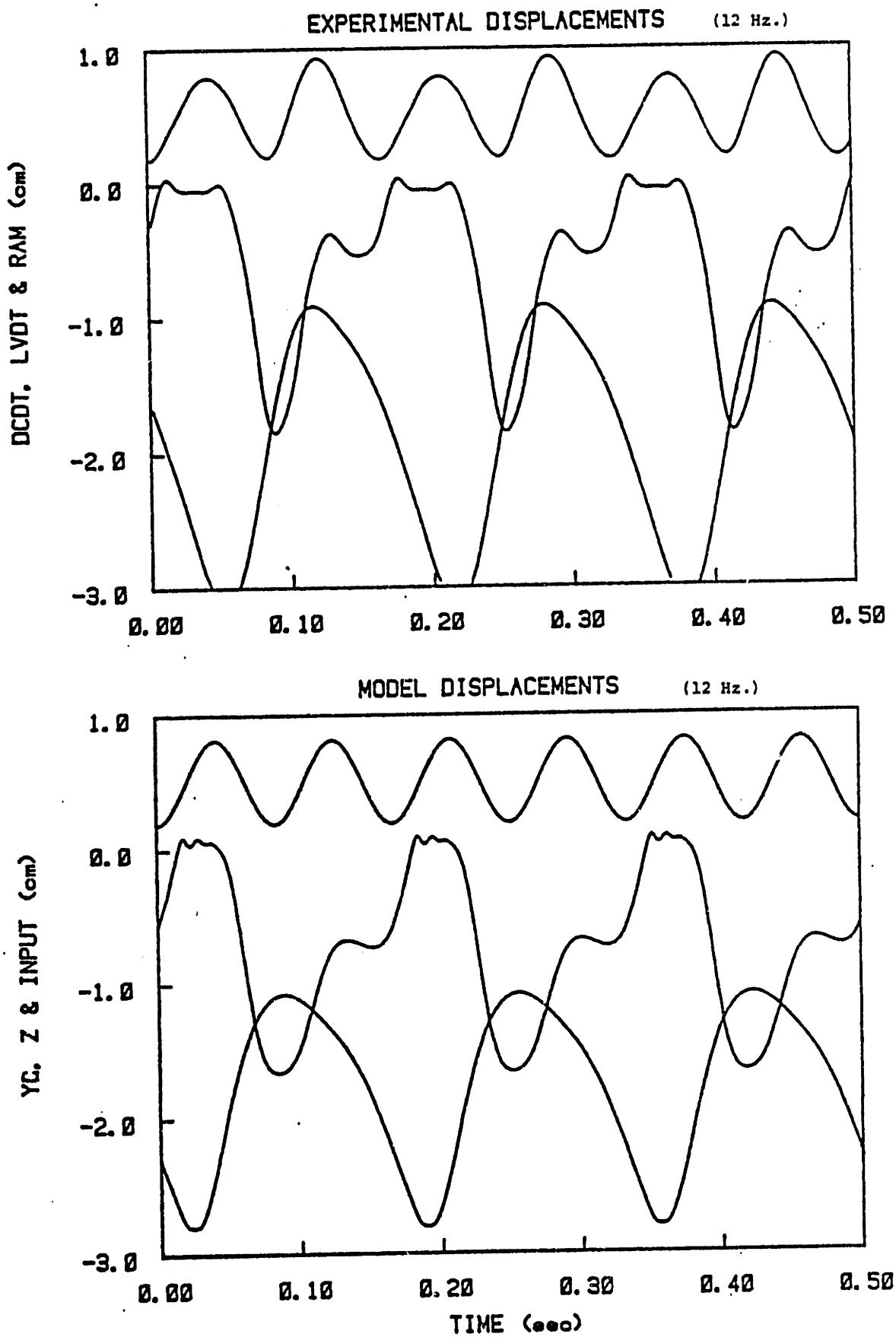
EXPERIMENTAL DISPLACEMENTS (12 Hz.)
DCDT, LVDT & RAM (cm)
1.0
0.0
-1.0
-2.0
-3.0
0.00
0.10
0.20
0.30
0.40
0.50
MODEL DISPLACEMENTS (12 Hz.)
YG, Z & INPUT (cm)
1.0
0.0
-1.0
-2.0
-3.0
0.00
0.10
0.20
0.30
0.40
0.50
TIME (sec)

FIGURE 3.19

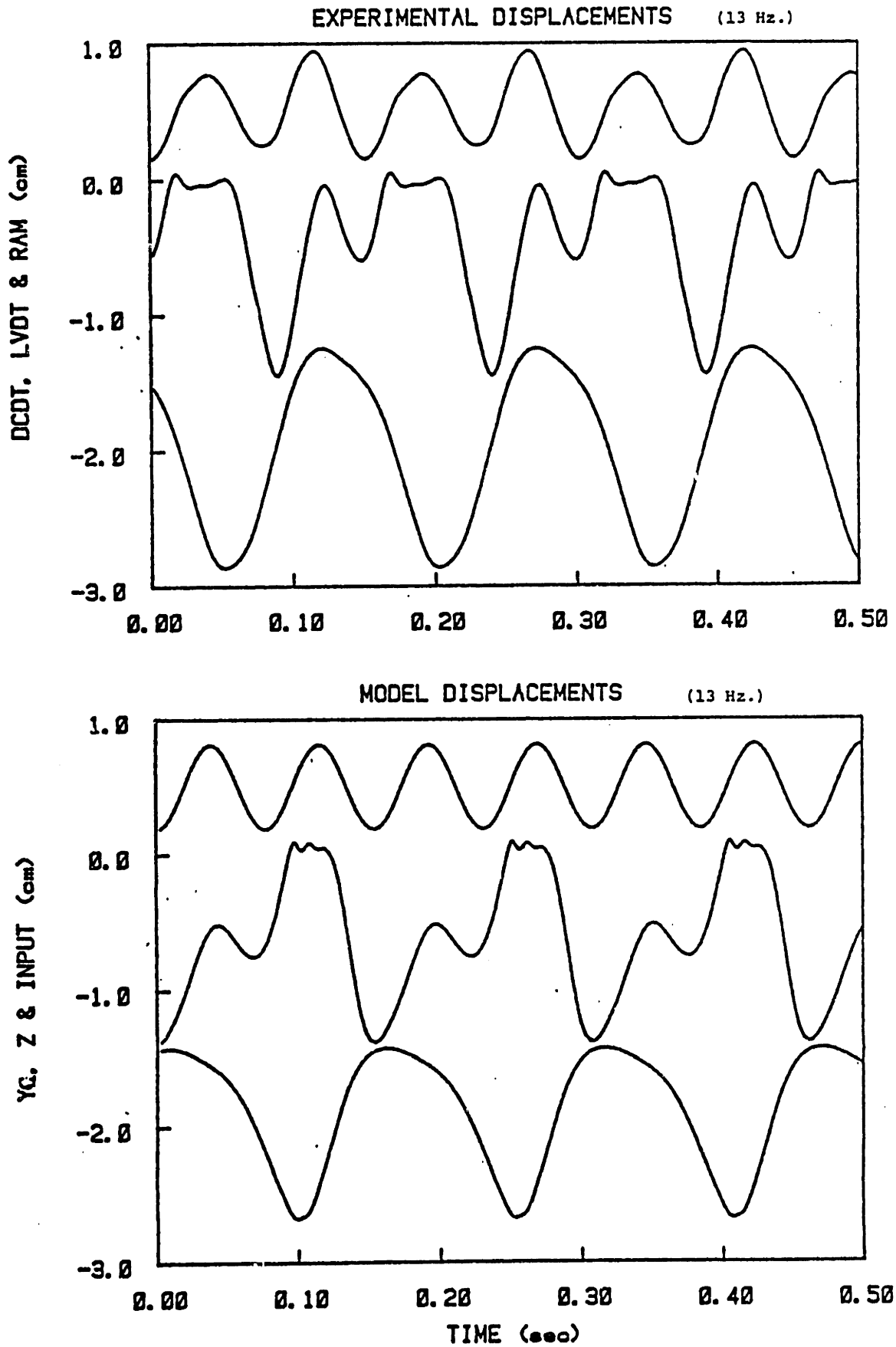
EXPERIMENTAL DISPLACEMENTS (13 Hz.)
DCDT, LVDT & RAM (cm)
1.0
0.0
-1.0
-2.0
-3.0
0.00
0.10
0.20
0.30
0.40
0.50
MODEL DISPLACEMENTS (13 Hz.)
YG, Z & INPUT (cm)
1.0
0.0
-1.0
-2.0
-3.0
0.00
0.10
0.20
0.30
0.40
0.50
TIME (sec)

FIGURE 3.20

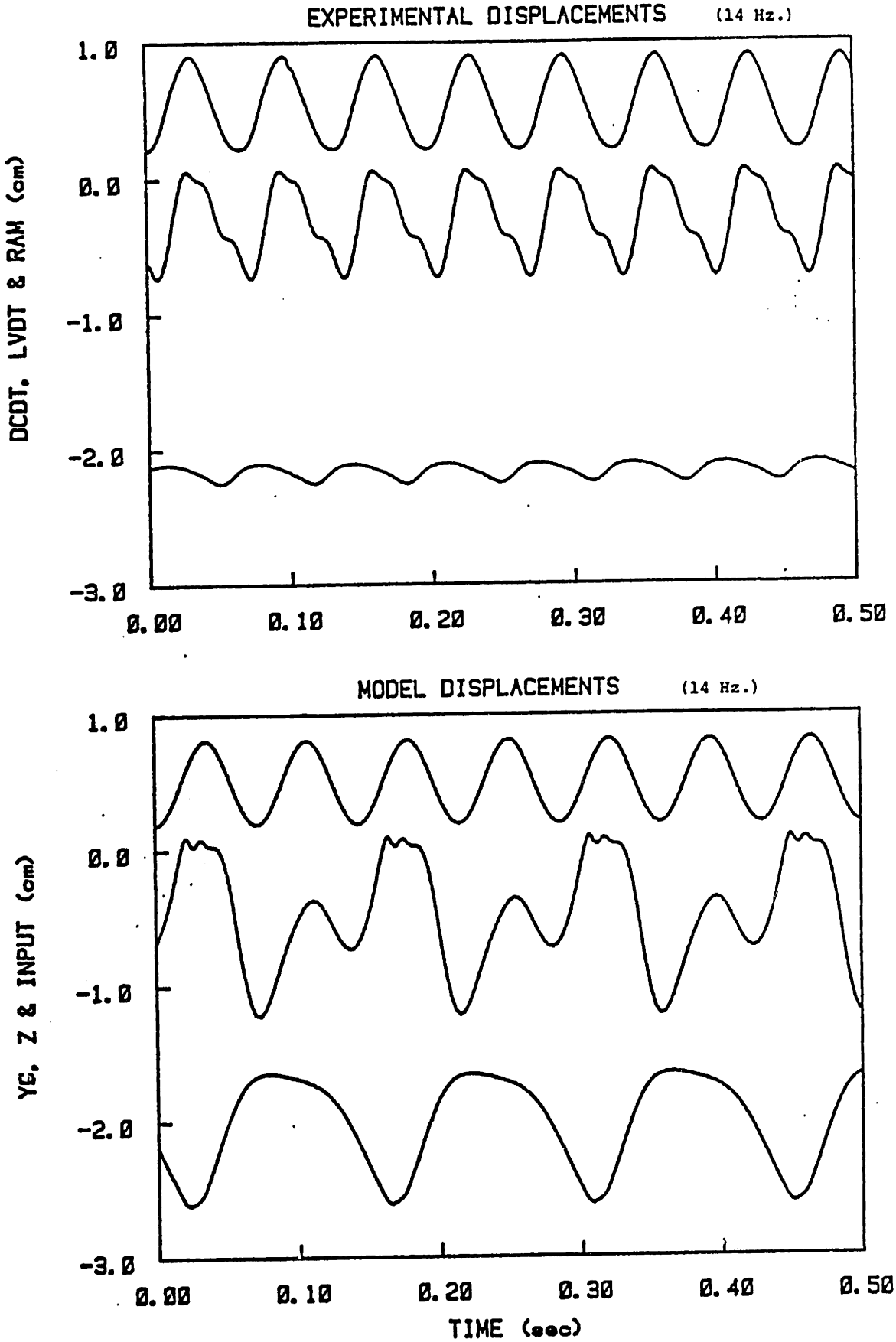
EXPERIMENTAL DISPLACEMENTS (14 Hz.)
DCDT, LVDT & RAM (cm)
1.0
0.0
-1.0
-2.0
-3.0
0.00
0.10
0.20
0.30
0.40
0.50
MODEL DISPLACEMENTS (14 Hz.)
YE, Z & INPUT (cm)
1.0
0.0
-1.0
-2.0
-3.0
0.00
0.10
0.20
0.30
0.40
0.50
TIME (sec)

FIGURE 3.21

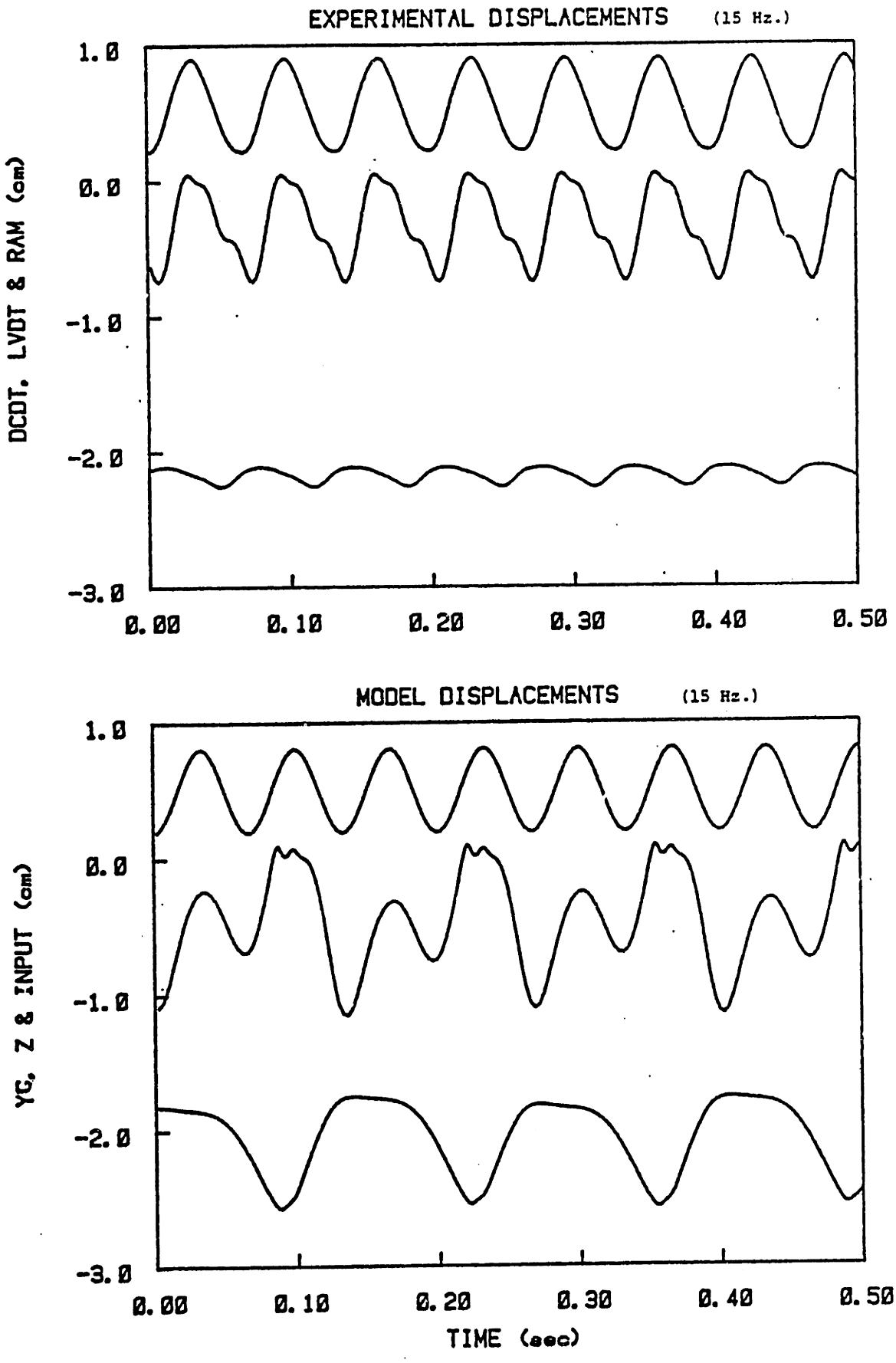
EXPERIMENTAL DISPLACEMENTS (15 Hz.)
DCDT, LVDT & RAM (cm)
1.0
0.0
-1.0
-2.0
-3.0
0.00
0.10
0.20
0.30
0.40
0.50
MODEL DISPLACEMENTS (15 Hz.)
YC, Z & INPUT (cm)
1.0
0.0
-1.0
-2.0
-3.0
0.00
0.10
0.20
0.30
0.40
0.50
TIME (sec)

FIGURE 3.22

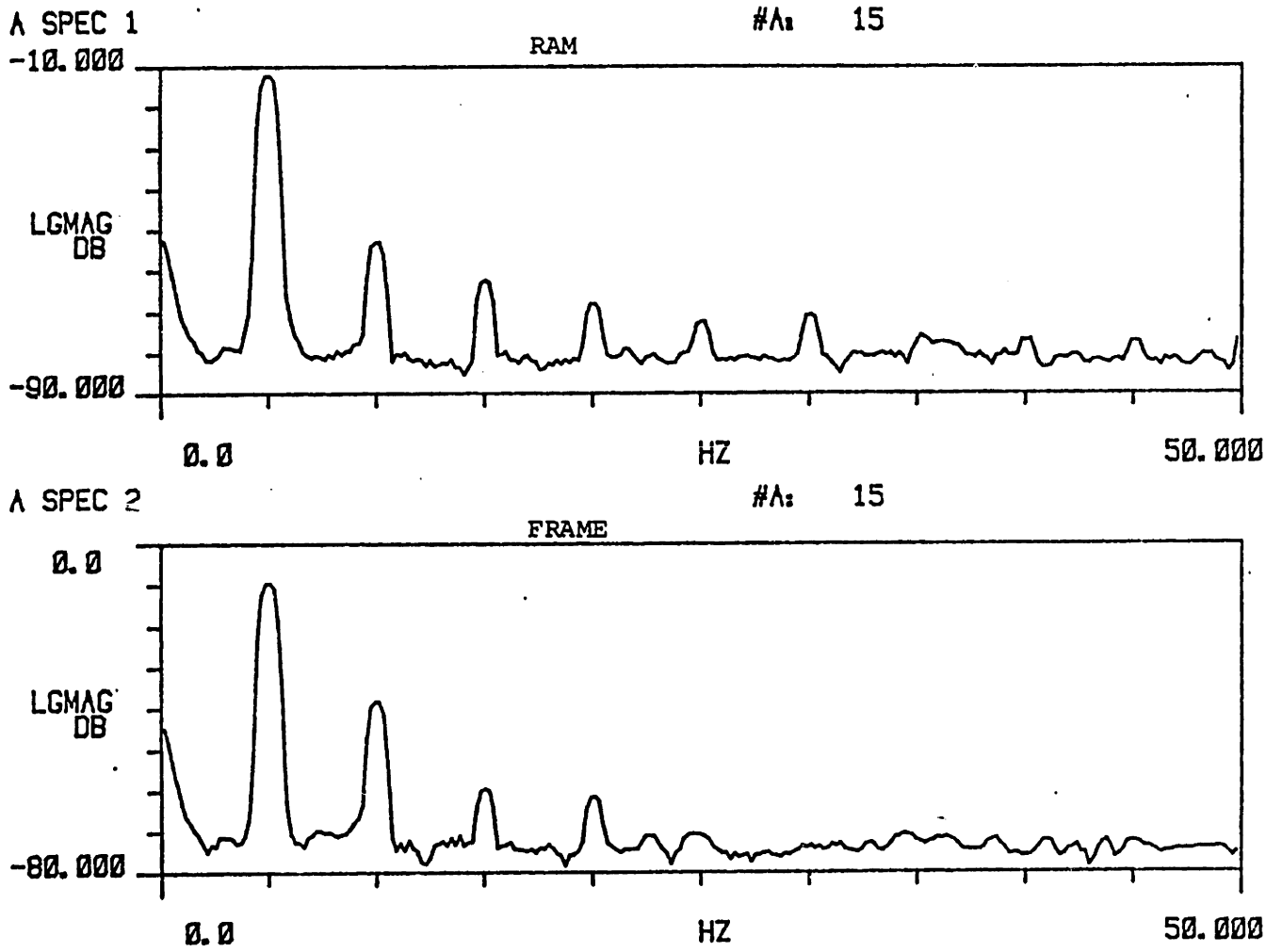

FIGURE 3.23: FREQUENCY CONTENT OF RAM AND FRAME AT 5 HZ

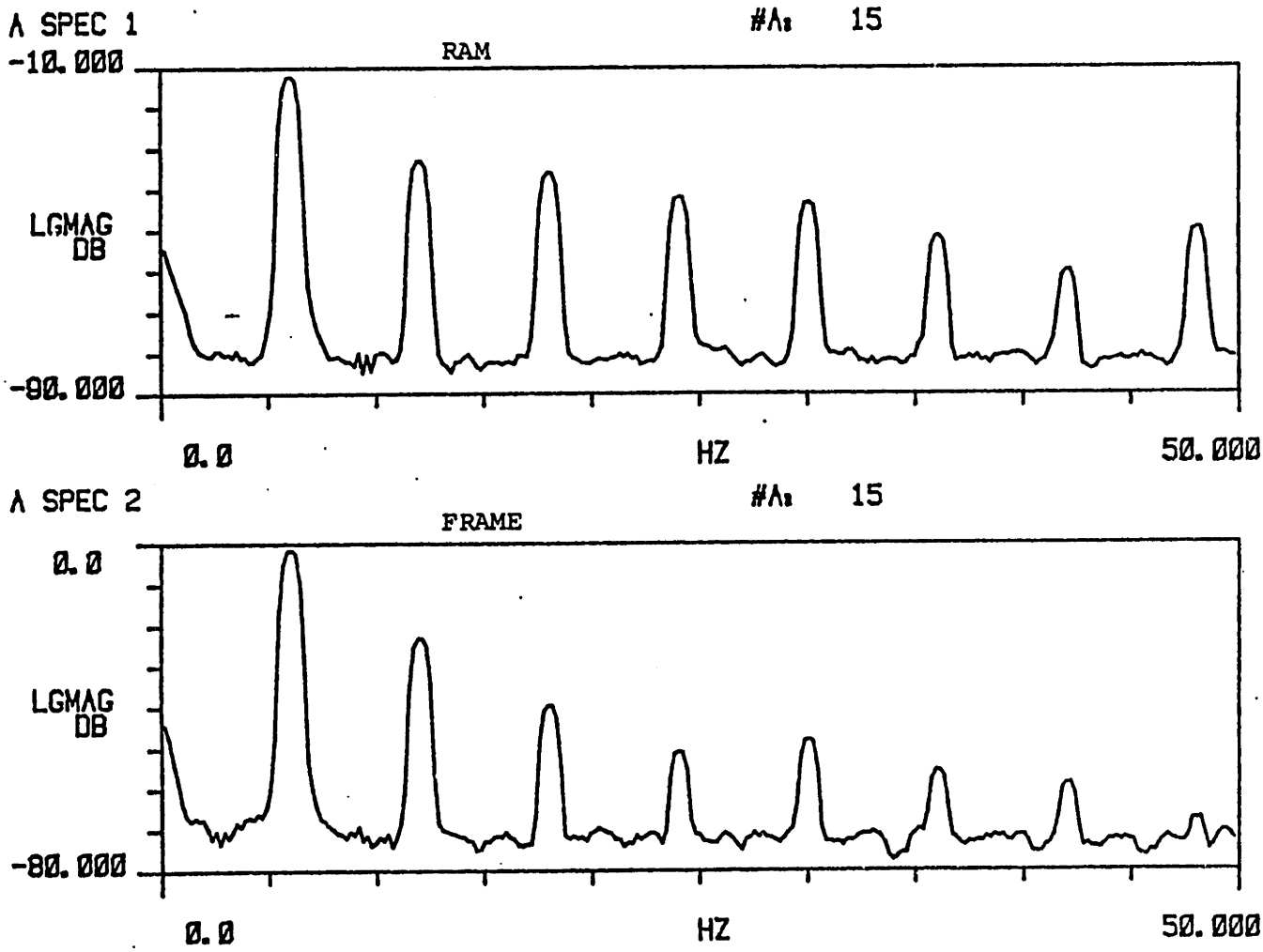

FIGURE 3.24: FREQUENCY CONTENT OF RAM AND FRAME AT 6 HZ

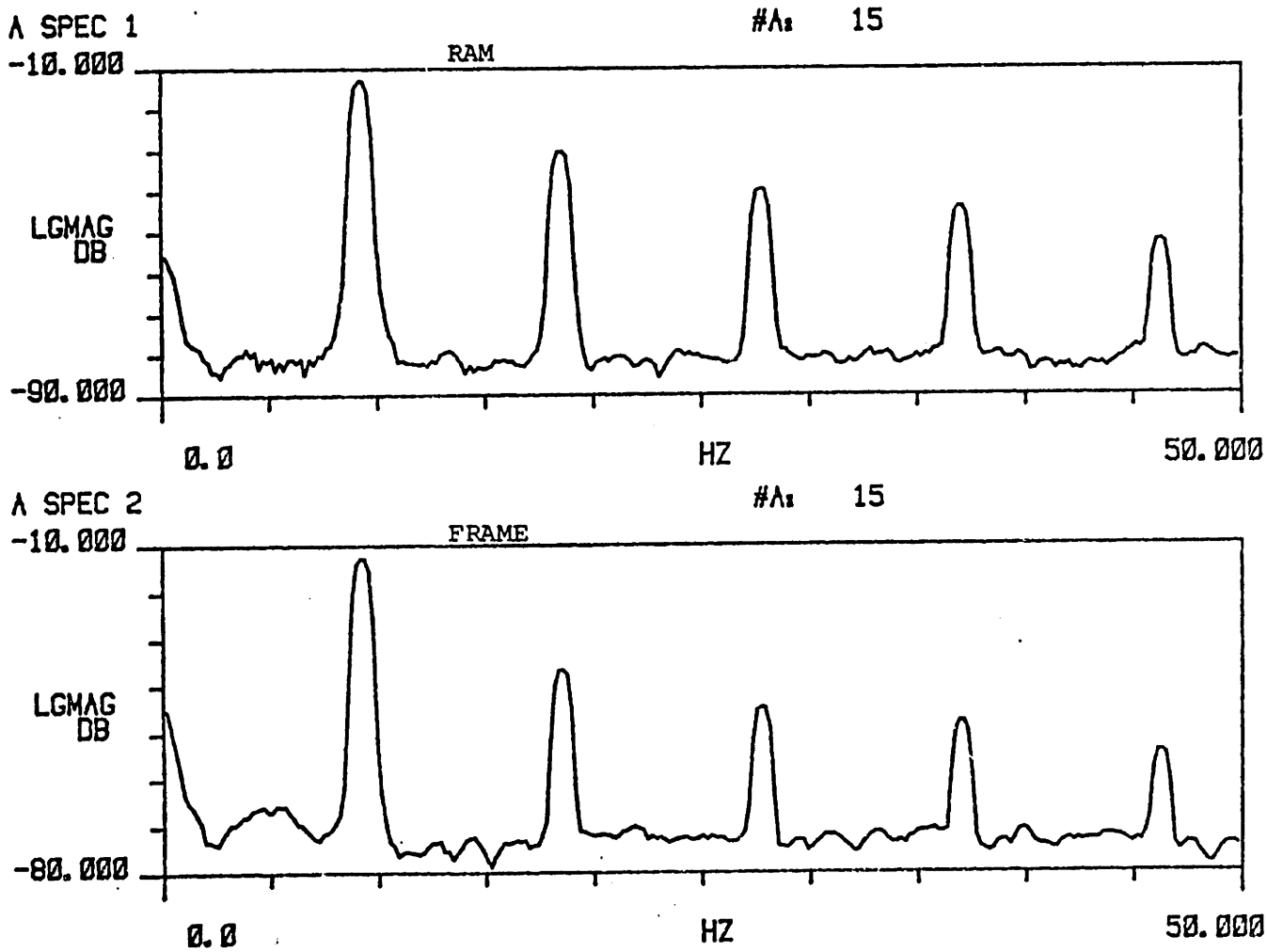

FIGURE 3.25: FREQUENCY CONTENT OF RAM AND FRAME AT 9 HZ

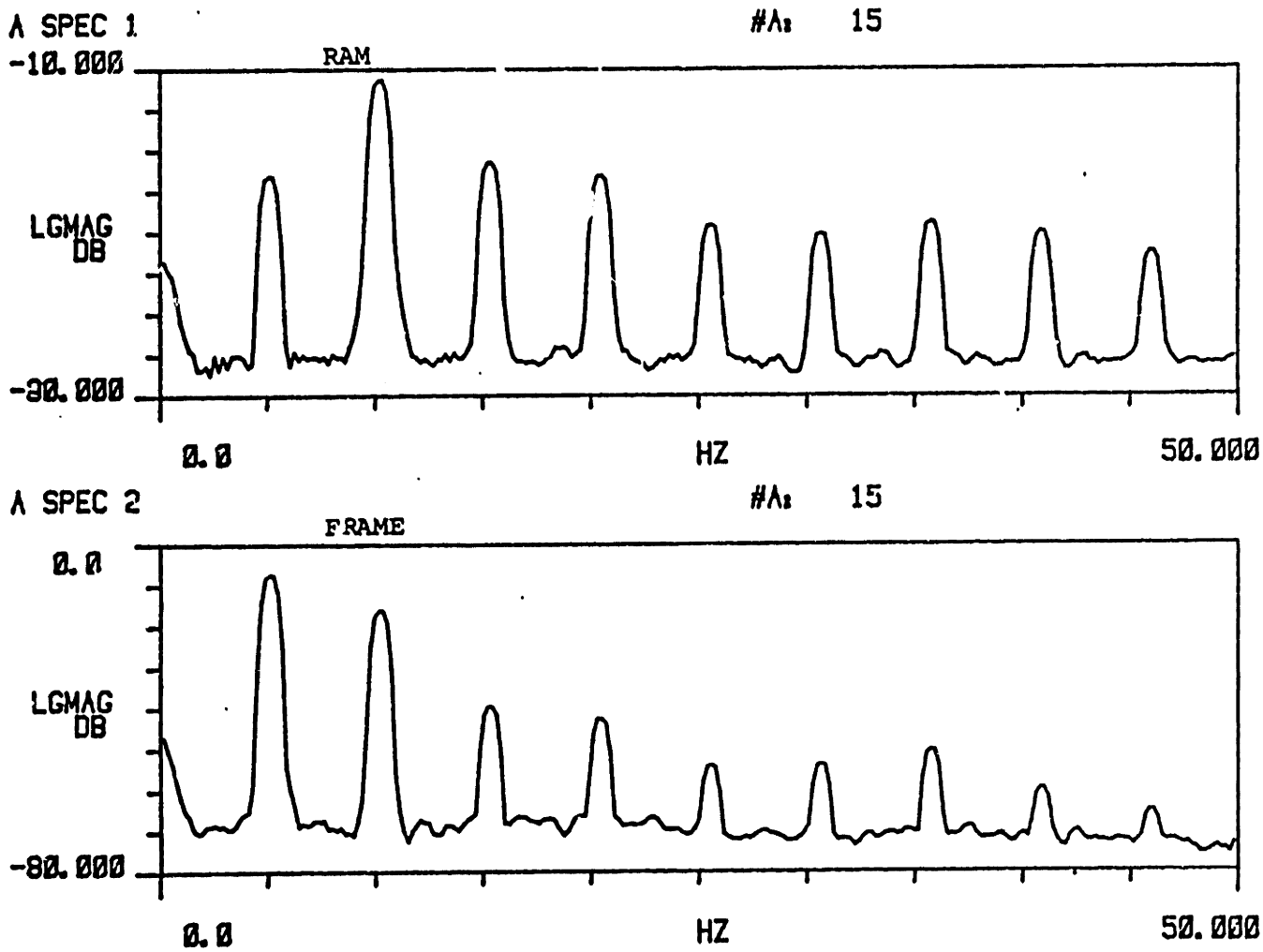

FIGURE 3.26: FREQUENCY CONTENT OF RAM AND FRAME AT 10 Hz

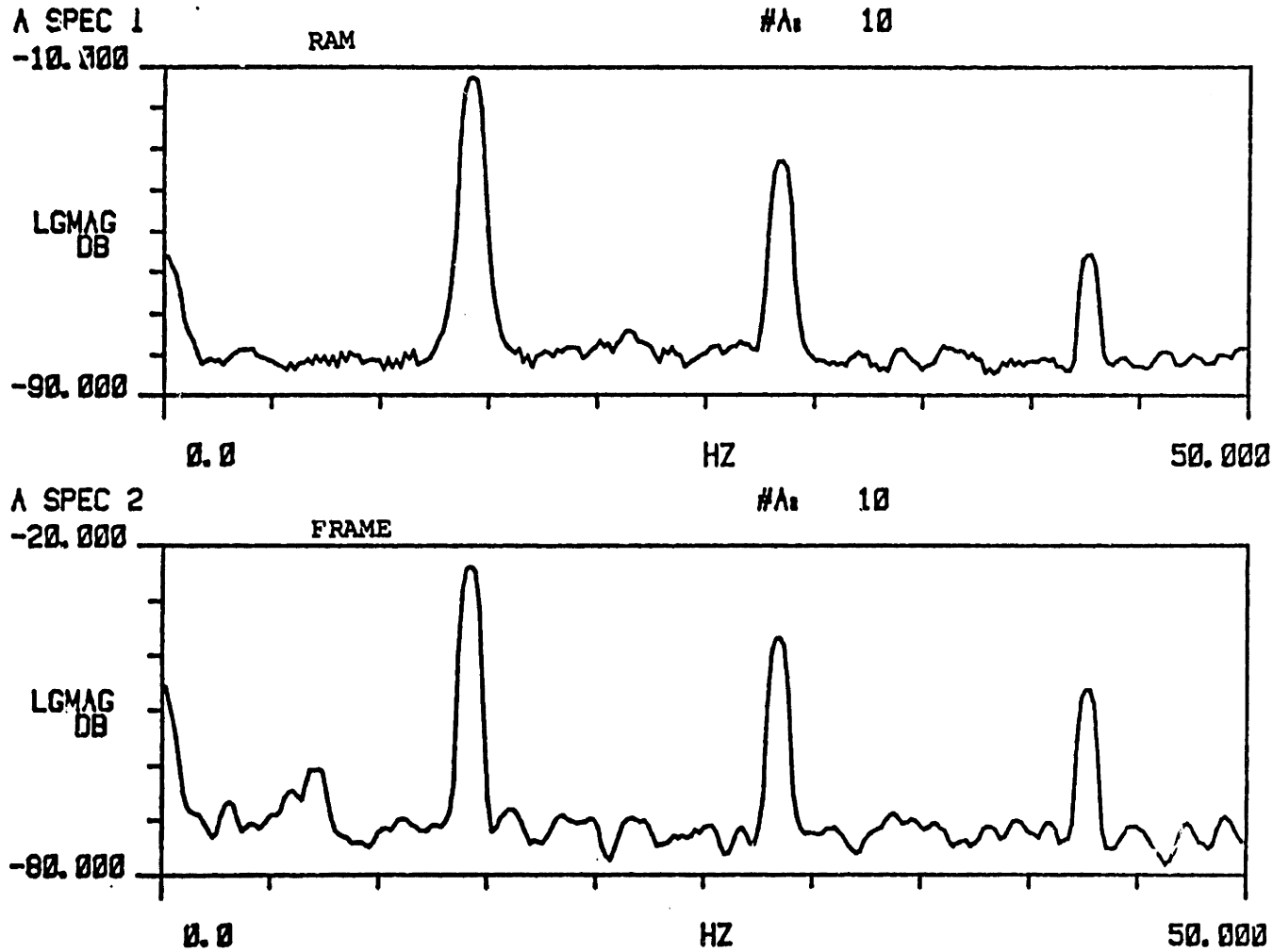

FIGURE 3.27: FREQUENCY CONTENT OF RAM AND FRAME AT 14 Hz

frequency input. This frequency is double the 6 Hz resonance frequency noted above.

At 13 Hz data in Figure 3.20 show that a subharmonic distortion of the input occurs. While at 14 Hz Figure 3.21 shows an anti-resonance of the frame in which all motion is taken up in the head suspension and flexure of the head structure. At and above 14 Hz, the pantograph responds primarily at the input frequency with reduced amplitude. The input also has little subharmonic distortion as shown by the frequency plots of Figure 3.27.

3.5 Comparison of Analytical and Experimental Data

As indicated in Section 3.1, the basic dynamic model has been configured to represent the test pantograph. Since excitation has been applied to the center of the head structure, bending of the head structure occurred during experimentation. To represent this phenomenon, two modifications were implemented in the model: A linear spring representing flexibility between the head structure and actuator has been incorporated, and a reduced head mass (i.e. 1/3 of flexible members plus suspension unit masses) to represent the effect of the head structure.

This section presents the analytical and experimental results collectively, with a lower set of analytical plots and an upper set of experimental data on each page. For low frequencies of applied head displacement (top curve) the theory predicts no displacement of the head (center curve) with respect to the frame (Figures 3.8 through 3.12). Up to 5 Hz neither experiment or theory illustrate substantial break-away of the head. Although slight separation of the head structure from the frame is predicted by the model, no measured physical separation is found.

The small separation in the model is due to the representation of the non-linear head suspension spring, and can be dealt with by choosing a stop element rather than a stiffening spring element. At the transition to 6 Hz input, the model shows a large increase in frame response (bottom curve) and corresponding large head suspension separation which agrees well with experimental results.

Analytical data for off resonance conditions match the experimental response curves better than data at the 6 Hz resonance condition. As expected, the amplitude correlation is much closer at 7 Hz, 8 Hz, and 9 Hz than at the 6 Hz resonance. This correspondence is related to the fact that analytical runs were executed at exactly the integer input frequencies while experimental runs were typically conducted slightly off integer frequencies, while resonance amplitudes were difficult to measure precisely.

Two phenomenon occur at 10 Hz input frequency: large system response, and the dominant subharmonic effect. The analytical model predicts these features including the bounce behavior of the head separation shown in Figure 3.17.

At 12 Hz the model indicates similar relative head motion. First, partial return to the unseparated state, then separation again remains at 0.7 cm for three-quarters of a cycle, with finally impact and bounce.

At 14 Hz the subharmonic response of the theory is still present, but does not appear in the experimental data of Figure 3.21. The modeling of the head structure is not adequate at this frequency.

Above 14 Hz the theoretical correlation with the experimental results is poor; and the actual pantograph responds at every cycle, while

the analytical model maintains dominant response at the subharmonic frequency.

In summary, this study has shown that the lumped parameter nonlinear model of the test pantograph is capable of accurately predicting detailed performance including head break-away in the frequency range of 0 to 13 Hz. Above this range structural effects become important with respect to link flexibility which are not included in the lumped model. It is noted by ref. [1,2] however, that the primary frequency range of interest for the model in performance evaluations is 0 to 5 Hz, thus the lumped model should be more than adequate.

CHAPTER 4

CONCLUSION

In the research experimental and analytical procedures have been used to identify parameters and operating characteristics. A detailed analytical and experimental study of a test pantograph has been completed which has resulted in the formulation of a nonlinear, lumped parameter, experimentally verified pantograph model. The experimental investigation has led to identification of geometric, coulomb friction, and suspension stops (or variable stiffness) as significant nonlinearities influencing pantograph performance, and has shown that for operation under conditions with disturbance frequencies greater than 13 Hz, pantograph frame and head structural resonances are important. The experimental data have been used to validate a lumped parameter nonlinear pantograph model valid for disturbances in the 0-13 Hz frequency range. Such a model is adequate for pantograph-catenary interactions in the primary operating ranges of interest in the United States.

As mentioned above, a nonlinear computer model has been developed which incorporates three nonlinearity types. The first, physical geometry, affects the effective frame parameters of the linearized version, and limits the validity of the 2-mass model when it is compelled to function about heights distant from its nominal operation height. The second, head suspension stops, prevents smooth transitions and recovery in the head suspension, and was shown to be a source of loss-of-contact and large contact force. The third, coulomb friction, is a source of rough motion and large contact force when found in the head suspension, and has little effect on pantograph behavior when found in frame joints.

Measurements of the physical test pantograph parameters were arranged into the necessary nonlinear model parameter values, and computer simulations were performed to predict response characteristics. With reference to section 3.5, the phenomenon in similarity are: the break-away of the head structure with the resonance of the pantograph system near 6 Hz, and the transition to the dominant subharmonic response at 10 Hz input.

A static analysis giving information on the force deflection characteristics of the pantograph frame has been performed. The static relation was derived by eliminating the dynamic terms from the nonlinear equations of motion. It agreed well with the experimentally obtained data which, in addition, indicated hysteresis and coulomb friction in the frame structure to be small, about 3 N.

A linearization of the equations of motion provided a basis for evaluating the effective linear frame parameters of the 2-mass model. From this technique quantitative relations specifying the effective frame parameters (i.e. M_F, K_F, B_F) for all operating heights were derived and plotted. This parametric study is valuable for determining the effective frame mass, stiffness, and damping in the 2-mass model. In addition, an understanding of their variation for different operating heights has been achieved.

The linear 2-mass model was shown to correspond to the nonlinear model as long as the excursions from the nominal operating height was not more than 20 cm.

REFERENCES

1. Wormley, D. N., Seering, W. P., Armbruster, K., Vesely, G. C., "Dynamic Performance Characteristics of New Configuration Pantograph-Catenary Systems," U.S.D.O.T. Contract No. DT-RS-56-81-C-00020, December, 1982.

2. Armbruster, K., "Modeling and Dynamics of Pantograph-Catenary Systems for High Speed Trains," S.M. Thesis, Department of Mechanical Engineering, Massachusetts Institute of Technology, 1983.

3. Morris, R. B., "Application of an Analogue Computer to a Problem of Pantograph and Overhead Line Dynamics," Proceedings of the Institute of Mechanical Engineers, Britain, 1964 - 65.

4. Gostling, R. J., and Hobbs, A. E. W., "The Interaction of Pantographs and Overhead Equipment: Practical Applications of a New Theoretical Method," paper presented at I. Mech. E. Derby Branch, February, 1981.

5. Vinayagalingam, T., "Acceleration Detection and Inertia Compensation of Pantograph Head Using a Constant Flow Hydraulic Servo," ASME Production Engineering Division, Presented at W.A.M., November, 1981.

6. Vinayagalingam, T., "Significance of Pantograph Independence Upon Quality of Current Collection at High Speed," J-DSMC.

7. Levy, S., Bain, J. A., and Leclerc, E. J., "Railway Overhead Contact Systems, Catenary-Pantograph Dynamics for Power Collection at High Speeds," Journal of Engineering for Industry, ASME Paper #68-RR2, November, 1968.

8. Elkins, J. A. "A Method for Predicting the Dynamic Response of a Pantograph Running at Constant Speed Under a Finite Length of Overhead Equipment," British Railway Board, R&D Division, Dynamics Group Technical Note TN DA 36, February, 1976.

9. Hobbs, A. E. W., "Accurate Prediction of Overhead Line Behavior," Railway Gazette International, September, 1977, pp. 339 - 343.

10. Wann, L. M., "Improvement of a Pantograph for High Speed Trains," S.M. Thesis, Massachusetts Institute of Technology, 1980.

11. Scott, P. R., and Rothman, M., "Computer Evaluation of Overhead Equipment for Electric Railroad Traction," IEEE Transactions on Industry Applications, Vol. 1A - 10, No. 5, Sept./Oct., 1974.

12. Sikorsky Aircraft, "Design and Development of a Servo-Operated-Pantograph for High Speed Trains," U.S.D.O.T. Final Report, Contract No. 7-35415, July, 1970.

13. Peters, J., "Dead Line Testing of the Faiveley Single and Dual Stage Pantographs on the RTT Catenary System," Technical Report FRA/TCC-81/01, U.S.D.O.T.

14. Grey, R. T., "Test Results of General Electric-Faiveley Pantograph for High Speed Operation," Report prepared for U.S.D.O.T., Office of High Speed Ground Transportation, December, 1967.

15. Paolini, J., "Weight Breakdown and Data on August Stemman Pantograph Type-BS129," Report prepared at the TSC of D.O.T., March, 1980.

16. Coxen, D. J., Gostling, R. J., and Whiteland, K. M., "Evolution of a Simple High-Performance Pantograph," Railway Gazette, January, 1980.

17. Belyaev, I. A., Vologine, A. A., and Freifeld, A. V., "Improvement of Pantograph and Catenaries and Method of Calculating Their Mutual Interactions at High Speeds," Rail International, June, 1977, pp. 309 - 328.

18. Schultz, D. G., Melsa, J. L., "State Functions and Linear Control Systems," McGraw-Hill, 1967, pp. 112 - 118.

APPENDIX A

DERIVATION OF NONLINEAR PANTOGRAPH MODEL

This appendix presents the derivation of the equations of motion for the two degree of freedom nonlinear dynamic pantograph model. The two degrees of freedom associated with the model are:

θ_1, frame angular position, and

y_h, absolute position of the head structure.

The model directly incorporates the nonlinear linkage configuration. With the assumption of rigid jointed links, the angular position of the links about the joints are geometrically related to the control bar vertical height, and hence only one frame degree of freedom θ_1 is required. The head mass is separated from the frame by a spring and damper suspension, where the interaction between the head and the frame is characterized by the head suspension force F_h.

For derivation purposes it is advantageous to separate the members of the frame into two free body diagrams as shown in Figure A.1. The rigid lower link rotates about point G with the applied base spring force F_b; gravity forces $m_1 g$ and $m_k g$; and the linkage forces G_x, G_y, D_x, D_y contributing to its motion. In addition, rotational friction (viscous and coulomb) are incorporated at the base pivot. The rigid upper link moves spatially subject to the constraint that point E moves vertically and that joint D of the upper link is connected to the same joint on the lower link. It includes the effects of the head suspension force F_h; gravity forces $m_2 g$ and $m_c g$; and the linkage forces D_x, D_y, E_x. The forces pertinent to the model include:

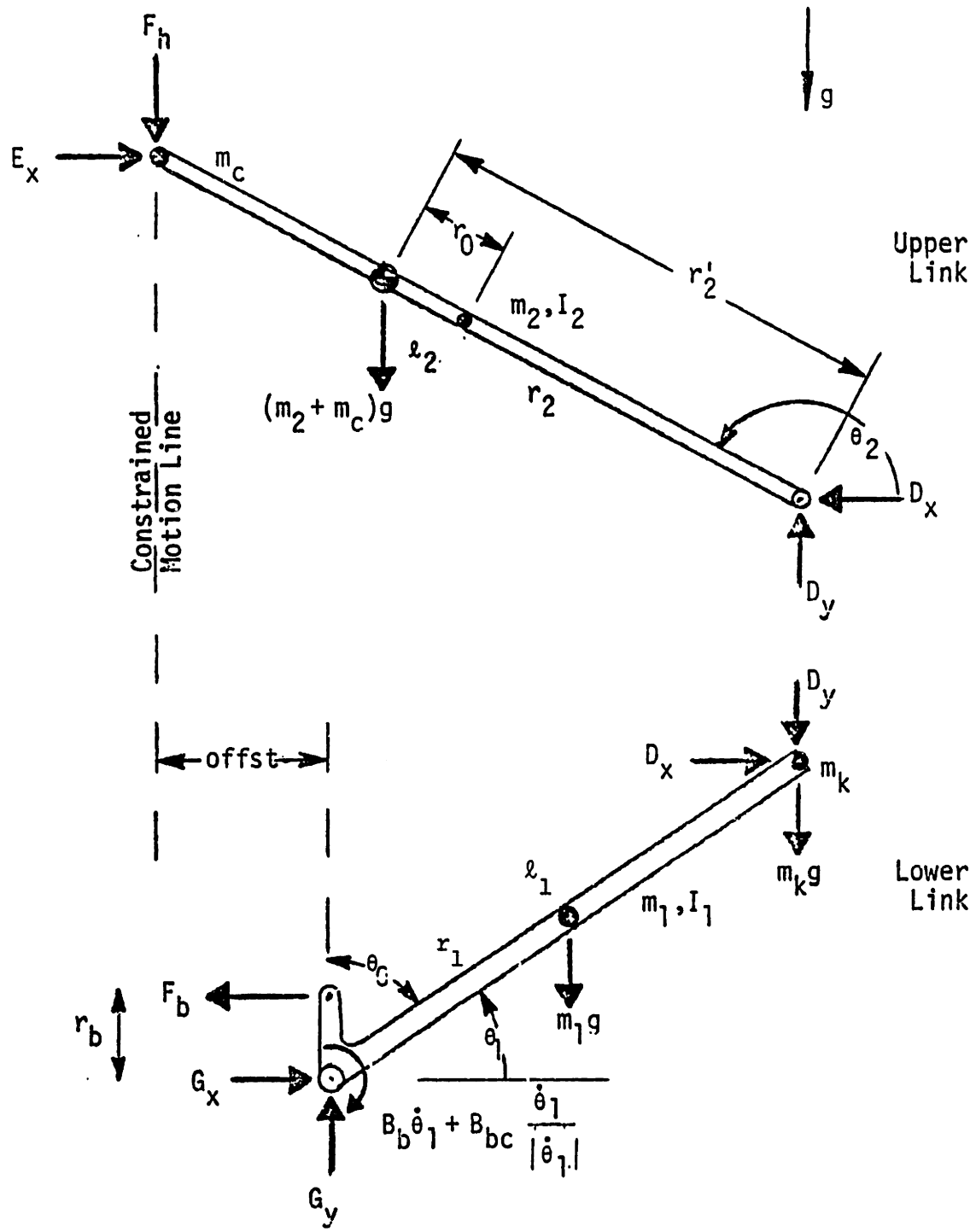

FIGURE A.1: FREE BODY DIAGRAM OF FRAME

G_x , horizontal base pivot force

G_y , vertical base pivot force

F_b , force from pretensioned frame spring

D_x , horizontal linkage force between members at knuckle

D_y , vertical linkage force between members at knuckle

E_x , horizontal linkage force at control bar point

F_h , applied force from head suspension (detailed later)

$m_1 g$, gravity force due to mass of lower link

$m_2 g$, gravity force due to mass of upper link

$m_c g$, gravity force due to lumped mass at control bar

$m_k g$, gravity force due to lumped mass at knuckle

$T_{bc} \frac{\dot{\theta}_1}{|\dot{\theta}_1|}$, rotational friction at base pivot

ition, the parameters identified in Figure A.1 are summarized as:

ffst , offset of base pivot from constrained motion line

, length of lower link

, length of upper link

, distance to mass of lower link from base pivot

, distance to mass of upper link from knuckle

, moment arm length about point G to where force F_b acts

, angle between moment arm and centerline of lower link

, mass of lower link

, mass of upper link

, lumped mass of control bar

, concentrated mass of knuckle

, moment of inertia of lower link about c-of-m including only m_1

, moment of inertia of upper link about c-of-m including only m_2

, rotational viscous damping coefficient

, rotational coulomb friction value

, gravity

Reference to the model schematic of Figure A.1 indicates that θ_2 describes the orientation of the upper link and is related to θ_1, as given by equation (A-1).

$$\theta_2 = \arccos\left(-\ell_1/\ell_2\cos\theta_1 - \frac{offst}{\ell_2}\right) \tag{A-1}$$

Similarly,

$$\dot{\theta}_2 = fcn(\theta_1,\dot{\theta}_1) \text{ and } \ddot{\theta}_2 = fcn(\theta_1,\dot{\theta}_1,\ddot{\theta}_1),$$

and are listed in subsequent analysis. The sum of the moments about the base pivot, G, which is fixed to ground yields the following equation:

$$(I_1+m_1r_1^2+m_k\ell_1^2)\ddot{\theta}_1 = F_b r_b \sin(\theta_1+\theta_o) - m_1 g r_1 \cos\theta_1 - m_k g \ell_1 \cos\theta_1$$
$$-B_b\dot{\theta}_1 - B_{bc}\frac{\dot{\theta}_1}{|\dot{\theta}_1|} - D_y\ell_1\cos\theta_1 - D_x\ell_1\sin\theta_1 \tag{A-2}$$

F_b is given by the physical configuration of the base spring and takes the following form:

$$F_b = PRETEN + K_b r_b \cos(\theta_1 + \theta_o) \tag{A-3}$$

Where PRETEN is the pretension force in the base spring, K_b, when the moment arm r_b is vertical. Defining an equivalent moment of inertia I_b about the base pivot and collecting the nonlinkage force terms into K reduces equation (A-2) to:

$$I_b\ddot{\theta}_1 = K - D_y\ell_1\cos\theta_1 - D_x\ell_1\sin\theta_1 \tag{A-4}$$

where

$$I_b = I_1 + m_1 r_1^2 + m_k \ell_1^2 \tag{A-5}$$

and

$$K = F_b r_b \sin(\theta_1 + \theta_o) - m_1 g r_1 \cos\theta_1 - m_k g \ell_1 \cos\theta_1 - B_b \dot{\theta}_1 - B_{bc} \frac{\dot{\theta}_1}{|\dot{\theta}_1|} \tag{A-6}$$

The masses m_2 and m_c (control bar mass) combine to form the center of mass for the upper link shown in Figure A.1. The values for r_2' and r_o, locating the center of mass, are found from the following relations:

$$r_2' = \frac{m_2 r_2 + m_c \ell_2}{m_2 + m_c} \tag{A-7}$$

$$r_o = \frac{m_c (\ell_2 - r_2)}{m_2 + m_c} \tag{A-8}$$

Taking moments about the center of mass yields the following equation:

$$I_2' \ddot{\theta}_2 = -D_y r_2' \cos\theta_2 - D_x r_2' \sin\theta_2 - F_h (\ell_2 - r_2') \cos\theta_2 - E_x (\ell_2 - r_2') \sin\theta_2 \tag{A-9}$$

Where the final moment of inertia I_2' about the center of mass is:

$$I_2' = I_2 + m_2 r_o^2 + m_c (\ell_2 - r_2')^2 \tag{A-10}$$

The sum of the horizontal forces equals the horizontal acceleration of m_2, where m_c only moves vertically and therefore is not included in equation (A-11).

$$m_2 \ddot{x}_2 = E_x - D_x \tag{A-11}$$

x_2 is the horizontal displacement measured horizontally from point G to the upper link mass m_2.

The sum of the vertical forces equals the vertical acceleration of the combined mass at the center of mass, thus:

$$(m_2 + m_c)\ddot{y}_2' = D_y - F_h - (m_2 + m_c)g \qquad \text{(A-12)}$$

Where y_2' is the vertical height measured from point G to the upper link center of mass.

With the appropriate substitutions and algebraic manipulations of equations (A-4), (A-9), (A-11), and (A-12), the following differential equation is obtained:

$$I_b\ddot{\theta}_1 - I_2' \frac{\ell_1 \sin\theta_1}{\ell_2 \sin\theta_2}\ddot{\theta}_2 + (m_2 + m_c)(\ddot{y}_2' + g)\left(\ell_1\cos\theta_1 - r_2' \frac{\ell_1 \sin\theta_1}{\ell_2 \sin\theta_2}\right)$$

$$-m_2\ddot{x}_2(\ell_2 - r_2')\sin\theta_2 \frac{\ell_1 \sin\theta_1}{\ell_2 \sin\theta_2} - K + F_h\left(\ell_1\cos\theta_1 - \ell_2\cos\theta_2 \frac{\ell_1 \sin\theta_1}{\ell_2 \sin\theta_2}\right) = 0 \qquad \text{(A-13)}$$

Common groups of terms, representative of effective lengths, occurring frequently are conveniently labelled as follows:

$$\delta_1 = (\ell_2 - r_2')\sin\theta_2 \frac{\ell_1 \sin\theta_1}{\ell_2 \sin\theta_2} \qquad \text{(A-14)}$$

$$\delta_2 = \ell_1\cos\theta_1 - r_2'\cos\theta_2 \frac{\ell_1 \sin\theta_1}{\ell_2 \sin\theta_2} \qquad \text{(A-15)}$$

$$\delta_3 = \ell_1\cos\theta_1 - \ell_2\cos\theta_2 \frac{\ell_1 \sin\theta_1}{\ell_2 \sin\theta_2} \qquad \text{(A-16)}$$

These simplifications, along with the following kinematic relations:

$$\ddot{x}_2 = -\ell_1 \sin\theta_1 \ddot{\theta}_1 - r_2 \sin\theta_2 \ddot{\theta}_2 - \ell_1 \cos\theta_1 \dot{\theta}_1^2 - r_2 \cos\theta_2 \dot{\theta}_2^2 \quad \text{(A-17)}$$

$$\ddot{y}_2' = \ell_1 \cos\theta_1 \ddot{\theta}_1 + r_2' \cos\theta_2 \ddot{\theta}_2 - \ell_1 \sin\theta_1 \dot{\theta}_1^2 - r_2' \sin\theta_2 \dot{\theta}_2^2 \quad \text{(A-18)}$$

$$\dot{\theta}_2 = - \frac{\ell_1 \sin\theta_1}{\ell_2 \sin\theta_2} \dot{\theta}_1 \quad \text{(A-19)}$$

$$\ddot{\theta}_2 = - \frac{\ell_1 \sin\theta_1}{\ell_2 \sin\theta_2} \ddot{\theta}_1 - \frac{\ell_1}{\ell_2 \sin\theta_2} (\cos\theta_1 + \frac{\ell_1 \sin^2\theta_1 \cos\theta_2}{\ell_2 \sin^2\theta_2}) \dot{\theta}_1^2 \quad \text{(A-20)}$$

$$q_1 = \frac{\ell_1 \sin\theta_1}{\ell_2 \sin\theta_2} \quad \text{(A-20)}$$

$$q_2 = \frac{\ell_1}{\ell_2 \sin\theta_2} (\cos\theta_1 + \frac{\ell_1 \sin^2\theta_1 \cos\theta_2}{\ell_2 \sin^2\theta_2}) \quad \text{(A-22)}$$

are utilized with algebraic manipulation to yield the following differential equation of motion:

$$\ddot{\theta}_1 [I_b + I_2' q_1^2 + (m_2+m_c)(\ell_1 \cos\theta_1 \delta_2 - r_2' \cos\theta_2 \delta_2 q_1) + m_2 (\ell_1 \sin\theta_1 \delta_1 - r_2 \sin\theta_2 \delta_1 q_1)]$$

$$+ \dot{\theta}_1^2 [I_2' q_1 q_2 - (m_2+m_c)(\ell_1 \sin\theta_1 \delta_2 + r_2' \cos\theta_2 \delta_2 q_2 + r_2' \sin\theta_2 \delta_2 q_1^2)$$

$$+ m_2 (\ell_1 \cos\theta_1 \delta_1 - r_2 \sin\theta_2 \delta_1 q_2 + r_2 \cos\theta_2 \delta_1 q_1^2)] + (m_2+m_c) g \delta_2 - K + F_h \delta_3 = 0$$

Equation (A-23) is conveniently rewritten about the angular degree of freedom as:

$$I \ddot{\theta}_1 + C \dot{\theta}_1^2 = Q \quad \text{(A-23)}$$

where $$I = I_b + I_2' q_1^2 + (m_2 + m_c)(\ell_1 \cos\theta_1 \delta_2 - r_2' \cos\theta_2 \delta_2 q_1) + m_2(\ell_1 \sin\theta_1 \delta_1 - r_2 \sin\theta_2 \delta_1 q_1) \quad \text{(A-25)}$$

and is designated the generalized inertia coefficient, where

$$C = I_2' q_1 q_2 - (m_2+m_c)(\ell_1 \sin\theta_1 \delta_2 + r_2' \cos\theta_2 \delta_2 q_2 + r_2' \sin\theta_2 \delta_2 q_1^2) + m_2(\ell_1 \cos\theta_1 \delta_1 - r_2 \sin\theta_2 \delta_1 q_2 + r_2 \cos\theta_2 \delta_1 q_1^2) \quad \text{(A-26)}$$

and is designated the centripetal coefficient, and where

$$Q = K - (m_2 + m_c) g \delta_2 - F_h \delta_3 \quad \text{(A-27)}$$

is designated the generalized torque.

The head suspension force F_h is readily obtainable from consideration of the free body diagram for the pantograph head. The derivation of the equation of motion for the pantograph head follows.

Figure A.2 shows the degree of freedom associated with the head is y_h, which is a measure of the absolute height of the pantograph head, and can alternatively be determined by summing the control bar height y_c and relative displacement of the head from the control bar, z.

The parameters pertinent to the free body diagram shown in Figure A.2 are:

m_h, mass of head

K_h, spring stiffness of head suspension

B_h, viscous damping rate of head suspension

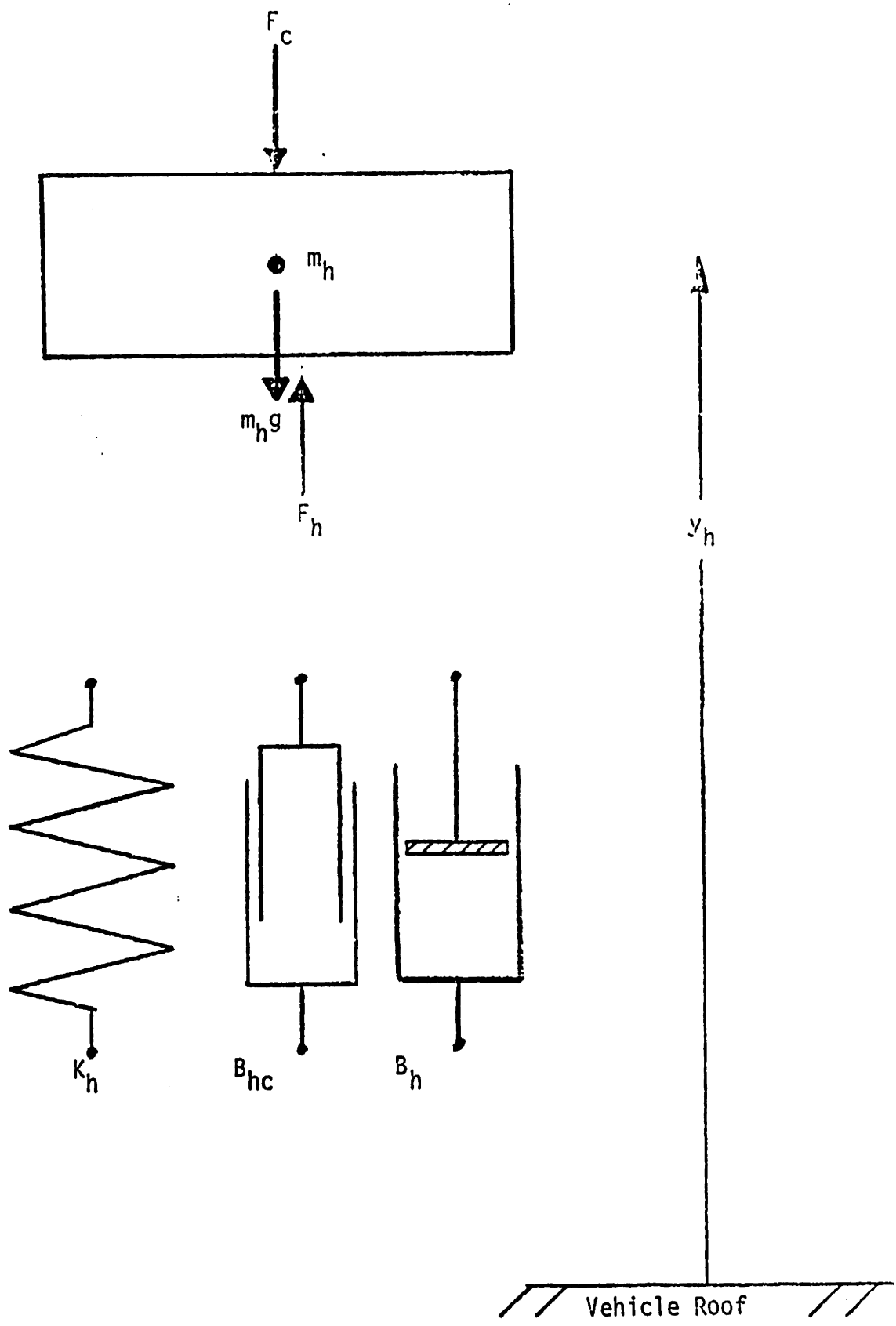

FIGURE A.2: FREE BODY DIAGRAM OF PANTOGRAPH HEAD

B_{hc}, coulomb friction in head suspension

The sum of the forces on the head mass equals the acceleration of m_h, thus:

$$m_h\ddot{y}_h = -F_c - m_h g - K_h(y_h - y_c) - B_h(\dot{y}_h - \dot{y}_c) - B_{hc}\frac{(\dot{y}_h - \dot{y}_c)}{|\dot{y}_h - \dot{y}_c|} \qquad \text{(A-28)}$$

The interaction between the head and the control bar of the frame occurs through suspension elements K_h, B_h, and B_{hc}.

Inspection of the above differential equation (A-28) reveals the head suspension force is defined as:

$$F_h = -K_h(y_h - y_c) - B_h(\dot{y}_h - \dot{y}_c) - B_{hc}\frac{(\dot{y}_h - \dot{y}_c)}{|\dot{y}_h - \dot{y}_c|} \qquad \text{(A-29)}$$

The kinematic equations relating y_c and $\dot{y}_c$ to θ_1 and $\dot{\theta}_1$ are:

$$y_c = \ell_1 \sin\theta_1 + \ell_2 \sin\theta_2 \qquad \text{(A-30)}$$

$$\dot{y}_c = \delta_3 \dot{\theta}_1 \qquad \text{(A-31)}$$

Hence, the final form of the two differential equations (A-24 and A-29) combine to form the equations of motion for the pantograph model, and are summarized as:

$$I\ddot{\theta}_1 + C\dot{\theta}_1^2 = Q \qquad \text{(A-32)}$$

$$m_h\ddot{y}_h + B_h(\dot{y}_h - \delta_3\dot{\theta}_1) + K_h[y_h - (\ell_1\sin\theta_1 + \ell_2\sin\theta_2)] =$$

$$-F_c - m_h g - B_{hc}\frac{(\dot{y}_h - \delta_3\dot{\theta}_1)}{|\dot{y}_h - \delta_3\dot{\theta}_1|} \qquad \text{(A-33)}$$

where I is given by equation (A-25),

C is given by equation (A-26),

Q is given by equation (A-27),

and where F_h, contained in the generalized force expression (Q), is rewritten from equation (A-29) in terms of the two degrees of freedom as:

$$F_h = -K_h[y_h-(\ell_1\sin\theta_1+\ell_2\sin\theta_2)] - B_h(\dot{y}_h-\delta_3\dot{\theta}_1)$$

$$-B_{hc}\frac{(\dot{y}_h - \delta_3\dot{\theta}_1)}{|\dot{y}_h - \delta_3\dot{\theta}_1|} \qquad \text{(A-34)}$$

Equation (A-32) relates the dynamics of the frame about the generalized coordinate $\dot{\theta}_1$ with applied forces and equation (A-33) relates the dynamics of the pantograph head about the generalized coordinate y_h with applied forces. The model input consists of the vertical force F_c from catenary interaction.

APPENDIX B

STATIC MODEL DERIVATION

This section presents the static analysis for the physically asymmetric frame pantograph. Rigid links with the applied forces (F_c, F_b, and F_h) and gravity forces on the five lumped masses are utilized. The initial static relations are derived by eliminating the dynamic terms from equation (A-32) (i.e. Q), and the resulting expression from equation (A-33) is:

$$K_h[y_h - (\ell_1 \sin\theta_1 + \ell_2 \sin\theta_2)] = -F_c - m_h g \qquad \text{(B-1)}$$

The term Q as indicated in equation (A-27) is:

$$F_b r_b \sin(\theta_1+\theta_o) - m_1 g r_1 \cos\theta_1 - m_k g \ell_1 \cos\theta_1 - (m_2+m_c) g \delta_2 - F_h \delta_3 = 0 \qquad \text{(B-2)}$$

Since F_h equals the negative of the left hand side of equation (B-1) neglecting dynamic terms, substitution of the right hand side of equation (B-1), for F_h, into equation (B-2), yields:

$$F_c = \frac{F_b r_b \sin(\theta_1+\theta_o) - m_1 g r_1 \cos\theta_1 - m_k g \ell_1 \cos\theta_1 - (m_2+m_c) g \delta_2}{\delta_3} - m_h g$$

where F_b is given by equation (A-3).

Equation (B-3) gives the force required for equilibrium at various pantograph positions θ_1 corresponding to pantograph heights y_c.

APPENDIX C

LINEARIZATION OF NONLINEAR EQUATIONS

This section presents the linearization of the nonlinear equations of motion similar to the technique presented in Ref. [18]. The nonlinear equations (A-32) and (A-33) are valid in the full operating range, while the linearized version of the nonlinear equations are valid only in the neighborhood of an equilibrium operating height. The subsequent analysis derives the expressions determining the linear form of the equations of motion for the linear 2-mass model from the nonlinear form of the equations of motion. In addition, quantitative results of the effective linear parameters for the test pantograph are determined. The angular degree of freedom in the linear model is translated into a displacement coordinate specifying the position of an effective frame mass in the linear model. The linearization proceeds excluding nonlinear and nonmonotonic terms, such as coulomb friction and head suspension stop characteristics. The two degrees of freedom associated with the linear model are:

y_H, absolute position of the head about some operating height, and

y_F, absolute position of the effective frame mass about some operating height.

The head mass and the nominal head suspension elements are those used in the nonlinear model. The following analysis provides expressions for the effective frame mass and frame suspension elements.

The generalized coordinates associated with equations (A-32) and (A-33) are not suitable for the desired linear analysis. A coordinate

transformation of θ_1 to the height of the control bar y_c is used to derive the effective frame mass motion. The transformation is based on the following kinematic relations:

$$\dot{\theta}_1 = 1/\delta_3 \, \dot{y}_c \tag{C-1}$$

$$\ddot{\theta}_1 = 1/\delta_3 \, \ddot{y}_c + \frac{\delta_4}{\delta_3^3} \dot{y}_c^2 \tag{C-2}$$

where δ_3 is listed by equation (A-16), and

$$\delta_4 = \ell_2 \cos\theta_2 q_2 + \ell_1 \sin\theta_1 + \ell_2 \sin\theta_2 q_1^2 \tag{C-3}$$

The resulting nonlinear equations of motion become:

$$\frac{I}{\delta_3} \ddot{y}_c + (\frac{\delta_4}{\delta_3^3} I + C/\delta_3^2)\dot{y}_c^2 = Q \tag{C-4}$$

$$m_h \ddot{y}_h + B_h(\dot{y}_h - \dot{y}_c) + K_h(y_h - y_c) = -m_h g - F_c \tag{C-5}$$

Equation (C-4) is a statement of the force balance on the frame, and equation (C-5) is a statement of the force balance on the head mass m_h.

Considering tracking at a particular height, excursions of the state variables $(y_c, \dot{y}_c, y_h, \dot{y}_h)$ and input variables are designated about this height with a Δ. Then new state variables and input are defined as follows:

$$\Delta y_c = y_c - y_c^\circ$$

$$\Delta \dot{y}_c = \dot{y}_c$$

$$\Delta y_h = y_h - y_h^\circ$$

$$\Delta \dot{y}_h = \dot{y}_h$$

$$\Delta F_c = F_c - F_c^\circ$$

where equilibrium conditions are:

y_c° - the operating height

y_h° - equilibrium head height

F_c° - equilibrium input force

The equilibrium values are determined from the nonlinear equations by setting all derivatives of state variables (accelerations and velocities) to zero. y_c°, the operating height is chosen arbitrarily while F_c° is given by equation (B-3) with θ_1 and θ_2 found in terms of the operating height. y_h° is determined from equation (C-5), where F_c is again found from equation (B-3), and is:

$$y_h^\circ = y_c^\circ - \frac{m_h g}{K_h} - \frac{F_c^\circ}{K_h} \qquad \text{(C-6)}$$

Applying the technique discussed in reference [18] to equations (C-4) and (C-5), the resulting linearization in coordinates (Δy_c, $\Delta \dot{y}_c$, Δy_h, $\Delta \dot{y}_h$) is in the following form with all partial derivatives evaluated at the equilibrium conditions:

$$\frac{I}{\delta_3} \Delta \ddot{y}_c = \left.\frac{\partial Q}{\partial y_c}\right|_o \Delta y_c + \left.\frac{\partial Q}{\partial \dot{y}_c}\right|_o \Delta \dot{y}_c + \left.\frac{\partial Q}{\partial y_h}\right|_o \Delta y_h + \left.\frac{\partial Q}{\partial \dot{y}_h}\right|_o \Delta \dot{y}_h \qquad \text{(C-7)}$$

$$m_h \Delta \ddot{y}_h = K_h \Delta y_c + B_h \Delta \dot{y}_c - K_h \Delta y_h - B_h \Delta \dot{y}_h - \Delta F_c \qquad \text{(C-8)}$$

The second equation is derived directly from equation (C-5) excluding the constant gravity force on the head. The first equation involves evaluating more complicated partial derivatives. The terms in equation (C-4) premultiplying $\dot{y}_c^2$ do not have a role in the linear version, because $\dot{y}_c$ equals zero at equilibrium and is always post-multiplying any partial derivative result of these terms. It is also important to note that when evaluating the coefficient in front of Δy_c, Q is equal to zero at equilibrium as shown in the static analysis.

The partial derivatives evaluated at equilibrium in terms of the nonlinear model's parameters are:

$$\left.\frac{\partial Q}{\partial \dot{y}_h}\right|_o = B_h \delta_3 \qquad \text{(C-9)}$$

$$\left.\frac{\partial Q}{\partial y_h}\right|_o = K_h \delta_3 \qquad \text{(C-10)}$$

$$\left.\frac{\partial Q}{\partial \dot{y}_c}\right|_o = -B_b/\delta_3 - B_h \delta_3 \qquad \text{(C-11)}$$

$$\left.\frac{\partial Q}{\partial y_c}\right|_o = \{-K_b r_b^2 \sin^2(\theta_1+\theta_o)+F_b r_b \cos(\theta_1+\theta_o)+m_1 g r_1 \sin\theta_1+m_k g \ell_1 \sin\theta_1$$

$$+(m_2+m_c)g[\ell_1\sin\theta_1+r_2'\frac{\ell_1}{\ell_2}\sin\theta_1 q_1+r_2'\cos\theta_2\frac{\ell_1}{\ell_2}\frac{\cos\theta_1}{\sin\theta_2}+r_2'\cos^2\theta_2\frac{\ell_1}{\ell_2}\frac{\sin\theta_1}{\sin^2\theta_2}q_1$$

$$-[-F_b r_b \sin(\theta_1+\theta_o)+m_1 g r_1\cos\theta_1+m_k g\ell_1\cos\theta_1+(m_2+m_c)g\delta_2]\cdot\frac{1}{\delta_3}$$

$$\cdot[\ell_1\sin\theta_1+\ell_1 q_1\sin\theta_1+\ell_1\cos\theta_1\frac{\cos\theta_2}{\sin\theta_2}+\ell_1\sin\theta_1\frac{\cos^2\theta_2}{\sin^2\theta_2}q_1]\}\cdot\frac{1}{\delta_3}$$

$$-K_h\delta_3 \qquad \text{(C-12)}$$

After dividing all partial derivative results (i.e. equations (C-9) through (C-10)) by δ_3; equation (C-9) corresponds to the linear model's parameter B_H, equation (C-10) corresponds to the linear model's parameter K_H, equation (C-11) corresponds to the linear model's parameter combination $-B_F-B_H$, and equation (C-12) corresponds to the linear model's parameter combination $-K_F-K_H$. In addition, to preserve the equivalence of equation (C-7), the coefficient premultiplying $\Delta\ddot{y}_c$ is divided by δ_3 and corresponds to the linear model's parameter M_F. Hence:

$$M_F = I/\delta_3^2 \qquad \text{(C-13)}$$

$$K_F = \{K_b r_b^2 \sin^2(\theta_1+\theta_o)-F_b r_b\cos(\theta_1+\theta_o)-m_1 g r_1\sin\theta_1-m_k g\ell_1\sin\theta_1$$

$$-(m_2+m_c)g[\ell_1\sin\theta_1+r_2'\frac{\ell_1}{\ell_2}\sin\theta_1 q_1+r_2'\cos\theta_2\frac{\ell_1}{\ell_2}\frac{\cos\theta_1}{\sin\theta_2}+r_2'\cos^2\theta_2\frac{\ell_1}{\ell_2}\frac{\sin\theta_1}{\sin^2\theta_2}q_1]$$

$$+[-F_b r_b\sin(\theta_1+\theta_o)+m_1 g r_1\cos\theta_1+m_k g\ell_1\cos\theta_1+(m_2+m_c)g\delta_2]\cdot\frac{1}{\delta_3}$$

$$\cdot[\ell_1\sin\theta_1+\ell_1 q_1\sin\theta_1+\ell_1\cos\theta_1\frac{\cos\theta_2}{\sin\theta_2}+\ell_1\sin\theta_1\frac{\cos^2\theta_2}{\sin^2\theta_2}q_1]\}\frac{1}{\delta_3^2} \qquad \text{(C-14)}$$

$$B_F = B_b/\delta_3^2 \tag{C-15}$$

and the rest of the lienar model's parameters are:

$$M_H = m_h \tag{C-16}$$

$$K_H = K_h \tag{C-17}$$

$$B_H = B_h \tag{C-18}$$

as expected since the pantograph head suspension is in linear form at the outset.

The dimensionality of the frame linearized parameters is preserved. Equation (C-13) has mass dimensions for the effective frame mass, equation (C-14) has force-per-length dimensions for the effective frame stiffness, and equation (C-15) yields force per length per second dimensions for the effective frame damping. Note that B_b in equation (C-15) is torsional damping of the nonlinear model. All of the effective frame parameters are evaluated at a nominal operating height.

Finally equations (C-7) and (C-8), with the coefficients determined by equations (C-13) through (C-18) take the following linear form:

$$M_F\ddot{y}_F = -(K_F + K_H)y_F - (B_F + B_H)\dot{y}_F + K_H y_H + B_H\dot{y}_H \tag{C-19}$$

$$M_H\ddot{y}_H = K_H y_F + B_H\dot{y}_F - K_H y_H - B_H\dot{y}_H - \Delta F_c \tag{C-20}$$

where Δy_c and Δy_h have been replaced by y_F and y_H respectively. Equations (C-19) and (C-20) constitute the linear two-mass model.